Imperial College London
Department of Bioengineering

Advanced Beamforming for High Frame Rate Ultrasound Vascular Imaging

Antonio Stanziola

Submitted in part fulfilment of the requirements for the degree of
Doctor of Philosophy in Bioengineering of the Imperial College London, February
20, 2019

Declaration of originality

The studies illustrated in this thesis are, to the best of my knowledge, entirely my work conducted at the Department of Bioengineering, Imperial College London, during my PhD studies between October 2012 and October 2018. All the assistance received in writing this thesis has been acknowledged and additional sources of information have been duly cited.

Antonio Stanziola

Acknowledgements

I am grateful to my supervisor for his continuous guidance and support during my whole PhD studies: his passion for new ideas and science tremendously helped me in becoming a better researcher. I'm also grateful to the whole ULIS group, including past members, for their support over the years. I also thank all the firends of the Imperial college for all beautiful discussion we had: JD, Marta, Jacopo, Nikola, Sara, Guillaume, Matjaz and Margherita.

Dedication

I want to dedicate this thesis to my family, my stupidly smart brother and Sara, for their fundamental support over the last years. I wouldn't have made it without you. I also dedicate this to the friends of *h tagliato*, as if it was antani with tarapiatapioco.

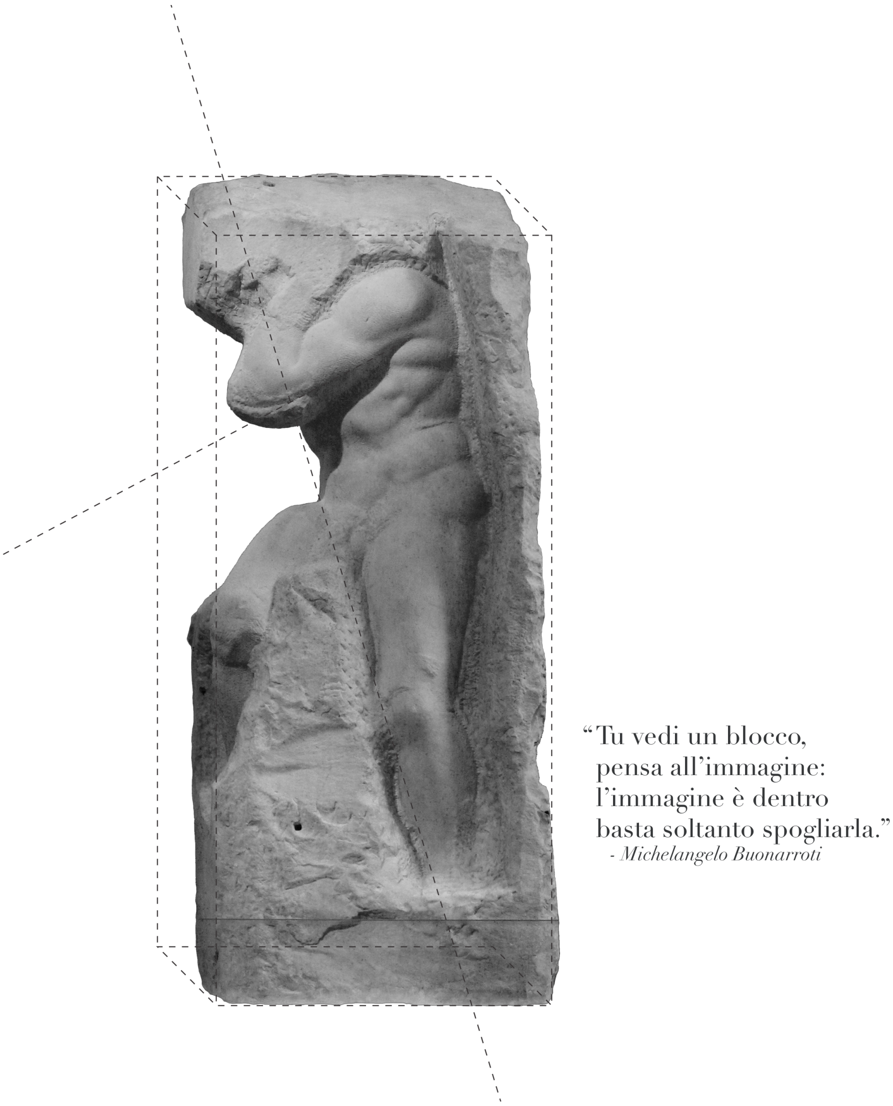

Atlas Slave' by Michelangelo for the Julius Tomb, 1520-23, Florence, Galleria dell' Accademia, distributed under the Creative Commons Attribution-Share Alike 3.0 Unported licence. Original image author: Jörg Bittner Unna; graphical elaboration by Francesco Stanziola

Abstract

Ultrasound vascular imaging has seen two major advances which are unfolding unprecedented possibilities for research: the first being the use of microbubbles as contrast agents to highlight the vasculature, while the second one is the use of unfocused transmission and digital image reconstruction techniques yielding a remarkable frame-rate increase. Their consolidation is pushing scientists to design acquisition procedures and reconstruction models to surpass conventional approaches developed for focused ultrasound, taking full advantage of the new available data. In this thesis, signal processing, in particular spatial and temporal second order statistics, has been used to try pushing the boundaries in this direction.

In the first contributing chapter, some limitations of classical coherent compounding and multipulse imaging methods for contrast ultrasound are highlighted, with the use of both simulations and in vivo experiments, in particular when fast flow is imaged: as an example, the case of cardiac imaging with diverging waves is reported. The results show how motion is responsible for large intensity drops, up to tens of dB, which can have potential detrimental effects in quantifications studies. The results also show the dependency of this effect on a variety of acquisition settings and we also highlight some artefacts arising from those scenarios. Finally, reduction of such artefacts by correcting motion is demonstrated.

In the second contributing chapter, a new method is developed to reduce noise in High-Frame Rate vascular images. Standard vascular imaging using e.g Power Doppler are characterized by a low Signal to Noise Ratio, especially for unfocused acquisitions. Using cross correlation between two different estimates of the same target vascular signal, we devised a method called Acoustic Sub-Aperture Processing (ASAP) which reduces the noise floor given by random uncorrelated sources, such as electronics, while maintaining the same power estimate. The two estimates can be chosen both as different spatial location within the same point spread function, or as the results of two orthogonal projections of the same pixel value. In this way, a noise reduction proportional to the square root of the number of averaged frames is achieved. The effectiveness of this technique has been tested in several in-vivo settings, both for contrast and non contrast acquisitions.

In the third contributing chapter, methods are developed to reduce imaging artefacts such as side lobes and grating lobes. While effective, ASAP is susceptible to artefacts due principally to the interference generated by strong scatterers like big vessels. Under certain conditions, the presence of artefacts can even reduce the ability to image small vessels compared to simpler approaches. Assuming lack of correlation

of the different interference signals, we have devised an adaptive method to select the two sub-apertures in the noise subspace. The results show that such method is effective at mitigating the contribution of interferences to the final image and therefore the strength of the artefacts, improving the visualization of smaller vessels, albeit creating a tradeoff between computational time and quality of the result. Because of the computational load required by the proposed method, we also propose an alternative fast approach based on the spatial Fourier transform.

As ASAP is not the only technique based on cross correlation, the last contributing chapter proposes a tensorial framework capable of the generalizing several coherence methods currently available, by taking into account the different possible domains of correlations, like space, channels, depth and frames. This is done by extending the variance matrix to a variance tensor. Besides deepening the understanding of the interconnection of the various techniques, the multilinear approach allows to combine the various methods to achieve superior performances while keeping the computational time manageable compared to adaptive methods. The algorithms have been preliminary tested in challenging scenarios like contrast enhanced cardiac acquisitions and in vitro. The results suggest improvements in terms of interference and artefacts reductions compared to matrix based processing. A promising future direction is suggested, namely the use of tensorial decomposition techniques for source separation to improve the reconstruction of vascular images

List of publications

Journal Publications

A. Stanziola, M. Toulemonde, Y. O. Yildiz, R. J. Eckersley and M.-X. Tang, *Ultrasound Imaging with Microbubbles [Life Sciences]*, in IEEE Signal Processing Magazine, Volume 33, no. 2, pp. 111-117, March 2016.

W. K. Cheung, B. N. Shah, **A. Stanziola**, D. M. Gujral, N. S. Chahal, D. O. Cosgrove, R. Senior, M.-X. Tang, *Differential Intensity Projection for Visualisation and Quantification of Plaque Neovascularisation in Contrast-Enhanced Ultrasound Images of Carotid Arteries*, in Ultrasound in Medicine & Biology, Volume 43, Issue 4, pp. 831-837, 2017.

S. Lin, A. Shah, J. Hernández-Gil, **A. Stanziola**, B. I. Harriss, T. O. Matsunaga, N. Long, J. Bamber, M.-X. Tang, *Optically and acoustically triggerable sub-micron phase-change contrast agents for enhanced photoacoustic and ultrasound imaging*, in Photoacoustics, Volume 6, pp. 26-36, 2017

A. Stanziola, C.H. Leow, E. Bazigou, P.D. Weinberg, M.-X. Tang, *ASAP: super-contrast vasculature imaging using coherence analysis and high frame-rate contrast enhanced ultrasound*, in IEEE Transactions on Medical Imaging, Volume 37, no. 8, pp. 1847-1856, Aug. 2018.

A. Stanziola, M. Toulemonde, Y. Li, V. Papadopoulou, R. Corbett, N. Duncan, R. J. Eckersley, M.-X. Tang, *Motion Artifacts and Correction in Multi-Pulse High Frame Rate Contrast Enhanced Ultrasound*, IEEE transactions on ultrasonics, ferroelectrics, and frequency control, Dec. 2018.

Submitted

C. H. Leow, N. L. Bush, **A. Stanziola**, M. Braga, A. Shah, J. Hernandez-Gil, N. J. Long, O. Aboagye, J.C. Bamber, M.-X. Tang, *3D microvascular imaging using high frame rate ultrasound and ASAP without contrast agents: development and initial in vivo evaluation on non-tumour and tumour models*, submitted to IEEE transactions on ultrasonics, ferroelectrics, and frequency control.

Conferences

A. Stanziola, M.-X. Tang, *Temporal and spatial processing of high frame-rate contrast enhanced ultrasound data*, Proceedings of the 21st European Symposium on Ultrasound Contrast Imaging, p160-162, Rotterdam, January 2016.

A. Stanziola, C.H. Leow, E. Bazigou, P. D. Weinberg, M.-X. Tang, *Acoustic Sub-Aperture Processing (ASAP) for vascular imaging using high frame-rate ultrasound and microbubbles*, 2016 IEEE International Ultrasonics Symposium (IUS), Washington, France, 2016.

A. Stanziola, M.-X. Tang, *Super contrast imaging using high frame-rate CEUS and spatial and temporal signal processing*, Proceedings of the 22nd European Symposium on Ultrasound Contrast Imaging, Rotterdam, January 2017.

M. Toulemonde, W. C. Duncan, **A. Stanziola**, V. Sboros, Y. Li, R. J Eckersley, S. Lin, M.-X. Tang, M. Butler ,*Effects of motion on high frame rate contrast enhanced echocardiography and its correction*, 2017 IEEE International Ultrasonics Symposium (IUS), Washington, DC, 2017.

C. H. Leow, M. Braga, **A. Stanziola**, J. Hernández-Gil, N. J. Long, E. O. Aboagye, M.-X. Tang, *Multi-frame rate plane wave contrast-enhance ultrasound imaging for tumour vasculature imaging and perfusion quantification*, 2017 IEEE International Ultrasonics Symposium (IUS), Washington, DC, 2017.

J. Zhu, E. Rowland, C. H. Leow, K. Riemer, **A. Stanziola**, S. Harput, K. Cox, P. D. Weinberg, M.-X. Tang, *High frame rate contrast enhanced ultrasound imaging of lymph node in vivo*, Proceedings of the 21st European Symposium on Ultrasound Contrast Imaging, p31-33, Rotterdam, January 2018.

A. Stanziola, M. Toulemonde, R. Corbett, V. Papadopoulou, R.J. Eckersley, N. Duncan, M.-X. Tang, *Benefits of adaptive beamforming methods for contrast enhanced high frame-rate ultrasound*, presented at the 2018 IEEE International Ultrasonics Symposium (IUS), Kobe, Japan, 2018.

A. Stanziola, T. Robins, K. Riemer, M.-X. Tang, *A Deep Learning Approach to Synthetic Aperture Vector Flow Imaging*, presented at the 2018 IEEE International Ultrasonics Symposium (IUS), SA-VFI Challenge, Kobe, Japan, 2018.

Published patent application

A. Stanziola, M.-X. Tang, *Acoustic sub-aperture processing for ultrasound imaging*, GB2551376

List of Abbreviations

ASAP	Acoustic Sub-Aperture Processing
CANR	Contrast to Acoustic Noise Ratio
CC	Cross correlation
CE	Contrast Echocardiography
CEUS	Contrast Enhanced Ultrasound
CFPD	Coherent Flow Power Doppler
CNR	Contrast to Noise Ratio
CWD	Continous Wave Doppler
DAS	Delay and Sum
DAX	Dual Apodization with Cross-correlation
DOA	Direction of arrival
FWHM	Full-width Half-maximum
HFR	High Frame Rate
LVC	Left Ventricular Chamber
MB	Microbubble
MI	Mechanical Index
ML	Maximum Likelihood
MPDE	Multilinear Power Doppler Estimation
MV	Minimum Variance
PCF	Phase Coherence Factor
PD	Power Doppler
PI	Pulse Inversion
PRF	Pulse Repetition frequency
PSF	Point Spread Function
PWD	Pulsed Wave Doppler
PWI	Plane Wave Imaging
RF	Radio Frequency
ROI	Region of Interest

SAI	Synthetic Aperture Imaging
SLSC	Short Lag Spatial Coherence
SNR	Signal to Noise Ratio
SOS	Second Order Statistics
SVD	Singular Value Decomposition
US	Ultrasound

Nomenclature

$\mathbf{a}$	Apodization vector
$\mathbf{A}$, $\mathbf{B}$, $\mathbf{C}$,...	Matrix
c	Speed of sound
$\mathsf{E}_i[x]$	Ensamble average of the variable x over the index or variable i.
$\mathbf{F}$	Fourier matrix
ϕ	Velocity potential
$\hat{\mathbf{R}}$	Covariance matrix
$\mathbf{R}$	Sample covariance matrix
$R_x(\tau)$	Autocorrelation of the signal x
$\mathbf{T}_{i_1,i_2,\ldots,i_N}$	Tensor of order N
$\mathrm{Tr}(\mathbf{M})$	Trace of the matrix $\mathbf{M}$, that is $\mathrm{Tr}(\mathbf{M}) = \sum_i M_{i,i}$
ω	Frequency
$\mathbf{x}$, $\mathbf{y}$, $\mathbf{z}$,...	Vector
$\mathbf{x}^{\mathsf{H}}$	Hermitian transpose of $\mathbf{x}$
$\mathbf{x}_\perp$	Vector perpendicular to $\mathbf{x}$

Contents

List of Tables

List of Figures

Chapter 1

Background

This chapter will briefly introduce the fundamental knowledge necessary to appreciate how Ultrasound (US) images are produced, and review the relevant literature in beamforming and contrast agents. The first section starts by describing the physics behind sound propagation, including some of the most widely used approximations of interest for medical imaging, then we will describe the engineering of medical US imaging, with great focus on beamforming algorithms and their recent developments, and finally we will review contrast agents, including its use, development, physical modelling and detection techniques.

1.1 Wave physics

Wave phenomena can be observed whenever we have some kind of continuum where local oscillations can occur. The derivation of the wave equation differs for different physical situations, such as electromagnetic waves or mechanical waves, but its linear form is always given as

$$\left(\frac{\partial^2}{\partial r^2} - \frac{1}{c^2}\frac{\partial^2}{\partial t^2}\right)\Phi = 0 \tag{1.1}$$

for the one dimensional case or

$$\left(\nabla^2_{\mathbf{r}} - \frac{1}{c^2}\frac{\partial^2}{\partial t^2}\right)\Phi = 0 \tag{1.2}$$

for the three dimensional one [3]. Here, r or $\mathbf{r} \in \mathbf{R}^3$ refers to the spatial dimension, t is time and $\Phi(\mathbf{r}, t)$ is the oscillating quantity, which can represent different physical variables, such as the electric or magnetic field amplitude.

In US imaging, tissue is often crudely approximated as a fluid for which the only kind of waves that can possibly arise, called *longitudinal*, result from the oscillation of each point from its equilibrium position in the same direction as the wave propagates. In this case, the simple linear wave equation is given by [4]

$$\left(\nabla_{\mathbf{r}}^2 - \frac{1}{c^2}\frac{\partial^2}{\partial t^2}\right)\phi = 0, \tag{1.3}$$

where ϕ is the velocity potential, also known as acoustic field, from which both particle velocity $\mathbf{v}$ and pressure $\mathbf{p}$ can be derived

$$\mathbf{v} = \nabla_{\mathbf{r}}\phi, \qquad p = -\frac{\partial}{\partial t}\phi. \tag{1.4}$$

It must be kept in mind that this is a very simplified picture, as the actual nature of biological tissues is better depicted by using an anisotropic viscoelastic model, from which more complex waves of medical interest, such as shear waves, can arise and be used to infer viscoelastic properties [5]. A great review of wave physics for medical ultrasound is given by Szabo [4]. The speed of sound c_0 is given by

$$c_0 = \sqrt{\frac{\gamma B_t}{\rho_0}}, \tag{1.5}$$

where γ is the specific heat ratio, B_T is the isothermal bulk modulus and ρ_0 is the equilibrium density [4]. Clearly such values, in a real object, assume different values in different spatial locations, so $c(\mathbf{r})$ is generically regarded as a function of space. With that in mind, the aim of US imaging is to reconstruct the spatial variations of sound speed by transmitting ultrasonic waves and recording the scattered acoustic field at different locations and times. Therefore we are interested in wave propagation phenomena in the presence of acoustic sources and scatterers.

Some classes of solutions of the three dimensional wave equation have properties that make them useful for ultrasound imaging. A first family of solutions is composed of monochromatic plane waves [6]

$$\phi(\mathbf{r}, t) = \exp\left[-j\left(\frac{\mathbf{k}_0^{\mathsf{H}}\mathbf{r}}{c_0} - \omega_0 t\right)\right], \tag{1.6}$$

with $\mathbf{k} \in S^1$ is called *wave vector* and ω is the angular or temporal frequency. This solution is interesting in US imaging for a variety of reasons. First of all, it is a limited diffraction beam which can be well approximated by finite apertures meaning that, if it is generated by an ultrasound transducer, it roughly keeps its shape even after propagating for a relatively long distance [7, 8]. Secondly, if Fourier transformed both spatially and temporally, its form is

$$\phi(\mathbf{k},\omega) = \delta(\mathbf{k}-\mathbf{k}_0)\delta(\omega-\omega_0), \tag{1.7}$$

which suggests that plane waves of different spatial and temporal frequencies form a basis of the spatio-temporal Fourier spectrum and, due to linearity, all separable solutions of the wave equation can be decomposed as sums (either discrete sums or integrals) of plane waves.

Another interesting solution is the free space Green function, or impulse response, of the wave equation differential operator, which is given by [9, 10]

$$G(\mathbf{r},t) = \frac{1}{4\pi\|\mathbf{r}\|}\,\delta\left(t - \frac{\|\mathbf{r}\|}{c_0}\right). \tag{1.8}$$

This represents the acoustic field produced by an impulsive spherical wave generated in the spatial origin at time $t = 0$. When the transducer elements are small compared to the wavelength, the wave emitted by a single element can be approximated as the superposition of impulsive spherical waves [11]

$$f(\mathbf{r},t) = \int G(\mathbf{r}-\mathbf{r}_0, t-t')f_0(t')\,dt', \tag{1.9}$$

where $f_0(t)$ is the acoustic signal at the element surface.

1.1.1 Huygens principle

There are two major applications of the free space Green's function that are of interest for this work. The first one is given by the powerful Huygens principle. This principle actually derives from the temporal transform of the inhomogeneous wave equation, named Helmholtz equation

$$\left(\nabla^2_{\mathbf{r}} - \frac{\omega^2}{c^2}\right)\phi(\mathbf{r},\omega) = -f(\mathbf{r},\omega), \tag{1.10}$$

where f is a function with compact spatial support [12]. In brief, its 3D formulation states that the wave-field $\phi(\mathbf{r},\omega)$ inside a volume, V, surrounded by a surface Ω is completely determined by the field at the surface itself. Mathematically, this is given by the Kirchhoff-Helmholtz's integral equation [12]

$$\phi(\mathbf{r},\omega) = \oint_\Omega \left(\frac{\partial\phi(\mathbf{r}',\omega)}{\partial\mathbf{n}(\mathbf{r}')}G(\mathbf{r}-\mathbf{r}',\omega) - \phi(\mathbf{r}',\omega)\frac{\partial G(\mathbf{r}-\mathbf{r}',\omega)}{\partial\mathbf{n}(\mathbf{r}')}\right) d\mathbf{r}', \tag{1.11}$$

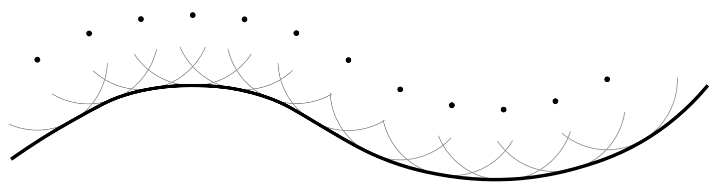

Figure 1.1: Illustration of the Huygens principle, stating that a generic wavefield (in thick black) can be reproduced by the superposition of the spherical wavefields emitted by a collection of point emitters.

where $\mathbf{n}(\mathbf{r})$ is the vector normal to the surface pointing inwards to the volume V and $G(\mathbf{r}, \omega)$ is the temporal Fourier transform of the Green's function. In practice, each point of the surface Ω is considered as a secondary source emitting both a spherical and a dipolar wave. An illustration of the Huygens principle is given in Fig. 1.1. When Ω is a box and all its faces are moved to infinity with the exception of one, that we will consider as coinciding to the (x, y) plane, the Kirchhoff-Helmholtz's equation simplifies to

$$\phi(\mathbf{r}, \omega) = -\iint_{\mathbb{R}^2} \left(\phi(\mathbf{r}', \omega) \frac{\partial G(\mathbf{r} - \mathbf{r}', \omega)}{\partial \mathbf{n}(\mathbf{r}')} \right) d\mathbf{r}'. \tag{1.12}$$

The other application of Green's functions is the calculation of delays for many beamforming techniques, as will be shown in the next section.

1.1.2 Born approximation

Following the arguments given on the third Chapter of [6], let's assume that the imaged medium is static and the velocity function $c(\mathbf{x})$ is given by the following perturbed model

$$m(\mathbf{r}) = \frac{1}{c^2}, \qquad m(\mathbf{r}) = m_0(\mathbf{r}) + \varepsilon m_1(\mathbf{r}), \tag{1.13}$$

with ε small and $m_0(\mathbf{r}) = 1/c_0^2$. We further divide the acoustic field ϕ as the sum of the incident and scattered field

$$\phi = \phi_{\text{inc}} + \phi_{\text{sct}}. \tag{1.14}$$

Now, we can easily find the solution ϕ_0 given by the propagation of the incident field on the free space wave equation with velocity c_0. With this result, the wave equation rewrites as

$$m_0(\mathbf{r}) \frac{\partial^2 \phi_0}{\partial t^2} - \nabla_{\mathbf{r}}^2 \phi_{\text{sct}} = -\varepsilon m_1(\mathbf{r}) \frac{\partial^2 \phi}{\partial t^2}, \tag{1.15}$$

which in integral form gives the Lippmann-Schwinger equation

$$\phi_{\text{sct}} = -\int_0^t \int_{\mathbb{R}^3} G(\mathbf{r}-\mathbf{r}', t-t') m_1(\mathbf{r}') \frac{\partial^2 \phi}{\partial t^2}\, d\mathbf{r} dt'. \tag{1.16}$$

Under certain conditions [6], this equation can be solved iteratively for the scattered field by the recursive formula

$$\phi^n = -\int_0^t \int_{\mathbb{R}^3} G(\mathbf{r}-\mathbf{r}', t-t') m_1(\mathbf{r}') \frac{\partial^2 \phi^{n-1}}{\partial t^2}\, d\mathbf{r}' dt', \tag{1.17}$$

with $\phi^0 = \phi_{\text{inc}}$ and $\phi_{\text{sct}} = \sum_{n=1}^{\infty} \phi^n$. If one stops at the first iteration, $n = 1$, we get what is called the *first order Born approximation* of the scattered field

$$\phi_{\text{sct}} = -\int_0^t \int_{\mathbb{R}^3} G(\mathbf{r}-\mathbf{r}', t-t') m_1(\mathbf{r}') \frac{\partial^2 \phi_{\text{inc}}}{\partial t^2}\, d\mathbf{r}' dt'. \tag{1.18}$$

This approximation is widely used in ultrasound imaging and will be encountered later in the text.

Note that the use of such approximation requires the knowledge of the speed of sound function over space, while the imaging problem tries to estimate it from knowledge of the scattered field in some points of space. For such reason, it is called an inverse problem and often named *wave inversion* problem.

The first order Born approximation can also be modified to include absorption effects [4], as to model an homogeneous medium where the amplitude drop of a wave increases with distance. To do so, the Green's function is multiplied by an exponential factor

$$G'(\mathbf{r}, \omega) = G(\mathbf{r}, \omega) e^{-\|\mathbf{r}\|/\alpha(\omega)}, \tag{1.19}$$

where the factor $\alpha(\omega)$ encodes the frequency dependent attenuation.

1.2 Ultrasound Pulse Echo Imaging

The goal of ultrasound is to build an image after measuring part of an acoustic field. For such purpose, an US machine is usually comprised by [4]:

- A probe, or transducer, which contains a set of piezoelectric elements that convert acoustic signals into electrical ones and vice-versa.
- An electric board responsible of both collecting and generating the acoustic signals.

- A central processing unit that stores and processes the acquired data.

The most widely used imaging modality, which we will consider in this thesis, is named Pulse-Echo Imaging. In such method, the transducer transmit a wideband pulse and afterwards records the backscattered echoes for an amount of time proportional to the desired scanning depth. The procedure can be repeated multiple times with different transmit sequences before reconstructing an image. Other than physical constraints, the final image depends on many tunable factors, among which we will focus on: the transmit sequence, the reconstruction method and post processing techniques. In analogy with radar and seismic imaging, the reconstruction procedure is often referred as beamforming [13, 14].

1.2.1 Transmit sequences

During the transmit phase, the elements of the transducer are excited to produce a wave pattern. In the early days of ultrasound scanners, the acoustic energy was spread in the whole medium by mechanically steering a single element, in a way that resembles scanning electromagnetic radars [4]. Each of the transmitted waves was focused using an acoustic lens to produce a narrow US beam from which a single line of the image was reconstructed: this method is called *focused imaging*.

Nowadays almost all scanners use probes named *phased arrays*, for which complex acoustic fields can be generated by varying the amplitude, phase, delay and possibly frequency content of many piezoelectric elements distributed along the aperture [4]. In such setting, the wave equation for an homogeneous medium is often assumed to simplify the design of transmit sequences. This means that the speed of sound is constant and, for our purposes, taken equal to the average speed for soft tissues [15]: 1540 m/s.

The simplest US field transmittable from a transducer is given by using only one of the elements while keeping all the others off. If the element is small enough in all the spatial dimensions, compared to the wavelength, it is well approximated by a point source which produces a spherical wavefront. Sequentially firing each element and combining each of the obtained images is the principle behind the Synthetic Aperture Imaging (SAI) approach using single elements [11].

When a phased array is used, the Huygens principle (Sec. 1.1.1) is also employed to drive the elements in order to produce an arbitrary wavefield. For example, one can excite all the elements with exactly the same pulse $\phi(\omega)$. In this case, assuming that the elements are dense spatially and that the aperture is large enough, the

(a) Plane wave **(b)** Diverging wave **(c)** Focused wave

Figure 1.2: Illustrative examples of maximum pressure distribution for different kind of transmitted waves. Dynamic range is 20dB. The images have been made using Field II [1].

Huygens principle (Sec. 1.1.1) shows that a planar wave is produced [8]. By varying the delays, the plane wave can also be steered at different angles [16]. This kind of transmission defines the Plane Wave Imaging (PWI) method.

The fact that the aperture is not infinite and that the elements are spaced at a finite distance makes the plane wave approximation only valid in the vicinity of the array, called near-field: in the far-field and outside the aperture, those discrepancies from the ideal case distort the beam-pattern producing what are called transmit *sidelobes* and *gratinglobes* [13, 17].

Another method of interest in this thesis is constructed by imagining a single virtual point emitter located *behind* the actual transducer. In this case, once more assuming an homogeneous lossless medium, the first Born approximation can be used to calculate the time at which the virtual wave reaches each transducer element. Such time values are the used as delays for the transmission, again using the Huygens principle [18] to replicate a spherical wavefront, which has a greater energy compared to single element emissions.

Thanks to the reciprocity theorem [19, Section 7.2], the same argument can be applied to find out how to transmit a focused wave. In this situation, it is just necessary to imagine the desired focal point somewhere in the space to be imaged, calculate the received delays to each element considering the transducer as a receiver, invert the time axis and emit the desired wave using the newly calculated delays: we are basically using the reciprocity theorem by switching the source and receiver roles of the focal point and the transducer. Examples of different maximum pressure spatial distribution, for different type of transmitted waves, can be seen in Fig. 1.2.

More complex transmission can also be used, for example weakly focused waves or multiline focused waves [18]. Even random transmission can be useful, especially when compressed sensing methods are used for successive image reconstruction [20].

1.2.2 Beamforming

In the context of US, beamforming often refers to the act of reconstructing the acoustic impedance mismatch or the speed of sound spatial function $c(\mathbf{x})$ from the measured acoustic field. As already stated, this is an inverse problem which is often under-determined and therefore requires some additional prior knowledge for its resolution. We'll now review some common beamforming techniques with their underlying assumptions, as they will be key concepts for the next chapters.

In this section, we define the pressure field measured by the N_c channels as $\mathbf{x}(t) \in \mathbb{R}_c^N$. If the signals are sampled, then they are collected in the matrix $\mathbf{X} \in \mathbb{R}^{N_c \times N_t}$, with N_t equal to the number of recorded samples.

A common preprocessing approach in ultrasound is to evaluate the Hilbert transform the received data, also known as Radio Frequency (RF) data, along the fast time dimension t, to get an estimate of the I/Q signal. In the whole thesis we will all always assume that data are Hilbert transformed, so the signals can always be considered as complex, meaning that $\mathbf{x}(t) \in \mathbb{C}_c^N$ and $\mathbf{X} \in \mathbb{C}^{N_c \times N_t}$

We also define the operator $\hat{\mathsf{E}}_i$ as the operator that performs the sample average over the dimension i. As an example

$$\mathsf{E}_c[\mathbf{X}] = \frac{1}{N_c} \sum_c \mathbf{X}_C \tag{1.20}$$

gives the sample average across the elements for different times t.

Delay and Sum

Delay and Sum (DAS) is the most common approach to beamforming and is based on the first order Born approximation and is optimal, in the least squares sense, under the assumption that interference signals are i.i.d. Gaussian random variables. It is comprised two stages: a first one that translate temporally the signals recorded by the elements, and a second one that sums them at a given common time, usually indexed as $t = 0$.

Starting simple, let's assume that we are imaging an homogeneous background with a single spatially impulsive scatter, like a wire or a microbubble, located in position $\mathbf{x}_0$. We now transmit a plane wave characterized by a Gaussian enveloped sinusoidal pulse

$$\phi_{\text{inc}} = g_0 \left(\frac{\mathbf{k}_0^{\mathsf{H}} \mathbf{r}}{c_0} - t \right), \tag{1.21}$$

where

$$g_0(t) = \sin(\omega_0 t) \exp\left(-\frac{t^2}{2\sigma^2}\right), \tag{1.22}$$

ω_0 is the pulse frequency, σ is the pulse width and $\mathbf{k}_0^{\mathsf{H}}$ denotes the hermitian transpose of $\mathbf{k}_0$.

The intuitive explanation of the delays stage of DAS goes as follow [16, 10]. Assuming that the speed of sound is constant throughout the medium, the central point $g(0)$ of the transmitted wave will reach the scatter x_0 at time

$$\tau_1(\mathbf{r}_0) = \frac{\mathbf{k}_0^{\mathsf{H}}\mathbf{r}}{c_0}, \tag{1.23}$$

after which the scatter will emit a spherical wave. The distance that such wave has to travel from $\mathbf{r}_0$ to a generic transducer element located at $\mathbf{r}_1$ is given by $\|\mathbf{r}_1 - \mathbf{r}_0\|$. So we can conclude that the total time, called *beamforming delay*, required by the wave to be scattered back to a transducer element in $\mathbf{r}_1$ from a scatter in position $\mathbf{r}_0$ is given by [10]

$$\tau(\mathbf{r}_0, \mathbf{r}_1) = \frac{\mathbf{k}_0^{\mathsf{H}}\mathbf{r}_0 + \|\mathbf{r}_1 - \mathbf{r}_0\|}{c_0}. \tag{1.24}$$

From a more formal point of view, such simple scenario assumes a scattering function $m_a(\mathbf{r})$, as defined in eq. (1.13), equal to

$$m_1(\mathbf{r}) = A\delta(\mathbf{r} - \mathbf{r}_0), \tag{1.25}$$

where A is the scattering amplitude. In this case, the Born approximation is exact at the first order and the scattered field is given by [10]

$$\phi_{\text{sct}} = -\int_0^t \int_{\mathbb{R}^3} G(\mathbf{r} - \mathbf{r}', t - t') A\delta(\mathbf{r}' - \mathbf{r}_0) \frac{\partial^2 \phi_{\text{inc}}(\mathbf{r}', t')}{\partial t^2} \, d\mathbf{r}' dt' \tag{1.26}$$

$$= A \int_0^t G(\mathbf{r} - \mathbf{r}_0, t - t') \frac{\partial^2 \phi_{\text{inc}}(\mathbf{r}_0, t')}{\partial t^2} \, dt'. \tag{1.27}$$

Plugging in the formula for the free space Green's function of eq. (1.8) we get

$$\phi_{\text{sct}} = \frac{A}{4\pi\|\mathbf{r} - \mathbf{r}_0\|} \int_0^t \delta\left(t - t' - \frac{\|\mathbf{r} - \mathbf{r}_0\|}{c_0}\right) \frac{\partial^2 \phi_{\text{inc}}(\mathbf{r}_0, t')}{\partial t^2} \, dt'. \tag{1.28}$$

Substituting to ϕ_{inc} the incident wave of eq. (1.21) and using the shift property of convolutions with delta functions, we get the final result

$$\phi_{\text{sct}} = \frac{A}{4\pi\|\mathbf{r}-\mathbf{r}_0\|} g''\left(t - \frac{\mathbf{h}^{\mathsf{H}}\mathbf{r}_0}{c_0} + \frac{\|\mathbf{r}-\mathbf{r}_0\|}{c_0}\right), \tag{1.29}$$

which again shows the same delay.

Given the delays, the channel data are time shifted as

$$x_c(t) \to x_c(t - \tau(\mathbf{r}_0, \mathbf{r}_c)), \tag{1.30}$$

then sampled at time $t = 0$ to get, with a slight abuse of notation, $x_c = x_c(0)$. Lastly, the data for all the channels s are averaged together to get the desired estimate

$$p = \mathsf{E}_c[a_c^* x_c] = \frac{1}{N_c} \sum_c a_c^* x_c, \tag{1.31}$$

where $a_c \in \mathcal{C}$ are the weights. Defining the vector of sampled channels estimates as $\mathbf{x} = (x_1, x_2, \dots)^{\mathsf{T}}$ and the *apodization* vector as the unit norm vector $\mathbf{a} = (a_1, a_2, \dots)^{\mathsf{T}}$, the DAS estimate can be written as a dot product between the two vectors

$$p = \mathbf{a}^{\mathsf{H}}\mathbf{x}. \tag{1.32}$$

The choice of the apodization function is crucial for the performance of the beamformer, and its design can be studied under different point of views. Often, especially in the radar community, the apodization is set equal to the uniform vector $(1, 1, 1, \dots)^{\mathsf{T}}$, since the underlying assumption is that the signal of interest hits the array with the same strength and phase at all channels, after delays. Another common option is to set the apodization equal to a signal window function: such choice can be understood in terms of Point Spread Function (PSF) by approximating its lateral profile using the Fraunhofer approximation, which allows useful parallels with the Fourier transform that are extremely helpful in designing apodizations [13]. Another possibility is to consider the properties of the Hilbert space where the channel vector $\mathbf{x}$ belongs, an approach that we will heavily follow in this thesis.

Other beamforming methods

As an alternative to DAS, Lu and Cheng have shown [7, 8] that the use of limited diffraction beams, like plane waves, in transmit and receive allows the sensing of the spatial Fourier transform of the underlying image. This technique has been further sped up by in [21] using Non-Uniform Fourier Transform, which inherently remaps the k-space for image reconstruction. Other Fourier methods have also been developed, for example the adaptation of Stolt frequency-wavenumber migration method for PWI by Garcia et al. [22], initially developed for seismic imaging [23], which yielded fastest computational time, thanks to the use of FFT, and better lateral resolution compared to DAS. Bernard et al. have also proposed a Fourier beamforming method based on the Fourier Slice Theorem [24], which linked different receive delay strategies to the reconstruction of different slices of the k-spectrum of the imaged object, further improving lateral resolution. Fourier methods have also been extended for imaging with diverging waves [25].

In [26], the authors have shown that the Fourier transform of the distortion function associated with the DAS delays has fast decaying properties, which allows to reduce the spectral support effectively required for beamforming. That in turns permits to avoid the oversampling required by the precise delays used in temporal DAS reconstruction, reducing the required sampling rate to the temporal Nyquist limit. They also show that beamforming in the Frequency domain allowed for further dramatic reduction of sampling sate at sub-Nyquist level using compressed sensing reconstruction, if the beamformed signals are assumed to follow a Finite Rate of Innovation model. Since then, many beamforming approaches began to use sparse priors for ultrasound image reconstruction [27, 28], including for SAI [29] and PWI [30, 31], with the purpose of improving image quality by computing a more robust solution to the inverse scattering problem. Lastly, the advantage of using randomly apodized and delayed waves with the compressed sensing framework has been shown in [20].

1.2.3 Doppler imaging

The signal $p(\alpha) = p_{f\alpha}$ associated with a beamformed pixel, at different transmissions α, is usually referred as Doppler signal or Pulsed Wave Doppler (PWD) signal. The reason for this name is that it shares with Continous Wave Doppler (CWD) the fundamental property of the frequency shift associated to a moving target, which for a linear scatter having an axial velocity of v is

$$\Delta\omega = \frac{2\omega_0 v}{c}, \tag{1.33}$$

with ω_0 equal to the transmitted frequency. It turns out that for many transmitted pulses with the same shape, the frequency of the slow-time signal $p(\alpha)$ is given by the same formula with a rescaled fundamental frequency [4]

$$\Delta\omega = \frac{2\omega_0 v}{c\omega_{PRF}}, \tag{1.34}$$

where ω_{PRF} is the pulse repetition frequency: this is however an idealized model where the transmitted wave is assumed monochromatic, while in the real case the wideband nature of the pulse will negatively affect the Doppler estimate (see [32] for a detailed analysis). Knowing the frequency shift, one can invert the equations to estimate the velocity of the scatter. The PWD technique has been successfully used for ultrafast ultrasound [33], where the authors noted how the ratio of maximum depth and fastest flow pose an upper bound on the number of plane wave to be used if one wants to avoid aliasing.

To find the Doppler frequency shift, one of the most used techniques relies on estimating the rate of change associated with the demodulated IQ Doppler signal. In [34], the authors show that the mean frequency shift is given by the rate of change of the autocorrelation $R(\tau)$ of the signal

$$j\Delta\omega = \frac{\frac{d}{d\tau}R(0)}{R(0)}, \tag{1.35}$$

where, after decomposing the autocorrelation in magnitude $\|R(0)\|$ and phase part $\phi(\tau)$, that is $R(\tau) = \|R(0)\|e^{j\phi(\tau)}$, the calculation is shown to simplify to

$$\Delta\omega = \frac{\phi(T)}{T}, \tag{1.36}$$

with $T = 1/\omega_{PRF}$. Another widely used method for determining the mean Doppler frequency has been proposed by Loupas et al. [35], where a 2-dimensional Fourier transform has been applied in fast time (depth) and slow time (pulse transmissions) to find the average frequency, with the aim reducing the bias of one dimensional autocorrelators. In a similar fashion, Torp and Kristoffersen [36] proposed a velocity matched spectrum method, which uses the Radon transform and the related 2D Fourier slice theorem for Doppler frequency estimation. This approach is capable of removing the aliased spectral components and further improves performance compared to the above methods. The velocity estimation bias associated with the above methods has been studied in [37] for contrast enhanced sequences, where the reduction in velocity bias for 2D methods compared with 1D autocorrelators has once more been verified. Nikolov and Jensen [38] have also shown that the application of recursive reconstruction allows directional Doppler sensing, paving the path for ultrafast flow imaging.

1.2.4 Compounding

Coherent compounding

Coherent compounding is a widely used method to improve Signal to Noise Ratio (SNR) and contrast of an ultrasound image, by coherently averaging images reconstructed using different transmissions [16]. Intuitively, compounding builds on the fact that, when static targets are imaged, the reconstructed signal for a given location is constant regardless of the transmission used, or at least it can vary in amplitude but not in phase. On the other hand, interference signals that are located away from the region of interest will be delayed differently for different transmissions: assuming that they are random, and more precisely that they can be modelled as i.i.d. zero mean Gaussian variables, then taking the average minimizes their contribution to the final image. This is clearly an over-simplification, since the deterministic presence of sidelobes and gratinglobes in ultrasound images imply that at least the zero-mean assumption is invalid. Alternatively, the effect of compounding can be studied in the Fourier domain [39]. Focusing on the Doppler signal, compounding boils down to low-pass filtering and sub-sampling [40].

Mathematically, compounding is simply given by

$$s = \mathsf{E}_{\alpha}[p] = \left| \frac{1}{T} \sum_{\alpha} p_{\alpha} \right|^2 \tag{1.37}$$

where $\alpha \in \{1, \ldots, T\}$ denotes each transmission, T is the total number of transmissions and s is the final pixel value; the reason behind taking the squared absolute value is that we are only interested in the magnitude of the signal for displaying, so the phase is only exploited during the compounding operation. Lastly, such estimated intensity is often displayed using decibel units, leading to

$$\hat{s} = 10 \log_{10}(s) \tag{1.38}$$

If we define the weight vector $\mathbf{q} = \frac{1}{T}(1, 1, \ldots, 1)^{\intercal} \in \mathbb{R}^T$, which we call transmit apodization, and the data vector $\mathbf{p} = (p_1, p_2, \ldots, p_T)$, then the above computation is equivalent to

$$s = |\mathbf{q}^{\intercal}\mathbf{p}|^2 = \mathbf{p}^{\intercal}\mathbf{q}\mathbf{q}^{\intercal}\mathbf{p} = \mathbf{p}^{\intercal}\mathbf{Q}_c\mathbf{p}, \tag{1.39}$$

with $\mathbf{Q_c} = \mathbf{q}\mathbf{q}^\intercal$, that is for example

$$\mathbf{Q}_c = \frac{1}{T^2} \begin{pmatrix} 1 & 1 & 1 & \dots \\ 1 & 1 & 1 & \dots \\ 1 & 1 & \ddots & \\ \vdots & \vdots & & \end{pmatrix} . \tag{1.40}$$

Note that the matrix $\mathbf{Q}_c$ is hermitian symmetric and positive semidefinite, i.e. $\mathbf{v}\mathbf{Q}_c\mathbf{v} \geq 0 \ \forall \mathbf{v}$, therefore the result will necessarily be a positive real number as expected.

Recall that, *for a single frame*, coherent compounding is extracting the DC component of the Doppler signal, as it is taking the average of it. This is an important characteristic that underlies the assumption of constant amplitude for the signal received from the scatterer of interest. While this is approximately true when imaging a region which has constant properties over time, it may be an inaccurate approach when blood flow is imaged, due to the flow itself that feeds different scatters at different times in the same spatial region.

Incoherent compounding and Power Doppler

In case of incoherent compounding, we neglect the phase information also during the frame averaging stage, by finding

$$s = \frac{1}{T} \sum_{\alpha} |p_\alpha|^2 , \tag{1.41}$$

that is

$$s = \frac{1}{T} \mathbf{p}^\mathsf{H} \mathbf{p} = \frac{1}{T} \left(\mathbf{p}^\mathsf{H} \mathbf{I} \mathbf{p} \right) , \tag{1.42}$$

with $\mathbf{I}$ equal to the identity matrix. Clearly, what we are finding here is the norm of the Doppler vector $\mathbf{p}$, which is invariant under basis change and therefore is the same as estimating the average power in the Fourier domain.

While, by all means, incoherent compounding should be another way to call what is know in the ultrasound community as Power Doppler (PD) estimation, usually the term PD is given to the estimation of the Doppler signal power of multiple frames, where *each frame* is made of multiple coherently compounded transmissions. That is, denoting s_f as the estimate of the coherently compounded pixel value at the

f-th frame, then the PD value is given by

$$PD = \frac{1}{F} \sum_f |s_f|^2, \tag{1.43}$$

where F is the total number of frames. If we want to formulate this operation again using a bilinear form, we just have to consider the vector $\mathbf{p}$ as the collection of all the pixel values for different transmission *and* different frames, so that if $p_{f,i}$ is the DAS estimate at the i-th transmission of frame f, we have $\mathbf{p} = (p_{1,1}, p_{1,2}, \ldots, p_{1,T}, p_{2,1}, \ldots)^\mathsf{T}$. Then, the PD estimate is given by the block matrix

$$PD = \mathbf{p}^\mathsf{H} \begin{pmatrix} \mathbf{Q}_c & \mathbf{0} & \mathbf{0} & \ldots \\ \mathbf{0} & \mathbf{Q}_c & \mathbf{0} & \ldots \\ \mathbf{0} & \mathbf{0} & \mathbf{Q}_c & \ldots \\ \vdots & \vdots & \vdots & \ddots \end{pmatrix} \mathbf{p}. \tag{1.44}$$

Once more, we find that the quadratic form matrix is positive semidefinite and, by consequence, produces only positive real estimates.

General formulation of frame compounding

Clearly, different choices of the $\mathbf{Q}$ matrix lead to different kind of estimations, as we have seen in the previous sections. The use of a semi-definite matrix also leads to the desirable property that the resulting estimate is necessarily real and positive. However, this need not be the case. In [41], the authors have used the lagged sampled autocorrelation of the Doppler signal to construct perfusion images: this boils down to the use of the following $\mathbf{Q}$ matrix

$$Q_{ij} = \begin{cases} 1 & \text{if } i - j = \tau \\ 0 & \text{otherwise} \end{cases}. \tag{1.45}$$

where τ is the desired lag. For example, in case of first lag autocorrelation, where $\tau = 1$, the matrix is given by

$$\mathbf{Q} = \begin{pmatrix} 0 & 1 & 0 & 0 & \ldots \\ 0 & 0 & 1 & 0 & \ldots \\ 0 & 0 & 0 & 1 & \ldots \\ 0 & 0 & 0 & 0 & \ldots \\ \vdots & \vdots & \vdots & \vdots & \end{pmatrix}. \tag{1.46}$$

We quickly remark that, being $\mathbf{Q}$ a non-definite matrix, the result of the bilinear product can have an arbitrary phase. This is in turn may have detrimental effects on the quantification of signal intensity. We will look these issues in greater detail in Chapter 4.

1.2.5 Adaptive Beamforming

Another way of looking at the PD estimate, which is far more common in the ultrasound and radar community, is given by taking into account both the beamforming process and the spatial power spectral estimation. Going back to eq. (1.41), we can explicitly write the value of s using eq. (1.32)

$$s = \frac{1}{T}\sum_{\alpha} |p_\alpha|^2 = \frac{1}{T}\sum_{\alpha} \left|\mathbf{a}^{\mathsf{H}}\mathbf{x}_\alpha\right|^2 = \frac{1}{T}\sum_{\alpha} \mathbf{a}^{\mathsf{H}}\mathbf{x}_\alpha\mathbf{x}_\alpha^{\mathsf{H}}\mathbf{a}. \tag{1.47}$$

Because the receive apodization $\mathbf{a}$ is the same for each transmission α, we can move the sum inside to get

$$s = \mathbf{a}^{\mathsf{H}}\left(\frac{1}{T}\sum_{\alpha} \mathbf{x}_\alpha\mathbf{x}_\alpha^{\mathsf{H}}\right)\mathbf{a}. \tag{1.48}$$

Now, we define the sample covariance matrix $\mathbf{R}$ as the terms on the inside of the parenthesis

$$\mathbf{R} = \frac{1}{T}\sum_{\alpha} \mathbf{x}_\alpha\mathbf{x}_\alpha^{\mathsf{H}}, \tag{1.49}$$

which contains all the unlagged second order statistics of the received channels data, to get the well known power estimate equation

$$s = \mathbf{a}^{\mathsf{H}}\mathbf{R}\mathbf{a}. \tag{1.50}$$

Minimum Variance beamforming

The key idea of many adaptive methods is to use the structure of the covariance matrix in order to adapt the apodization vector to achieve improved performances, usually in terms of interference rejection. The first and most famous approach goes back to Capon [42] and has been adapted for both focused and unfocused ultrasound imaging [43, 44, 45, 46]. It has also been shown, with appropriate modifications such as diagonal loadings, that it is also optimal in the Maximum Likelihood (ML) sense when the interference and noise sources are uncorrelated and Gaussian random variables [47]. We remark that the way we estimate the covariance matrix is not the only one possible, and indeed Minimum Variance (MV) techniques in ultrasound very often estimate the cross correlation matrix using samples in the fast time (or depth) rather than in the Doppler domain, since they are interested in imaging quasi-stationary targets; however, this only changes the resulting estimate of $\mathbf{R}$ and all the considerations made in the next of the section will be equally valid, unless specified.

The idea behind the Capon method, also widely know as MV beamforming, is to find an apodization $\hat{\mathbf{a}}$ that doesn't distort the signal of interest while it removes as much as possible the signals coming from other sources, which is measured in terms of power. The first goal is achieved by constraining the solution to have and unitary response in the direction of interest $\mathbf{a}$. With such a constraint, under the assumption of uncorrelated scatterers, minimizing the sensitivity to other sources is equivalent to minimizing the total estimated power, so the MV problem is formulated as

$$\min_{\hat{\mathbf{a}}} \hat{\mathbf{a}}^{\mathsf{H}}\mathbf{R}\hat{\mathbf{a}}, \qquad \text{with } \mathbf{a}^{\mathsf{H}}\hat{\mathbf{a}} = 1. \tag{1.51}$$

The solution can be found using the method of Lagrange multipliers and is given by

$$\hat{\mathbf{a}} = \frac{\mathbf{R}^{-1}\mathbf{a}}{\mathbf{a}^{\mathsf{H}}\mathbf{R}^{-1}\mathbf{a}}. \tag{1.52}$$

By substituting the MV apodization to the PD estimation in eq. (1.50), we see that the power estimate of MV is given by [42]

$$s = \hat{\mathbf{a}}^{\mathsf{H}}\mathbf{R}\hat{\mathbf{a}} = \frac{1}{\mathbf{a}\mathbf{R}^{-1}\mathbf{a}} \tag{1.53}$$

Modifications of the minimum variance method

The minimum variance approach suffers from heavy performance degradations when an imprecise knowledge of the true steering vector is present, as is often the case for ultrasound. To mitigate this intrinsic tendency of attenuating the source of interest, many methods have been developed both in the ultrasound and radar community. For example, creating a virtual array by averaging L neighbouring channels or substituting the covariance matrix with a diagonally loaded one [44] has been show to improve the robustness of the method, although the choice of ad hoc user parameters is required.

Asl and Mahloojifar [48] decomposed, via Singular Value Decomposition (SVD), the covariance matrix and then useed the intuition that the high coherence of the main-lobe signal will make it spread over a limited number of eigenvalues, in contrast to a sidelobe signal that will be probably contained over a larger support of the spectrum. They therefore use the eigenvectors associated with the highest eigenvalues to construct a signal subspace on which the MV aperture is projected. In this way, they find that image contrast is improved with respect to other MV approaches. This is however an assumption that is hard to justify in the context of vascular imaging, as the signal from small vessels may be located away from the upper part of the matrix spectrum, so that filtering the lowest eigenvalues can also filter out the signal of interest. Lastly, it has also been shown that a Forward-Backward regularization of the cross correlation matrix further improves the resolution and mainlobe amplitudes of reconstructed images, while being less dependent on free user settings like the diagonal loading level [49].

The MV approach has also been extended to SAI in [46], by decomposing the received signal in sub-bands using the Fourier transform and then applying it to each band separately. The results show that the proposed method improves contrast and is at most as sensitive as DAS to mismatches of the steering vector. Another approach followed by the same authors for High Frame Rate (HFR) US, which is of interest for this thesis, is given by the Transmit-Receive MV beamforming method [50], where the finite length of the input is used to construct a matrix $\mathbf{X} \in \mathcal{C}^{N_c \times N_\alpha}$, in which the first dimension is the number of channels and the second dimension the number of acquired transmissions. This allows to build two different correlation matrices

$$\mathbf{R}_c = \mathbf{X}\mathbf{X}^{\mathsf{H}}, \qquad \mathbf{R}_\alpha = \mathbf{X}^{\mathsf{H}}\mathbf{X}, \tag{1.54}$$

that allows two different MV calculations to be carried out: one in the channel domain and another in the transmit domain, where the steering vector associated to the transmit domain is given by the weights used during compounding. The results show an improved resolution compared to the same method applied only in the channel domain.

1.2.6 Correlation based methods

With the purpose of mainly reducing the effects of interferences on mainlobe signals, there have been several approaches that used some form of cross correlation between portions of the received signals to filter out unwanted echoes. Li and Li were among the first to introduce a coherence factor for US beamforming [51], by generalizing it as the ratio of low-pass energy over the total energy of the delayed signals, showing an improved clutter rejection and contrast, even when phase aberration are present once those have been properly corrected. An approach called Dual Apodization with Cross-correlation (DAX) uses the fast-time coherence of two different apertures, represented by two different apodization vectors, to estimate a weight matrix given by the coherence of the backscattered and delayed signals [52]; the weight matrix is then multiplied to the B-mode image, improving contrast. The methods has then been further improved by using complementary phase apodization in order to reject side and grating lobes [53].

Camacho et al [54] have introduced and tested in-vitro the concept of Phase Coherence Factor (PCF), where the correlation of the phase signal between different channels is used as weight, instead of the amplitude coherence, showing a dramatic interference reduction. The phase coherence method has also been extended to work with sub-aperture beamforming [55]. In a similar way, Lediju et al. [56] have defined the coherence function between channels at a distance m as the normalized average cross correlation

$$\hat{\mathbf{R}}(m) = \frac{1}{N-m} \sum_{i}^{N-m} \frac{\mathsf{E}_t[x_i(t) x_{i+m}^*(t)]}{\sqrt{\mathsf{E}_t[\|x_i(t)\|^2 \mathsf{E}_t[\|x_{i+m}(t)\|^2]}}, \tag{1.55}$$

and the used the average across M lags to create an image, which shows increased SNR and Contrast to Noise Ratio (CNR).

1.3 Contrast Agents

We've seen how the contrast in a beamformed ultrasound image is a function of the speed of sound spatial variations, which in turns depends mainly on density and elasticity. When blood flow is imaged, US signals of interest are generated by the scattering of red blood cells. Such signals are generally weak compared to the surrounding tissue structures when imaged at clinical frequencies [57]. This makes blood vessels appear as dark structures in an ultrasound image. Moreover, imaging of small vessels is heavily limited due to their small size compared to the US wavelength at clinical frequencies. Historically, the difference in motion magnitude between tissue and flowing blood has been exploited to enhance the vasculature using Doppler methods [58]: while this is still an indispensable tool for gathering information about the dynamics of the cardio-circulatory system, its basic implementations still confine it to cardiac and big vessels studies.

The fortunate accidental discovery of the large echogenicity of micrometer sized bubbles gave the tool to surpass such limitations [59], whose use marked the beginning of Contrast Enhanced Ultrasound (CEUS). We reviewed CEUS in [2], from which most of this section is based.

Microbubbles are injected in the blood stream and their size, typically smaller than 7μm in order to pass trough the pulmonary capillaries, sets their resonant frequency in the same spectrum range as used in medical ultrasound, that is 1 to 15MHz. To enhance their stability and lifetime by reducing gas leakage, but also to manipulate their mechanical properties, Microbubble (MB) are often coated with a lipidic shell.

The high scattering potential and small size of MBs gives unprecedented opportunities to image both macro and micro-vasculature in vivo and in real time [60], for example highlighting pathological markers in liver, heart, brain, breast and even the lymphatic system, virtually without any safety risk [61, 62]. Lastly, the sparse nature of microbubble infusions gave the opportunity to apply localization techniques which gave the possibility to break the diffraction (or Gabor) limit, creating super resolution images of the vasculature at micrometer scale [63].

1.3.1 Acoustical properties of microbubbles

Acoustic scattering by a MB occurs due to its size oscillation in response to an external pressure change. The relatively high compressibility of its core is responsible for the strong scattering at frequencies around the resonance. As the size of MBs is usually two order of magnitude smaller than the US pulse wavelength, few micrometer for the first versus hundreds of micrometers for the latter, this phenomenon is often mechanically modelled as a global pressure variation, assuming spherical symmetry holds and therefore the MB acts as a monopole source. With such symmetry, the Rayleigh-Plesset equation arise form the Navier–Stokes equations assuming an uncoated microbubble of polytropic gas lying in an infinite inviscid incompressible fluid, with low amplitude incident pressure waves [64]:

$$\left(\frac{\partial^2 r}{\partial t^2}\right) r + \frac{3}{2}\left(\frac{\partial r}{\partial t}\right)^2 = \frac{p - p_\infty}{\rho}, \tag{1.56}$$

where r is the microbubble radius, p is the pressure at the bubble-liquid interface, p_∞ is the pressure far away from the bubble and ρ is the fluid density. The pressure wave scattered by the MB is found as

$$p_s = \frac{\rho r}{d}\left[2\left(\frac{\partial r}{\partial t}\right)^2 + r\frac{\partial^2 r}{\partial t^2}\right], \tag{1.57}$$

where d is the distance from the bubble.

Naturally, the Rayleigh-Plesset equation equation is an idealized model that helps to grasp the fundamental characteristics of MB dynamics, but is far from modeling the real scenario: shell effects, bubble deflation, rupture, viscosity, incident frequency, proximity to vessel walls etc., all have to be taken into account to correctly predict the acoustic response. Many modified Rayleigh models have been developed for such purpose, but as this is a complex and interesting field of research outside the scope of this thesis, we refer to [65] and references therein for a more comprehensive review.

1.3.2 Contrast imaging techniques

Very often, contrast agents are used to highlight the vasculature alone discarding any information about the surrounding anatomical structure. This is especially true when small vessels have to be imaged. Such need calls for contrast specific transmission and processing techniques capable of suppressing tissue signal, commonly referred as *clutter*, while enhancing MB generated waves.

A class of methods, based on the concept of harmonic imaging, rely on the fact that tissue structures imaged at moderate Mechanical Index (MI) obey the linear wave equation and therefore the acoustic response of a spatial location can be modelled as a linear filter, as done for example in eq. (1.18). This means that, for moderate pressures, the spectrum of the received echoes has the same support on the temporal frequency axis as the transmitted wave.

On the other hand, the presence of squared terms in the Rayleigh-Plesset equations highlights the non linearity of the MB response to external pressures. This, in turn, means that the spectrum of the scattered wave will have a different support compared to the incident wave: if we model the microbubble as a simple memoryless non linear system, we can safely assume that harmonics will be generated [66]. Such prediction has been experimentally verified and lies as the basic principle of harmonic imaging of microbubbles. We remark, however, that in order for the harmonic signal to have a detectable strength, microbubbles must be driven at frequencies close to the resonant one and anyhow with a signal of strong enough amplitude, although not too powerful such that MB rupture happens.

The first most obvious method to separate tissue from contrast signal is given by high-pass filtering the received echoes at a frequency above the fundamental, but below some harmonics which are in the pass-band of the transducer. This class of

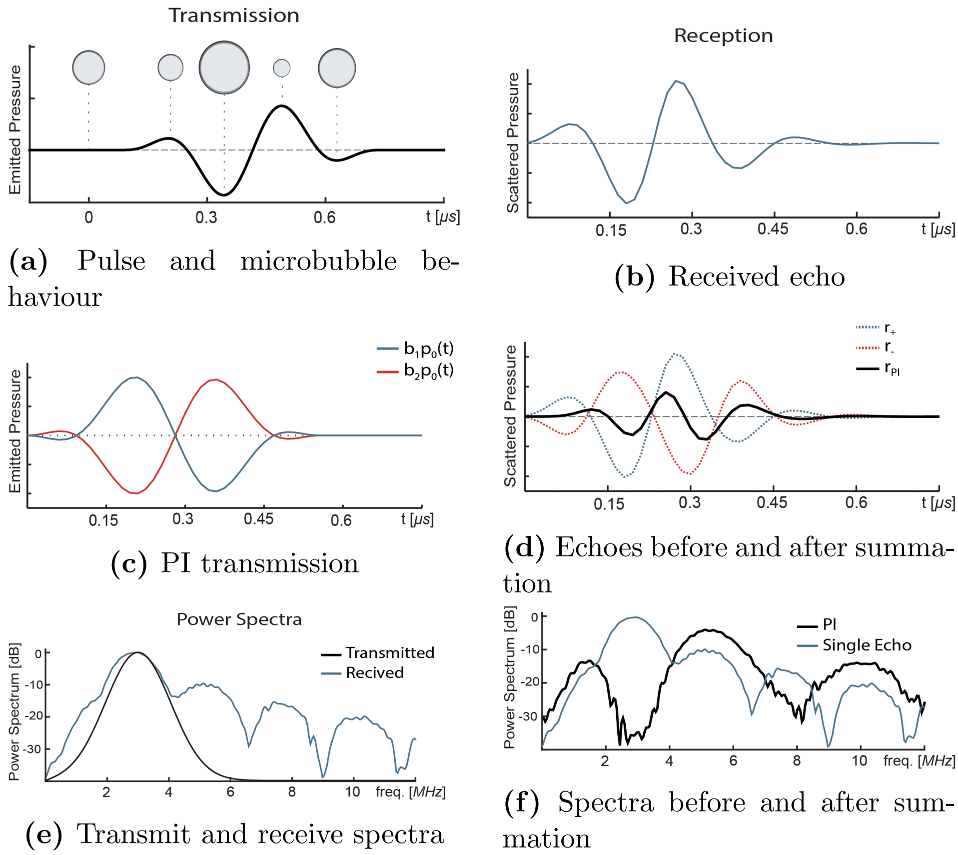

(a) Pulse and microbubble behaviour

(b) Received echo

(c) PI transmission

(d) Echoes before and after summation

(e) Transmit and receive spectra

(f) Spectra before and after summation

Figure 1.3: Principles of MB detection. The first row shows (a) microbubble oscillation in response to an external US pressure field, the scattered ultrasound wave (b) The second row illustrates the principle of Pulse-Inversion detection, where (c) depicts positive and negative transmitted pulses and (d) shows the MB responses to them; The last row shows the received spectra before (e) and after (f) pulse summation. Adapted from [2].

methods is called *contrast harmonic imaging* [67].

However, the resolution of an ultrasound image beamformed using standard linear techniques is bounded by the length of the transmitted wave, which in turns is inversely proportional to its spectral extent, due to the Gabor limit. In practice, to have good resolution very short pulses with wide spectra are transmitted, which makes the linear spectrum leak into the harmonic regions. In such cases, a satisfactory suppression of the clutter signal requires such a high cut-off frequency that first harmonics will be attenuated too.

Multipulse transmissions

Multipulse techniques are an elegant method developed to overcome this limitation. The key idea is to transmit multiple waves and sum them with different weights, in order to preserve some harmonics of interest [68].

Assuming that many monochromatic waves $\phi_k(t)$ are emitted,

$$b_k\phi_k(t) = b_k\phi_0 e^{j\omega_0 t}, \qquad b_k = \|b_k\| e^{j\theta_k}, \tag{1.58}$$

then by modeling either clutter or MB as memoryless systems, the echo will be given by its Taylor expansion

$$r_k(t) = \sum_n a_n \left[b_k^n \phi(t)\right]^n, \tag{1.59}$$

where the coefficients a_n depend on the scattering source: for tissue, the assumption that no harmonics are generated gives $a_n = 0$ for $n > 1$, while for MB we assume that at least the first coefficients are non zero. After transmitting K pulses, the received echoes are added together by a weighted sum

$$r_{sum}(t) = \sum_{k=1}^{K} \lambda_k r_k(t) = \sum_{n=1}^{K} \lambda_k \sum_n a_n \left[b_k^n \phi(t)\right]^n. \tag{1.60}$$

Depending on how the transmission coefficients vector $\mathbf{b} = (b_1, b_2, \dots)$ and the received weights vector $\lambda = (\lambda_1, \lambda_2, \dots)$ are chosen, the contribution of different harmonics is kept. For example, in Pulse Inversion (PI) two pulses with opposite phase are transmitted, $\mathbf{b} = (1, -1)$, and then coherently summed together, $\lambda = (1, 1)$ [66]. The final sum is therefore given by

$$r_{sum}(t) = \sum_n a_n \left[1^n \phi(t)\right]^n + \sum_n a_n \left[(-1)^n \phi(t)\right]^n = \begin{cases} 2a_n\phi^n(t) & n \text{ is even} \\ 0 & n \text{ is odd} \end{cases}, \tag{1.61}$$

which by consequence only keeps the contribution of the even harmonics while rejecting the odd ones, including the fundamental frequency and thus clutter. A review of many different Multipulse methods is given in [68], while an example of the acquisition using PI is given in Fig. 1.3.

We emphasize that the memoryless model only holds for a small number of transmissions, because microbubbles change when many pulses are applied, due to effects like deflation, shell rupture and destruction [69, 70]. Those source of variability, however, can also be exploited to discriminate contrast signals.

Motion based methods

Another class of methods, which works for CEUS as well as standard US are based on the fact that blood flow is usually associated with speeds higher than the bulk motion of surrounding tissues. For example standard Colour Doppler and Power Doppler methods, both continuous and pulsed, are both readily usable for highlighting contrast signals [71].

However, the previous multipulse framework can also be exploited to improve clutter discrimination by Doppler techniques An example of that has been given by Tremblay-Darveau et al [60]. The interesting fact is that if different pulses are transmitted using the PI scheme, the Doppler spectrum of a linear scatter will be circularly shifted by $\omega_{PRF}/2$: in practice, if it was around the DC component it will then sit around the Nyquist frequency. However, this behaviour is not matched by the second harmonic if the model in eq. (1.59) holds, therefore we have the following spectral shift for the n-th harmonic

$$\Delta\omega = \begin{cases} \dfrac{2\omega_0 v}{c\omega_{PRF}} & n \text{ is even} \\ \\ \dfrac{2\omega_0 v}{c\omega_{PRF}} + \dfrac{\omega_{PRF}}{2} & n \text{ is odd} \end{cases} . \tag{1.62}$$

This frequency splitting allows the use of simple low pass filters to isolate MBs in moderate flows, such as in perfusion.

Other motion based methods based on matrix decomposition have also been used to evaluate the spatial and temporal coherence of multiple frames. An important and recent approach, which yielded impressive results, is given by SVD of the entire beamformed video sequence [72].

1.3.3 Clinical applications of contrast agents

Microbubbles are an incredibly valuable tool for assessing, monitoring and treating a large pool of diseases that are connected with the cardiovascular system. In cardiac applications, they can be use in conjunction with destruction-imaging sequences to evaluate the dynamics of endocardial perfusion, which is an indicator of health of the heart muscle [73], or to help highlighting the cardiac walls during stress studies [74] and even achieve automatic tracking and segmentation of the cardiac walls [75]. Recently, the combined use of microbubbles and HFR imaging has been demonstrated to show and help quantify the flow dynamics in the cardiac chambers [76].

As a vascular contrast agents, microbubbles are also useful in detecting disease condition in kidney, such as arterial stenosis or perfusion deficit, thanks to the lack of contrast enhancement of the interested regions. By exploiting the dynamics of bolus injections, microbubbles have been found also helpful in imaging and characterizing liver lesions [77], thanks to the different vascular network that come with various degrees of malignancy and the consequent different wash out time associated [62].

Another exciting possibility comes from engineering the MB coating or by attaching specific molecules to its shell which are specific to a molecular target of interest, targeting contrast agents to disease markers, like angiogenic proteins expressed in the vasculature surrounding cancer sites, which makes molecular imaging and localized drug delivery possible [61, 78, 79]

For example, angiogenesis is an important marker with respect to diseases [80] and in particular to the growth and malignancy associated with tumours: targeting microbubbles to integrins that are expressed during neovascularization, it has been possible to non-invasively evaluate tumour angiogenesis [81]. Some useful reviews of contrast agent applications are given by Cosgrove [62], Lindner [82] and Stewart [83].

Chapter 2

Effects of motion on contrast imaging

2.1 Background

Unfocused or partially focused waves used in High Frame Rate (HFR) Ultrasound (US) are great methods to image fast moving targets such as in cardiovascular settings [84], both with and without contrast agents, because of the large frame-rate improvement they can achieve. Diverging waves have been used to generate 3D Doppler sequences of the heart [85], obtain cardiac strain images [18], imaging and quantifying myocardial perfusion [76] and to get blood flow velocity mappings [86, 87].

When imaging the heart, microbubbles can be used to evaluate the complex flow pattern in the chambers [76] or to assess anomalies of the myocardial perfusion [88]. In the latter, the discrimination of contrast and clutter signal is a key step in the process of quantifying cardiac microvasculature.

Due to the fast motion of the cardiac walls and the large depths that must be imaged, the number of pulses that can be combined to form an image is much more limited compared to other applications. The large depths also require low frequency transmission, which in turn impose a large pulse bandwidth to achieve satisfactory axial resolution, limiting the use of temporal filtering for clutter rejection. Therefore, simple multipulse contrast enhancing schemes are often employed: in this chapter, we will look at Pulse Inversion (PI).

The coherent sum of the multiple received echoes used to isolate microbubble signals (see Sec. 1.3.2) is however sensitive to the interpulse clutter motion, because of the resulting temporal shift of the echoes, which modifies their phase relationship [89, 90]. Furthermore, the compounding methods used to improve the image quality of unfocused transmissions (see Sec. 1.2.4 and [16]) are also affected by motion: Denarie et al. [17] demonstrate how even moderate motions, combined with compounding, result in artefacts both in terms of the shape of the Point Spread Function (PSF), loss of image contrast and resolution reduction.

We therefore hypothesize that the joint use of HFR and Contrast Enhanced Ultrasound (CEUS) will also suffer an even stronger reduction of image quality when the imaged targets are moving at a significant speed. Indeed, a recent study [91] has investigated the impact of out of plane motion on HFR amplitude modulation images in vitro with a linear array probe, finding a reduction of intensity which gets more significant with increased number of compounded frames.

Different processing methods can be used to mitigate the problems of simple PI. For example, nonlinear Doppler techniques have been developed specifically for detecting moving microbubbles using inter-pulse microbubble motion during multi-pulse methods [66, 92]. However, those methods are designed for single steering angles and cannot be directly used for motion correction of compounding images.

Another way to reduce such artefacts is to estimate the motion field and compensate for it before the coherent compounding is performed. Many of the currently available motion compensation methods rely on either tissue or blood Doppler signal, cross-correlation estimates, registration of beamformed images both for B-mode and for Doppler imaging [17, 93]. In the field of ultrafast cardiac imaging, motion compensation prior to compounding has been studied in [94], where the importance of the steering angle sequence is highlighted. For Color Doppler images, the authors of [40] show how coherent compounding acts as a low-pass filter, introducing velocity estimation bias and compensated for it after estimating 2D motion with the least square method of [95].

In this chapter, we investigate the effect of motion on PI CEUS cardiac images using both simulation and in-vivo experiments, showing the intensity changes that occur together with some significant examples of artefacts. Furthermore, we perform preliminary evaluation of a motion compensation algorithm and demonstrate how such algorithms might be a useful tool in this context.

	Simulations	**In-vivo**
Frequency (cycles)	1.5 MHz (3)	1.5 MHz (3)
Angle range	30	60
Number of angles	11 (×2 PI)	11 (×2 PI)
MI	0.05	0.08
Frames	-	1000
Pulse repetition frequency	5500 Hz	5500 Hz

Table 2.1: Settings for simulations and in-vivo acquisitions.

2.2 Materials and Methods

In this work, which I have jointly conducted with Dr. Matthieu Toulemonde and Dr. Yuanwei Li, we have implemented HFR CEUS using diverging waves with coherent compounding [96, 94].The waves are transmitted with a Pulse Repetition frequency (PRF) of 5500Hz using 11 steered waves. Since PI is used to enhance contrast signals, a single frame is made by a total of 22 transmitted waves and their reconstructed images are summed to form the final image.

The transducer used is a P4-1 with an aperture of 2.83cm and a total of 96 linearly spaced elements. The transmit frequency is a Gaussian enveloped sinusoid at $1.5MHz$ of 3 cycles. The transmitted Mechanical Index (MI) is of 0.08 and 0.05 for in-vivo and simulations respectively: note that the MI for the in-vivo data is defined as usual using the maximum peak negative pressure at any location of the image [4, Sec. 14.4.3], while for the simulation is measured at the microbubble location. The acquisition settings are summarized in Tab. 2.1. Given that the cancellation of the fundamental component will not be perfect, we process the Radio Frequency (RF) data using a high pass zero phase 5-th order Butterworth filter having a cut-off frequency of 2.7MHz to further remove clutter, both in vivo and in simulations.

2.2.1 Simulations

When perfusion is imaged, clinician often rely on the signal emitted from a few sparse microbubbles, like in the first seconds of a destruction-replenishment study [88]. For this reason, simulations are done using a single microbubble, and if not differently specified they are placed 5cm below the transducer surface and are moving at a speed of 25cm/s. The simulated model assumes a homogeneous lossless medium in which the Born approximation is perfectly valid. The pressure variation, $p(t)$, experienced by the microbubble is simulated in Field II [1, 97], by recording the acoustic field at

Radius range	empirical distribution from [98, Fig. 7]
Shell viscosity	15 nPa,s
Polytropic gas constant	1.095
Interfacial tension coefficient	0.0728 kg/s
Elasticity	1 N/m

Table 2.2: Microbubble mechanical parameters used for simulations.

the microbubble location when a transducer having the same characteristics as the P4-1 is used for transmission.

The pressure function is then used to numerically integrate the differential equations of the Marmottant model [99], where the model has been simplified by not considering buckling and rupture, since moderate pressures are considered in simulation. The microbubble mechanical parameters were extracted from the empirical study of SonoVue done in [100], summarized in Tab. 2.2, while the size of each microbubble has been randomly chosen for each simulation in accordance to their experimental size distribution [98].

Once the scattered echo has been calculated, the bubble is treated as a point emitter radiating a spherical wave, for which the signal recorded by each transducer element, that is just given by the delay time and the geometrical attenuation, is evaluated analytically and used to create the received data according to eq. (1.8). The number of simulations averaged for each data-point was 250.

2.2.2 In-vivo

The in-vivo acquisitions were performed using a 128-Verasonics platform (Verasonics Inc., Kirkland, USA) using an ATL P4-1 (Philips, Seattle, USA) phased-array transducer. The Left Ventricular Chamber (LVC) of an healthy volunteer was imaged while a continuous infusion 1.2 ml/min of Sonovue was administered The protocol used was approved by the Imperial College Research Ethics Committee. The acquisitions were made by our group member Dr. Matthieu Toulemonde.

2.2.3 Motion Compensation

It will be seen in the next section that motion induces deformations of the point spread function, creating artefacts in the image. We have therefore applied a simple off-the-shelf motion compensation algorithm to demonstrate the viability of this kind of approach. The software, designed for MRI data, is available online at and based on [101]: it models the motion field using a B-spline grid and can therefore account for both rigid and non-rigid transformation. Further details about it and its accuracy can be found in Harput et al. [102], where it is shown that its precision is good enough to be used for super-resolution ultrasound imaging. In this work, non-rigid transformations are estimated between each PI beamformed radio frequency pre-compounding frames, with the central angle as reference, and used to register the images before compounding summation.

Note that the shift between the two inverted pulse of each PI sequence is not compensated: however, the aim of this chapter is to show the importance of correcting motion rather than to produce the best registration algorithm for CEUS sequences; this choice is also justified by the observation that compounding is the main responsible of the intensity loss, as visible in the next chapter.

2.2.4 Analysis

Regarding the simulations, we evaluate the maximum intensity I in a squared region of interest of 6mm $\times$ 6mm centred on the microbubble position: when the bubble is moving, the centre is considered as the average position during the whole motion. The region of interest is shown in green in Fig. 2.1. To get an estimate of the intensity variation, the value I is divided by I_0 which represent the peak intensity reconstructed when the same microbubble is imaged while not moving. We then take the average of such normalized intensities to create plots under various conditions. This gives an indication of the peak brightness of the received signal compared to a steady one. We repeat the same operations using the average intensities rather than the maximum, which is a measure more closely related to perfusion estimation. Note that in [103] we used the ratio of the average intensities rather than the average of the ratios; they highlight the same effect, but the one proposed here is possibly less sensitive to bright outliers, i.e. resonant bubbles.

For the human acquisitions, the compounded PI frames are further enhanced using a method called SUM7 [76], which basically consists in an incoherent sum of 7 frames, giving a final display frame rate of about 30 Hz: this is conceptually identical to a short time Power Doppler (PD) (see Sec. 1.2.4) except for the fact that the absolute value of the images is averaged rather than the *squared* absolute value.

To evaluate image quality, we used the Contrast to Noise Ratio (CNR) and the Contrast to Acoustic Noise Ratio (CANR) measures. The first one gives an indication of the intensity ratio between the LVC and two Region of Interest (ROI) located outside the image field of view, representing noise (see Fig. 2.6 for a definition of the ROIs):

$$\text{CNR} = \frac{\mu_{LV} - \mu_{ROI}}{\sqrt{\sigma_{LV} - \sigma_{ROI}}} \tag{2.1}$$

where μ_{LV} and μ_{ROI} are the mean intensities in the LV chamber and in each noise ROIs, while σ_{LV} and σ_{ROI} are their variances. This value is averaged over all frames. Since the LVC is filled by blood containing contrast agents, this measure is similar to signal to noise ratio where the acoustic energy radiated by microbubbles is taken as signal of interest. Note that the noise region is comprised of both random and interference noise, therefore this measures helps us understand whether the signal enhancement given by motion correction interferes with the compounding process, increasing side and grating lobe.

The second one measures the ratio between the LVC signal and 6 different segments of the myocardium: under the assumption that contrast noise is negligible, which can be fulfilled by manually choosing frames with little myocardial perfusion, the signal from the cardiac muscle is mainly due to clutter, therefore CANR also measures the ability of removing motion artefacts. The myocardial segments are drawn using an automated method able to track the cardiac walls during the US sequence [75]. The CANR definition is the same as the CNR, where the noise ROIs are switched with different segments of the myocardium (see Fig. 2.6).

2.3 Results

Simulations

The first characteristic effect of motion is the blurring and modification of the PSF, as shown in [17]. In Fig. 2.1, the average PSF for different velocities is shown. We see that the presence of motion mainly affects its shape when an axial motion is present, while a pure lateral motion creates only a modest elongation of the mainlobe and a slight increase in the strength and size of the first sidelobes. An axial motion or a diagonal motion, on the other hand, heavily change the shape of a point target and, even at relatively modest speeds of 25cm/s, generates the impression of two closely spaced points rather than a single peaked image; the presence of an axial motion also heavily affects the strength of sidelobes, confirming for microbubbles the findings of [17] which were made for linear scatterers.

In Fig. 2.2, we show the maximum and average signal intensity in a ROI centred at the bubble position. As expected, due to the low pass nature of the PSF in the

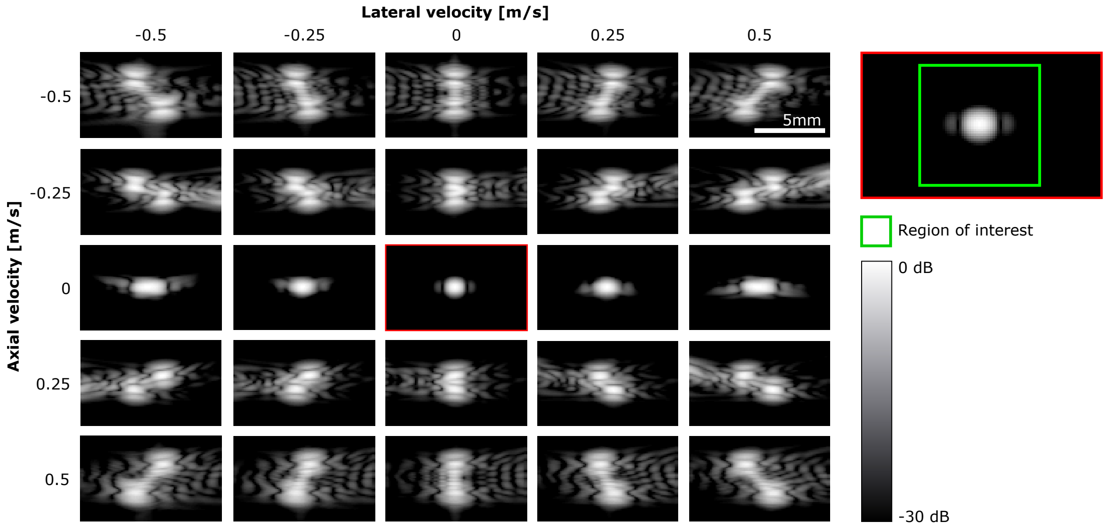

Figure 2.1: Simulated microbubble point spread function variation for different velocities, each of them results from the average of 250 simulations. The green square highlights the region of interest used for intensity estimation.

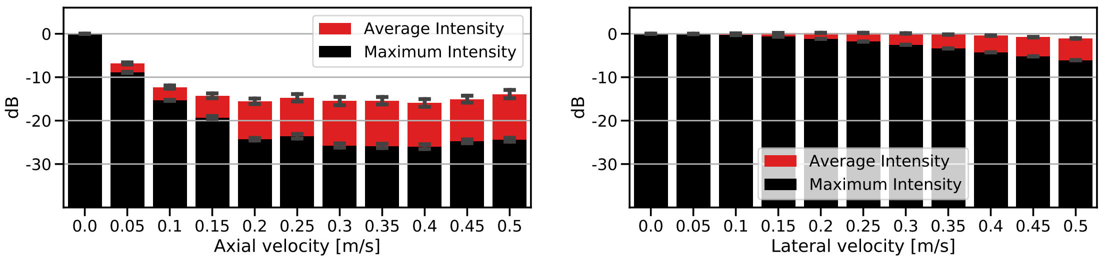

(a) Axial motion

(b) Lateral motion

Figure 2.2: Intensity variation for different lateral and axial motions of the microbubble. Each point is given by the ratio between intensity of a moving microbubble and the intensity of the same steady microbubble, averaged over 250 simulations.

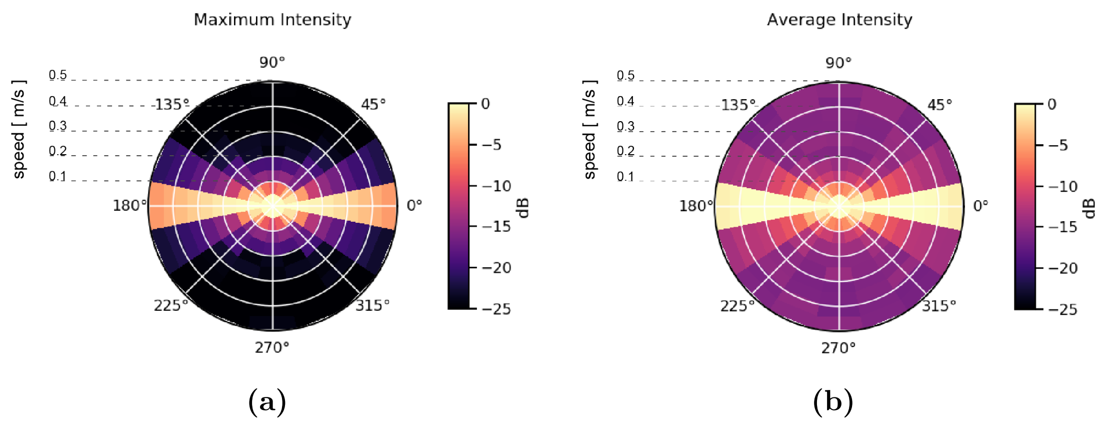

Figure 2.3: Intensity variation for motions of different magnitude and direction, up to 50cm/s.

lateral dimension, once more motion affects the signal intensity mainly for vertical velocities, resulting in a negligible average intensity loss for lateral speeds up to 50cm/s, with a drop of -7dB for the maximum intensity. On the other hand, the maximum intensity experiences a reduction of -9dB already for axial speeds of 5cm/s and has the lowest drop around 35cm/s where the maximum intensity reaches -26dB compared to the steady case. The average intensity, on the other hand, is less affected and is reduced by -16dB at most when the microbubble has an axial speed of 40cm/s.

To give a clearer description of how motion affects the signal intensity, the polar plots in Fig. 2.3 show the same information as Fig. 2.2 for different velocity magnitudes and directions. They show that, for both maximum and average intensity, the rapid signal attenuation happens already when the velocity direction moves a few degrees away from the lateral axis, and is more rapid the more its direction is vertical.

The images in Fig. 2.4 estimate how much the bubble position affects the change of intensity. While Fig .2.4(b) indicate that an axial velocity has an effect that is practically independent of the microbubble position, the images in Fig .2.4(a) clearly indicate that a lateral motion becomes rapidly more significant the more its angular position moves away from the 0 degree axis, and becomes as significant as an axial motion for 30° or more.

The last simulation result, that is the barplot in Fig. 2.5, describe how much the compounding stage is responsible for the loss of intensity. while for a single angle the intensity is practically kept the same as for a steady bubble, already using 6 angles gives a reduction of -18dB of maximum intensity, clearly showing that the main responsible of signal loss is the compounding stage rather than the phase shift

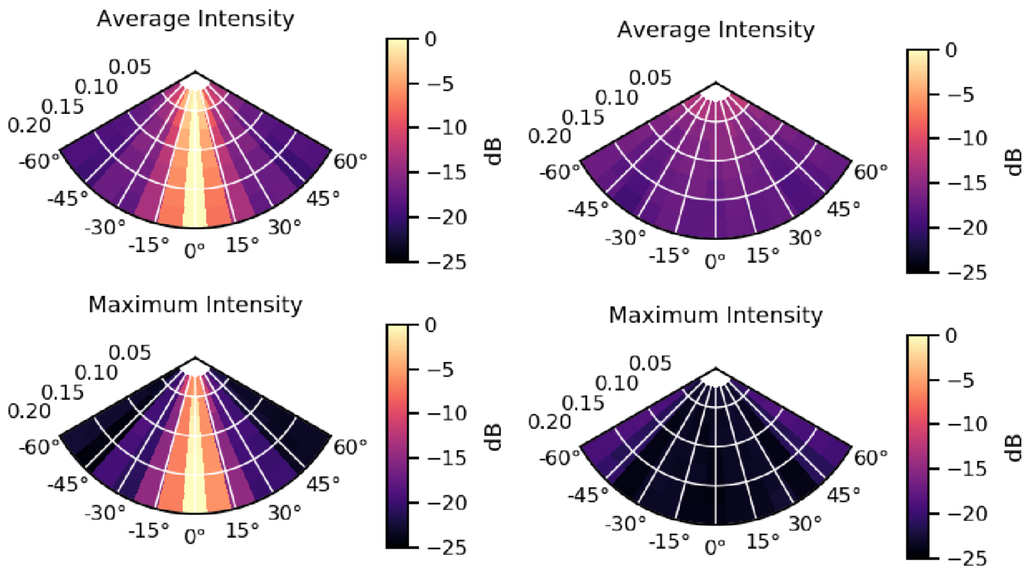

(a) Bubble moving laterally

(b) Bubble moving axially

Figure 2.4: Intensity variation for a microbubble moving at 25cm/s located at different position of the scanned image. The plots in the left column refer to a microbubble moving in the lateral direction while in the right column the microbubble is moving axially. Depths values are in meters.

between consecutive PI transmissions.

In-vivo

The human acquisition on healthy volunteer is shown in Fig. 2.6. The PI frames in Fig. 2.6(a) show the effect of motion, which is visible in the left image as a dark stripe and in the central image as a more homogeneous dark region having an intensity drop up to 10.4dB, despite the noise variance reduction produced by the SUM7 method.

The rightmost image is the result of applying the proposed motion compensation algorithm. The benefits of correction for motion are readily visible, since the dark area is clearly removed together with many artefacts, as shown for example by the greater visibility of anatomical structures such as the myocardial boundaries or the papillary muscle in the centre of the LVC.

Quantification for the in-vivo results is shown in Fig. 2.6, showing that the CNR is improved from 2dB to 3.2dB for the standard PI images and doubled for SUM7 processed frames. The CANR is also greatly improved, with a 0.5dB increase for standard images and rising from an average of 0.6db to 1.5dB for the SUM7 case.

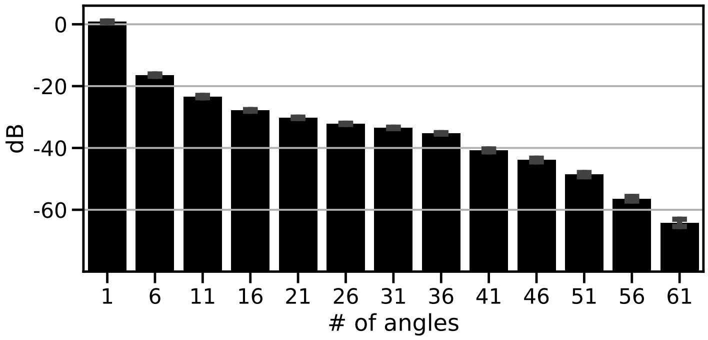

Figure 2.5: Effect of different number of compounding angles on the maximum intensity

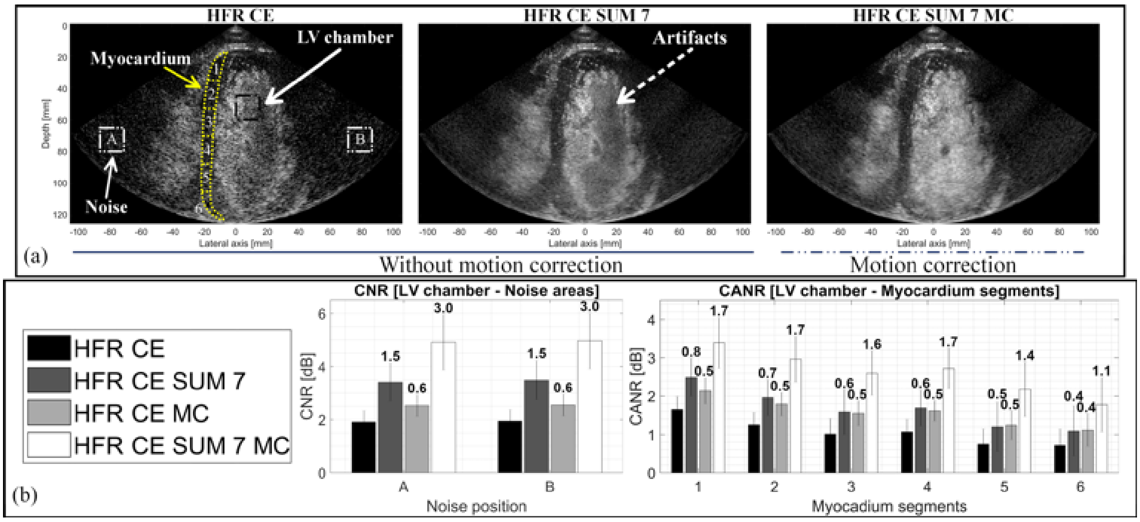

Figure 2.6: In vivo acquisitions on a healthy volunteer

2.4 Discussion and conclusions

Motion and its image degradation effects have been investigated separately for coherent compounding [17] and contrast multipulse imaging [89]. This chapter has, instead, shown the effect of microbubble motion on the intensity and quantification of HFR Contrast Echocardiography (CE) images when both PI and compounding is used, and highlighted the need of motion compensation for them. The work in [17], showing how motion degrades the main lobe signals while increasing the sidelobes, demonstrates the high variability of the PSF for different motions under different sequences of compounding angles and, furthermore, the non-linearity of the microbubble response greatly complicates a theoretical analysis such as the one performed by Alberti et al. [10]. We had, then, to rely on simulations to study the impact of motion. Using a custom simulator based on Field II [1], we showed that even moderate motion can significantly affect the intensity of PI images made with diverging waves, especially when the velocity is not directed laterally. The same has been found for the shape of the PSF. We remark, however, that the large sensitivity to axial motion compared to lateral motions is also the result of the relatively small aperture that has been used in this study: other works, like the one of Gammelmark [93], have shown that the impact of lateral motion can be almost as important as the axial one for low F numbers, i.e. for large apertures and shallow depths.

In [91], Viti and colleagues have evaluated how out of plane flow impact contrast detection, when amplitude modulation is used to image the cross section of a flow phantom. If we compare their findings with ours, we see that at least 30 compounded angles are required to achieve a reduction of -3dB when out of plane flow is imaged, while in our case 11 angles already suffice to give a reduction of -14dB of the average intensity, showing that in-plane motion has a greater detrimental effect on contrast imaging that out of plane one.

We have also shown *in-vivo* that the use of motion correction is a valuable method for compensating such effects, giving significant CNR and CANR improvements. We remark, however, that the motion compensation technique used is not optimized for US diverging wave imaging and has only been applied to demonstrate the usefulness of registration methods in this context. Also, the computation time for motion estimation and registration of each compounded frame is about 71s $\pm$10s (Intel Core i7-5820K, 4.50 GHz.), suggesting that non-rigid methods have to be computationally simplified to achieve real time motion correction.

The finding in this chapter confirm that, as already introduced in Sec. 1.2.4, the fact that standard plane wave compounding extracts the average value of the Doppler signal calls for methods that are insensitive to motion when multiple frames are used. While one viable method is given by motion compensation, its use is computationally demanding. In the next chapters, we will propose several techniques based on signal processing to improve HFR CEUS when flow has to be imaged.

Chapter 3

Acoustic sub-aperture processing

The combined use of contrast agents and HFR US gives some unique opportunities for designing simple yet effective signal processing methods by exploiting the statistical properties of acquired signals, thanks to the large amount of data samples generated by fast acquisitions, typically around 1 Gb and up to 20.000 frames per second. However, the reduced echoes strength given by the weaker amplitude of unfocused waves compared to focused ones, causes a drop in Signal to Noise Ratio (SNR) which is often addressed by compounding (Sec. 1.2.4) of differently steered transmissions. However, as the previous chapter highlights, this approach has to be limited to a small numnber of frames in the presence of fast moving targets, such as microbubbles or red blood cells, as the inherent low-pass filtering behaviour of compounding can cause a degradation of the desired signal.

Moreover, despite the stronger echoes produced by microbubbles compared to natural blood scatterers, this increase has a frequency dependency [104]: such that, at higher clinical frequencies, the signal generated by commercially available contrast agents still gives low SNR at depths. This challenge is clearly even harder when no contrast agent is used.

The joined use of HFR imaging and contrast agents opens up opportunities for imaging fast scatters, such as in cardiac and arterial flow studies, but also to use statistical methods to generate images of greater quality by leveraging information from multiple frames directly in the reconstruction process. Examples of this use are the reconstruction of 2D vector velocity using cross correlation of speckle patches for large vessels imaging [87], allowed by the reduced speckle decorrelation given by the high PRF. Such inter-frame speckle persistance has been exploited in [105] to adaptively clutter filter the images, obtaining slow flows usually rejected by wall filters. Lastly, the large density of frames per acquisition time has been shown to give opportunity to use the spatiotemporal variance estimation of an entire video sequence for clutter-flow signal separation, using Singular Value Decomposition (SVD) filtering on B-mode and contrast images [72, 106].

Despite the large pool of processing possibilities offered by HFR US, an important aspect that affects the adoption of a new technique in the clinical routine is given by the computational requirements: since the data acquired during an unfocused acquisition is very large, approaching often Gygabyte per second, the algorithms must hopefully be simple, fast and parallelizable.

In recent years, many methods to improve image quality, without introducing significant computational challenges, have been developed by exploiting the concept of coherence. In Coherent Flow Power Doppler (CFPD) [107], the use of spatial correlation between different transducer elements has been exploited to estimate the PD signal. This is done by building on the work of Lediju et al. [56], which defined the Short Lag Spatial Coherence (SLSC) imaging, but despite its promising results it is formulated in a computational demanding way and suffers from axial blurring due to the way cross correlation is estimated. As briefly discussed in Sec. 1.2.4, in [41], the lagged Doppler autocorrelation of pixel estimates has been used to reduce the effect of noise on Power Doppler images. This method has, however, limitations that are given by the spurious correlations generated by compounding different steered angle, which forces to compound before estimating the lagged autocovariance, therefore generating a tradeoff between the number of compounded transmissions and the smallest measurable autocorrelation lag.

Another technique using autocorrelation is given by Shin and collegeus [108, 109], where the reduction of interference noise has been achieved by cros correlating the same image beamformed two times using different apodizations, similarly to what has been done in SLSC, and the resulting cross correlation measure has been used as a weights for the B-mode image intensity. While describing their method, named Dual Apodization with Cross-correlation (DAX), the authors also showed using k-space arguments why the grating lobes of PSF made with alternating apodizations have an opposite phase [53]. We will use this result and, in the next chapter, extend it to general orthogonal apodization pairs.

3.1 Principles of ASAP

In vascular imaging, we want to differenciate signals coming from tissue and signals coming from blood, therefore the assumption that tissue motion is much lower than blood flow is often employed. This means that is possible to high-pass filter (wall filtering) the Doppler signal to keep only the signal from microbubbles. Denoting with f the frame number, applying the wall filter with impulse response $h(f)$ to all the channels x_i creates the new channel vector of filtered samples

$$\hat{\mathbf{x}}(f) = \begin{pmatrix} \hat{x}_1(f) \\ \hat{x}_2(f) \\ \hat{x}_3(f) \\ \vdots \end{pmatrix} = \begin{pmatrix} \hat{h}(f) * x_1(f) \\ \hat{h}(f) * x_2(f) \\ \hat{h}(f) * x_3(f) \\ \vdots \end{pmatrix}. \tag{3.1}$$

This gives a cross correlation matrix

$$\mathbf{R}_s = \frac{1}{F} \sum_f \hat{\mathbf{x}}(f) \hat{\mathbf{x}}^{\mathsf{H}}(f), \tag{3.2}$$

where F is the number of frames averaged. Because of the filtering, clutter signals are ideally not contributing to this matrix. The PD value is then estimated as shown in eq. (1.50), so that that for each pixel location the estimate of PD is given by

$$PD = \mathbf{a}^{\mathsf{H}} \mathbf{R}_s \mathbf{a}, \tag{3.3}$$

where $\mathbf{a}$ is the apodization.

Note that, while the above gives a clear picture of what happens during the reconstruction of a PD frame, because the order in which filtering and Delay and Sum (DAS) estimation is done is not important, one usually first creates the pixel signal estimate

$$p(f) = \mathbf{a}^{\mathsf{H}} \mathbf{x}, \tag{3.4}$$

then filters this estimates using $h(f)$ and at the end evaluates the signal power. In both cases, the final power estimate will be given by eq. (3.3).

Lets now assume that the recorded signal are corrupted by noise of constant power σ_n across channels, which is uncorrelated both between different pairs of channels and with the echoes. Then, in the limit of a large number of frames, the cross correlation matrix will have the form

$$\mathbf{R} = \mathbf{R}_s + \sigma_n \mathbf{I}, \tag{3.5}$$

where $\mathbf{I}$ is the identity matrix. The PD estimate is then given by

$$PD = \mathbf{a}^{\mathsf{H}} (\mathbf{R}_s + \sigma_n \mathbf{I}) \mathbf{a} = \mathbf{a}^{\mathsf{H}} \mathbf{R}_s \mathbf{a} + \mathbf{a}^{\mathsf{H}} (\sigma_n \mathbf{I}) \mathbf{a} = \mathbf{a}^{\mathsf{H}} \mathbf{R}_s \mathbf{a} + \sigma_n, \tag{3.6}$$

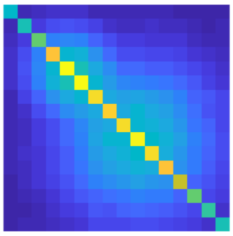

(a) Noisy cross correlation matrix.

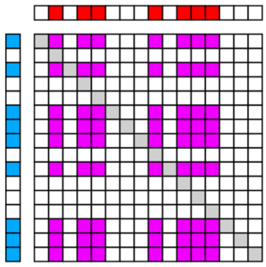

(b) Cross correlation matrix weightings generated by the two apertures.

Figure 3.1: Illustrative example of a noisy cross correlation matrix and the weightings generated by the two ASAP apertures.

where we assumed that $\|\mathbf{a}\| = 1$. Clearly, the presence of noise will bias the PD estimated as its power will be added to the final value.

3.1.1 Noise attenuation

The goal of Acoustic Sub-Aperture Processing is to remove noise contribution to the final PD estimate while preserving the power of the signal of interest. To do so, the core idea is to split the channels into two non overlapping apertures $\mathbf{w}_1$ and $\mathbf{w}_2$, beamform two video sequences from them and calculate, for each pixel location, the Doppler cross-correlation between the two estimates. The power estimate is then

$$
\begin{aligned}
ASAP &= \frac{1}{F}\sum_f p_1(f)p_2(f) \\
&= \frac{1}{F}\sum_f \mathbf{w}_1^{\mathsf{H}}\mathbf{x}\mathbf{x}^{\mathsf{H}}\mathbf{w}_2 \\
&\approx \mathbf{w}_1^{\mathsf{H}}(\mathbf{R}_s + \sigma_n\mathbf{I})\mathbf{w}_2 \\
&= \mathbf{w}_1^{\mathsf{H}}\mathbf{R}_s\mathbf{w}_2 + \sigma_n\mathbf{w}_1^{\mathsf{H}}\mathbf{w}_2 \\
&= \mathbf{w}_1^{\mathsf{H}}\mathbf{R}_s\mathbf{w}_2,
\end{aligned} \tag{3.7}
$$

showing that noise is asymptotically removed from the power estimate as more frames are considered. If a limited number of frames is considered, then under the assumption of Gaussian noise the SNR will on average improve by a factor proportional to $\sqrt{F}$. An illustrative example of noisy cross correlation matrix and weightings produced by the two apertures is shown in Fig. 3.1: it is possible to appreciate how the non-overlapping condition translates in a zero-weighting of the diagonal elements, which is where most of the noise power is concentrated.

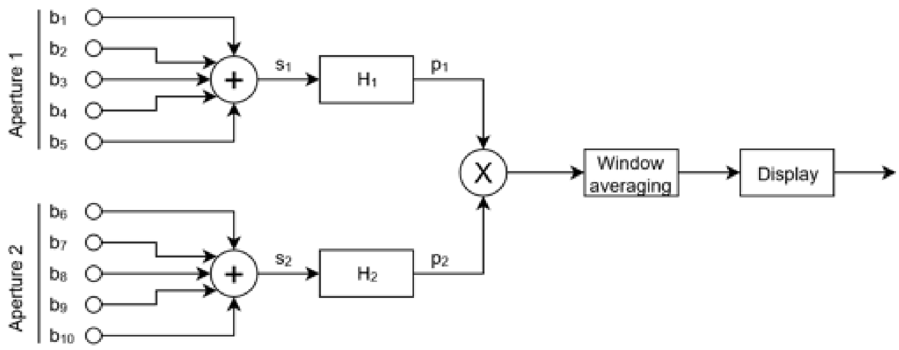

Figure 3.2: Schematic of the ASAP method. For each pixel, data coming from different channels b_i is split in two apertures and beamformed, to generate the signals s_i. Such signals are then filtered individually by filters H_i, and then multiplied and averaged to perform cross correlation. The result is then processed to remove unwanted signal, such as sidelobes, log compressed and displayed.

A key characteristic of this approach is that the computation of the cross correlation matrix is not necessary, but only the cross correlation of two video sequences beamformed using half the number of channels is required. This keeps the computational complexity of ASAP equal to the one of PD.

3.1.2 Cross correlation sign and display

Despite the cross correlation matrix $\mathbf{R}$ being positive semidefinite, the fact that we are using two different apertures leads to a generic complex scalar result, including negative cross correlations. While one could in principle just show the cross correlation magnitude, we expect to have a positive cross correlation when the signal of interest is imaged. Backed by the work of [53], we use the fact that negative correlations are given by the presence of intereference signals, therefore we only show the real part of the ASAP result and set any negative correlation to zero. A diagram of the ASAP method is shown in Fig. 3.2.

3.1.3 Wall filtering

We have precedently described the result of ASAP applied on the beamformed signals which have been filtered by the same wall filter for both apertures. To better understand how wall filtering affects the final estimate, we assume that noise is negligible and only care about the spectrum of the echo signal. If we call $P_i(\omega)$ the Fourier spectrum of the Doppler signal estimated by the i-th aperture, the cross-correlation theorem tells us that

$$\begin{aligned} ASAP &= \sum_f p_1(f)p_2(f) \\ &= \int_{-\omega_n}^{\omega_N} P_1(\omega)P_2^*(\omega)d\omega \\ &= \int_{-\omega_n}^{\omega_N} \|S(\omega)\|^2 H_1(\omega)H_2^*(\omega)d\omega, \end{aligned} \tag{3.8}$$

where ω_N is the Nyquist frequency, $S(\omega)$ is the Fourier transform of the echo Doppler signal and $H_i(\omega)$ is the Fourier transform of the wall filter applied on the i-th aperture.

The previous result shows that the total filter applied *to the power spectrum* is given by the product of the two applied filters. This means that, for example, by applying a high pass filter on one aperture and a low pass filter on the other, we can effectively obtain a bandpass filter. However, because there's no absolute value operation performed on the filters, care must be taken at the phase resulting from the product of the two filters.

If the same filter is applied on both apertures, then the previous equation siplifies to

$$ASAP = \int_{-\omega_n}^{\omega_N} \|S(\omega)\|^2 \|H(\omega)\|^2 d\omega, \tag{3.9}$$

while if the filters have arbitrary phase, the equation can be expressed as

$$ASAP = \int_{-\omega_n}^{\omega_N} \|S(\omega)\|^2 \|H_1(\omega)H_1^*(\omega)\| e^{j\theta(\omega)} d\omega, \tag{3.10}$$

where $\theta(\omega)$ is the sum of the two filter phases.

Rather than being a limitation, the control over the phase gives the possibility of perform different kind of estimations rather than simple PD. However, wether it is better to design a single global filter or two different sub-aperture filters depends on the application. We give an example of this by extracting the flow direction from the ASAP signal. We use two simple filters on each aperture: a low pass filter with impulse response $h_1 = (1, 1)^\intercal$ and an high pass filter $h_2 = (1, -1)^\intercal$. The zero in $\omega = 0$ of the high pass filter creates a jump of π its phase between positive and negative frequencies, so that the two sides of the frequency axis (within the Nyquist support) have opposite sign. This reduces the ASAP value to

$$ASAP = -\int_{-\omega_n}^{0} \|S(\omega)\|^2 \|H_1(\omega)H_1^*(\omega)\| d\omega + \int_{0}^{\omega_N} \|S(\omega)\|^2 \|H_1(\omega)H_1^*(\omega)\| d\omega, \tag{3.11}$$

which will have a negative sign if the Doppler spectrum is mostly concentrated in the negative frequencies region and, conversely, a positive sign if the spectrum is mostly in the positive frequencies. Therefore, simply looking at the sign of the cross correlation of the two apertures we can infer the direction of flow.

3.2 Methods

3.2.1 In-vitro evaluation

To evaluate noise suppression, the cross-section of a 200μm tube containing flowing microbubbles was imaged using Pulse Inversion and processed using both ASAP and PD The tube was located roughly 1.5cm below the transducer center. A suspension of 0.1mL of contrast agent (SonoVue, Bracco Imaging SpA, Milan, Italy) per liter of water was driven through the tube at a mean speed of 20cm/s by a syringe pump. The ultrasonic acquisition was performed using 4MHz single-cycle pulses at 0.2 MI from a L12-3v linear array probe and Vantage 128 ultrasound platform (Verasonics, Kirkland, WA, USA). The experiment used only the central 128 elements of the probe, for a total aperture width of roughly 2.5cm. Seven compounded plane-waves, equally spaced between -20 and +20 degrees, gave a final frame-rate of 875 Hz. The acquired RF data were filtered in fast-time (depth) using a 5th order Butterworth bandpass filter with cutoff frequencies at 6MHz and 12MHz. A total of 10 acquisitions has been done and the results averaged.

3.2.2 In-vivo experiments

The kidney of a healthy rabbit was imaged to assess its vasculature. All procedures complied with the Animals (Scientific Procedures) Act 1986 and were approved by the Local Ethical Review Process Committee of Imperial College London (Home Office Licence PPL 70/7333). The male New Zealand White rabbit (6 months old; HSDIF strain, Specific Pathogen Free, Harlan UK) was anaesthetized with medetomidine (0.25 mL/kg) and ketamine (0.15 mL/kg) while body temperature was maintained at 37C by a warming plate. A pulse oximeter (Edan VE-H100B) was attached to the tail to monitor oxygen saturation and heart rate. The fur around the scanning site was shaved to acquire images of the rabbit's right renal vasculature. SonoVue microbubbles were injected via the marginal ear vein as a bolus of 0.25 mL. The ultrasound acquisition was the same as the in-vitro experiment, except that each frame was reconstructed from 15 compounded angles between -18 and 18 degrees, with a final frame-rate of 750Hz. The data were transferred to a PC for offline processing using Matlab (The MathWorks, Natick, MA, USA).

3.2.3 Image quality quantification

We have used two metrics to evaluate the quality of ASAP images. The first one is the SNR, which is given by

$$SNR = \frac{\mathsf{E}[I_s]}{\mathsf{E}[I_n]}, \tag{3.12}$$

gives an estimate of the strength of the signal of interest compared to noise, where $\mathsf{E}[I_s]$ is the average intensity in the signal ROI and $\mathsf{E}[I_n]$ is the average intensity in the noise ROI. Sample averages are taken over different frames. Similarly, the CNR given by

$$CNR = \frac{\|\mu_s - \mu_n\|}{\sqrt{\sigma_s^2 + \sigma_n^2}}, \tag{3.13}$$

where $\mu_i = \mathsf{E}[I_i]$, σ_n^2 is the intensity variance in the noise ROI and σ_s^2 is the intensity variance in the signal ROI.

3.3 Results

3.3.1 Noise rejection

Fig. 3.3 shows the ability of ASAP to substantially reduce the noise floor while maintaining image axial resolution. Since we are performing a correlation estimation, noise suppression will improve with the number of averaged frames. This is fundamentally different from what happens using PD, which is not able to distinguish between noise and Doppler signal power.

The ability of ASAP to improve SNR as more frames are acquired is depicted in Fig. 3.4a, where the SNR is plotted against number of frames. As expected, the noise floor in PD remained approximately constant at 21dB, even for an ensemble averaging of over 200 frames. On the other hand, processing with ASAP shows an

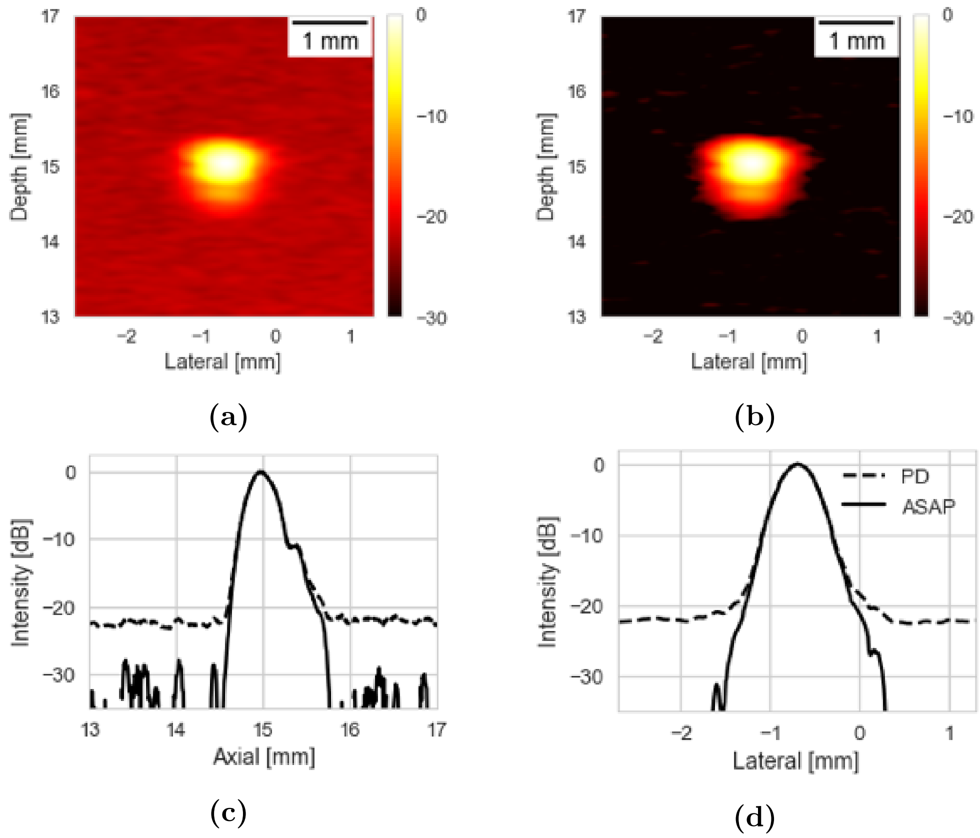

Figure 3.3: In vitro results,showing the cross-section of a 200 micron diameter vessel with flowing microbubbles using Pulse Inversion Power Doppler (a) and ASAP (b) processing. Both images were made using 200 frames acquired over 0.22s. (c) and (d) show the axial and lateral plot, respectively, for the same acquisition.

SNR improvement of 10dB compared to PD with 250frames used, with an improvement proportional to the square root of the number of averaged frames, as predicted by the theory. The final SNR reaches a value of 31dB. The same behaviour was observed for in-vivo experiments: Fig. 3.4b shows that an increase of 10dB in SNR was achieved by ASAP over PD. The CNR of ASAP, on the other hand, is similar to PD and its evolution with the number of frames exactly overlaps the PD one, as visible in Fig. 3.4c.

3.3.2 Choice of sub-apertures

The way channels are divided into two different groups affects the shape of the PSF given by each one of the two sub-apertures. This in turn changes the correlation of the interference signals, which are represented as side and grating lobes.

To evaluate this effect, we studied the PSF after processing the in-vitro data with ASAP using different sub-apertures. Apertures were chosen to have no overlapping

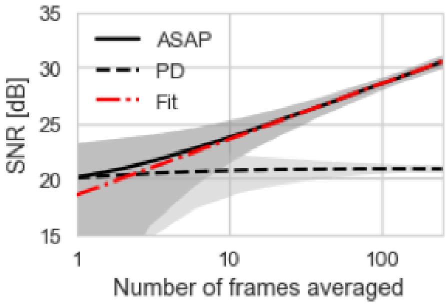

(a) SNR in-vitro.

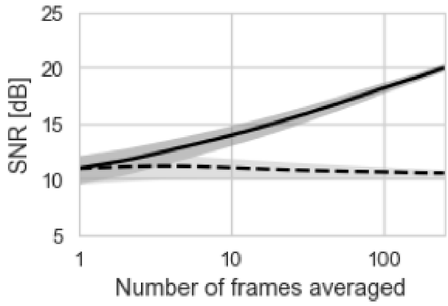

(b) SNR in-vivo.

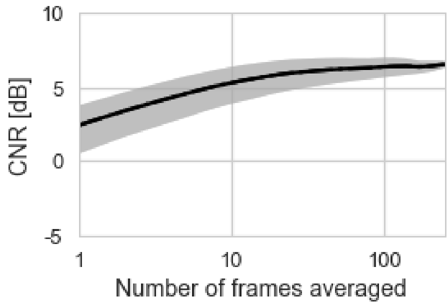

(c) CNR in-vitro

Figure 3.4: Evolution of SNR as a function of the number of frames averaged, for in-vitro (a) and in vivo (b) experiments. The red line shows a square root fit. The plot in (c) shows the CNR evolution: the PD and ASAP lines are exactly overlapping. Axis are in logarithmic scale.

elements to ensure noise decorrelation. In [52] it is shown that grouping the channels in two non overlapping apertures results in positively correlated mainlobe signals and negatively correlated interference lobes: with this in mind, negative correlating interference lobes can be detected and removed by setting the corresponding pixels to zero.

The channels were split into two groups A_1 and A_2 of roughly equal size, with no overlapping elements. If such splitting was not done randomly, we use the number N to indicate the number of contiguous channels used in each aperture: for example, saying $N = 3$ means that channels 1,2 and 3 belong to A_1, channels 4,5 and 6 to A_2, then channels 7,8 and 9 to A_1 again, and so on. We investigated apertures with N equal to 1, 2, 4 and 8. We also randomly split the channels into two apertures. The results of ASAP processing for different apertures are shown in Fig. 3.5.

The first row of the image was obtained by taking the absolute value of the correlation without removing negative correlations. This creates artefacts in terms of grating- and side-lobes. The image shows how increasing N moves the interference lobes closer to the mainlobe. In the second row, negative correlations were set to zero, and it can readily be seen that all interference signals have been suppressed.

	Without interference suppression	With interference suppression
N=1	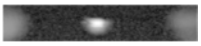	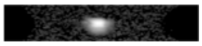
N=2	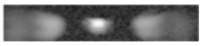	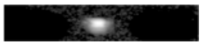
N=4	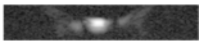	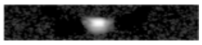
N=8	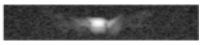	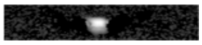
Random	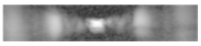	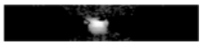

Figure 3.5: Estimation of the point spread function obtained when using ASAP, by means of a tube with flowing microbubbles, imaged in cross section. The first column shows the result of ASAP when interference is not suppressed, for different apertures. The second column shows the effect of suppressing interference signals, by setting negative correlations to zero. The dynamic range of the images is 40dB, 1000 frames are averaged.

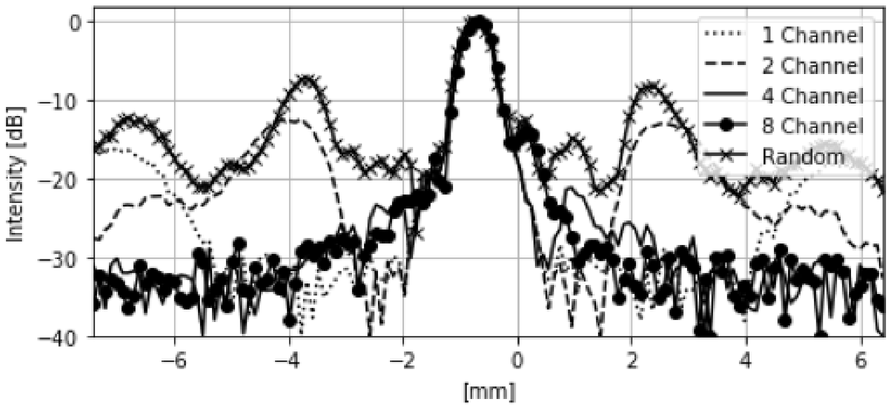

Figure 3.6: Lateral plot of the PSF when different apertures are used, without interference suppression, showing the position and strength of the side and grating lobes.

This confirms the expected negative correlation between side and grating lobes of the two apertures. The last column highlights how, somehow counter-intuitively, using random apertures performs poorly in terms of interference intensity.

Fig. 3.6 shows the lateral plots for the images in Fig. 3.5. It can be seen that the apertures for N = 4 and 8 give weaker sidelobes. This is the preferred condition, as the negative correlation of strong interference signals can mask the signal coming from weaker scatters, even if noise has been sufficiently suppressed.

On the other hand, taking too large an N may affect the results in the immediate near-field of the transducer. That is because the signal of a near field scatter has strong intensity in only a few adjacent channels, which can end up all in the same sub-aperture, reducing the cross-correlation between the sub-apertures. For this reason, we use N = 4 for in-vivo imaging.

3.3.3 Vascular imaging

To demonstrate the technique in vivo, the kidney of a healthy rabbit was scanned. In the resulting Pulse Inversion image (Fig. 3.7a), some of the non-contrast structures were still visible due to non-linear propagation artefacts [110]. It is also difficult to understand the vascular morphology because of speckle noise. The latter effect was mitigated by averaging several frames incoherently, after envelope extraction, to smooth the speckle noise for moving targets (Fig. 3.7b). Although this may help in delineating the main vascular structure, in practice it was necessary to use a wall filter and perform PD imaging (Fig. 3.7c). (Note that in our experiments the wall filter is always used after PI summation, for both PD and ASAP.)

Despite improvements in the image quality, the noise floor was high and comparable to the weak signals coming from some of the smaller vessels, especially in the deep regions of the image. As the noise power often changes with depth (because of depth varying signal amplification upon reception, also known as TGC), it is hard to separate noise from the fainter vessels by varying the dynamic range. This is especially true in real-time imaging, when the variance of PD is high due to the small number of frames used in the estimation. Using our technique, which generated the image shown in Fig. 3.7d, the noise level is largely reduced and the vasculature contrast is enhanced, especially in the challenging parts of the image. The rapid improvement in SNR with number of frames also makes possible the quantification of flow dynamics: we give an example, with the signal power in the cortex region, in Fig. 3.8. The resulting image enhancement makes the technique suitable for producing high-contrast images of the vasculature in real time

3.3.4 Separation of macro- and micro-flow using Wall filter

As mentioned, HFR US acquires thousands of frames per second, generating gigabytes of data; a processing technique that is computationally demanding therefore reduces the feasibility of real-time implementation. ASAP can be fully parallelized in a pixel-wise manner, without increasing the computational workload compared to the classical Power Doppler estimation. To further reduce complexity, we propose the use of a simple 2 tap Finite Impulse Response (FIR) filter, which is the backward finite difference: that is, we simply subtract consecutive frames. Although a filter with such a short impulse response has a poor transition at the cut-off frequency, the use of high frame rate imaging makes slow-moving signals very close to the zero-frequency, allowing simpler filters to be used. It must be noted that the use of

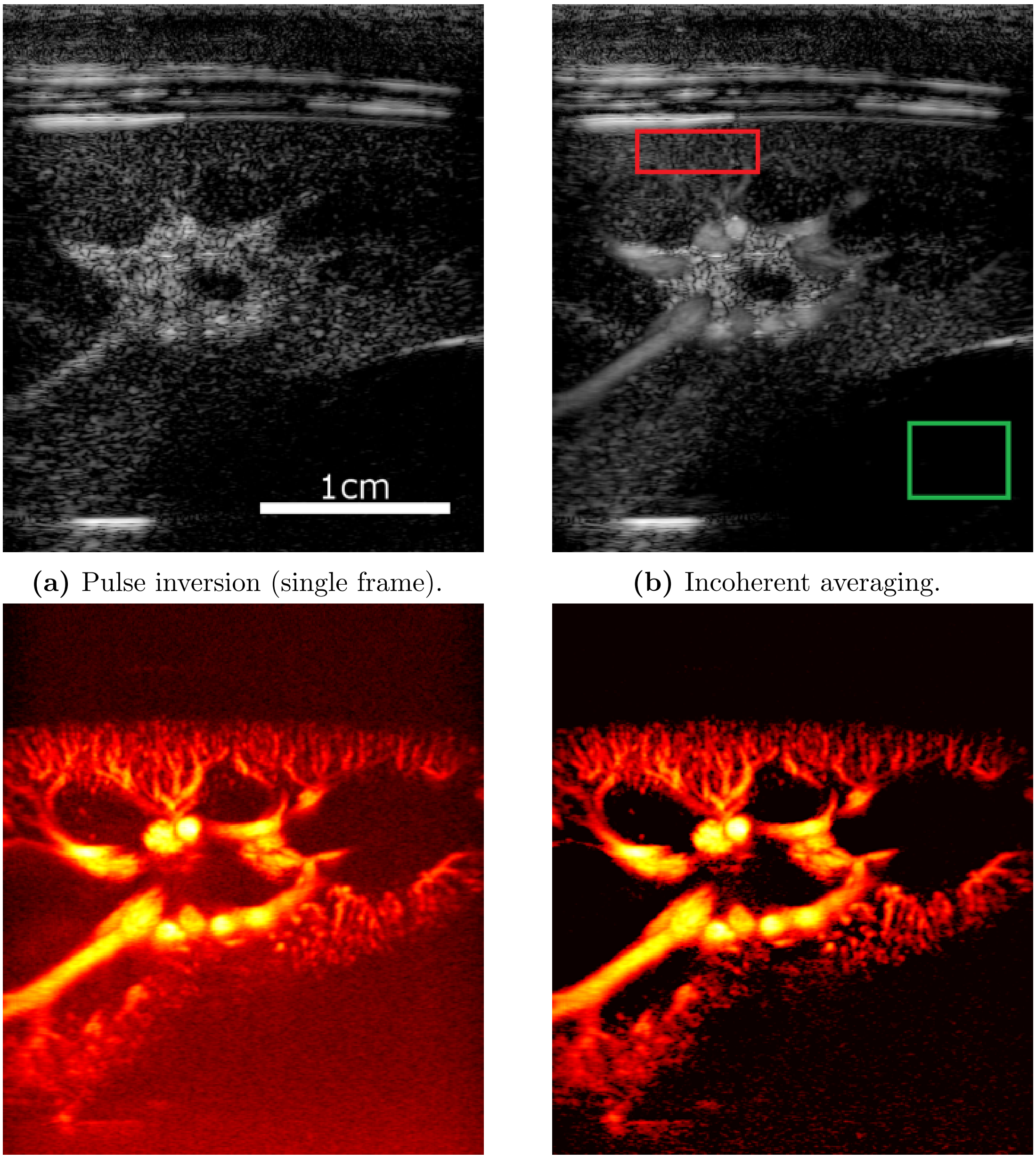

(a) Pulse inversion (single frame). **(b)** Incoherent averaging.

(c) Power Doppler. **(d)** ASAP.

Figure 3.7: In-vivo acquisition of a rabbit kidney after bolus injection of microbubbles: Pulse Inversion (a) and incoherent averaging (b), Power Doppler (c) and ASAP processing (d), displayed at 40dB of dynamic range. Averaging is done over 0.05sec, giving an imaging frame rate of 20Hz, for images (b), (c) and (d). The image in (b) also shows the region used for signal (red □) and noise (green □) measurement in SNR estimation.

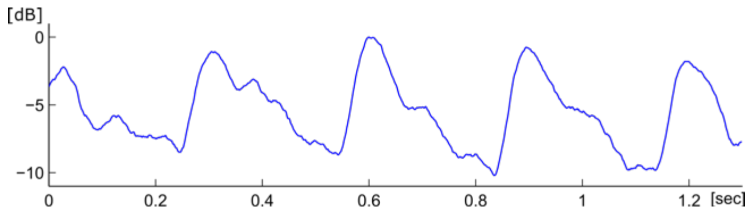

Figure 3.8: Quantification flow dynamics in the upper cortical region

such filters is not fundamental to the ASAP technique. The direct difference of two consecutive frames has already been evaluated for the transverse oscillation method and proved promising even for fast flow evaluation [111].

We extend such filter by varying the temporal distance between the two frames being subtracted. This changes the lowest cut-off frequency of the filter, highlighting vessels with different flow speed. An example is shown in Fig. 3.9a and Fig. 3.9b. It can clearly be seen that increasing the lag between the two subtracted frames allows more micro-vessels to be seen, especially ones in which microbubbles flow from the kidney cortex to the pyramid. We can therefore effectively lower our cut-off frequency, i.e. evaluate different flow regimes, while maintaining the same computational load. Another possibility is to use different filters for each one of the signals being correlated. Following the example given at the end of Sec. 3.1.3, we used two filters to obtain information on flow direction from the correlation value. This is illustrated in Fig. 3.9c, where flow towards the transducer is shown in red and flow moving away from the transducer is in blue.

3.4 Discussion

In this chapter, we propose an ultrasound imaging method, Acoustic Sub-Aperture Processing, capable of generating very high contrast images (with up to 10dB improvement over existing Doppler techniques both in-vitro and in-vivo) of macro- and micro-vessels in vivo at multi-centimetre depth, taking advantage of high frame-rate ultrasound and microbubble contrast agents.

The results show that CNR measures for ASAP is similar to PD. Actually they overlaps as showing in Fig. 4(c). This is due to that CNR measures take into account variance in the regions of interest, and for both PD and ASAP the local variance decreases with number of frames used. However it should be noted that such measure in a local region does not account for the global variations of the noise in the ultrasound images, which is known to change over imaging depth, as can be seen in Fig. 3.7c. PD can only reduce local noise variations through local averaging

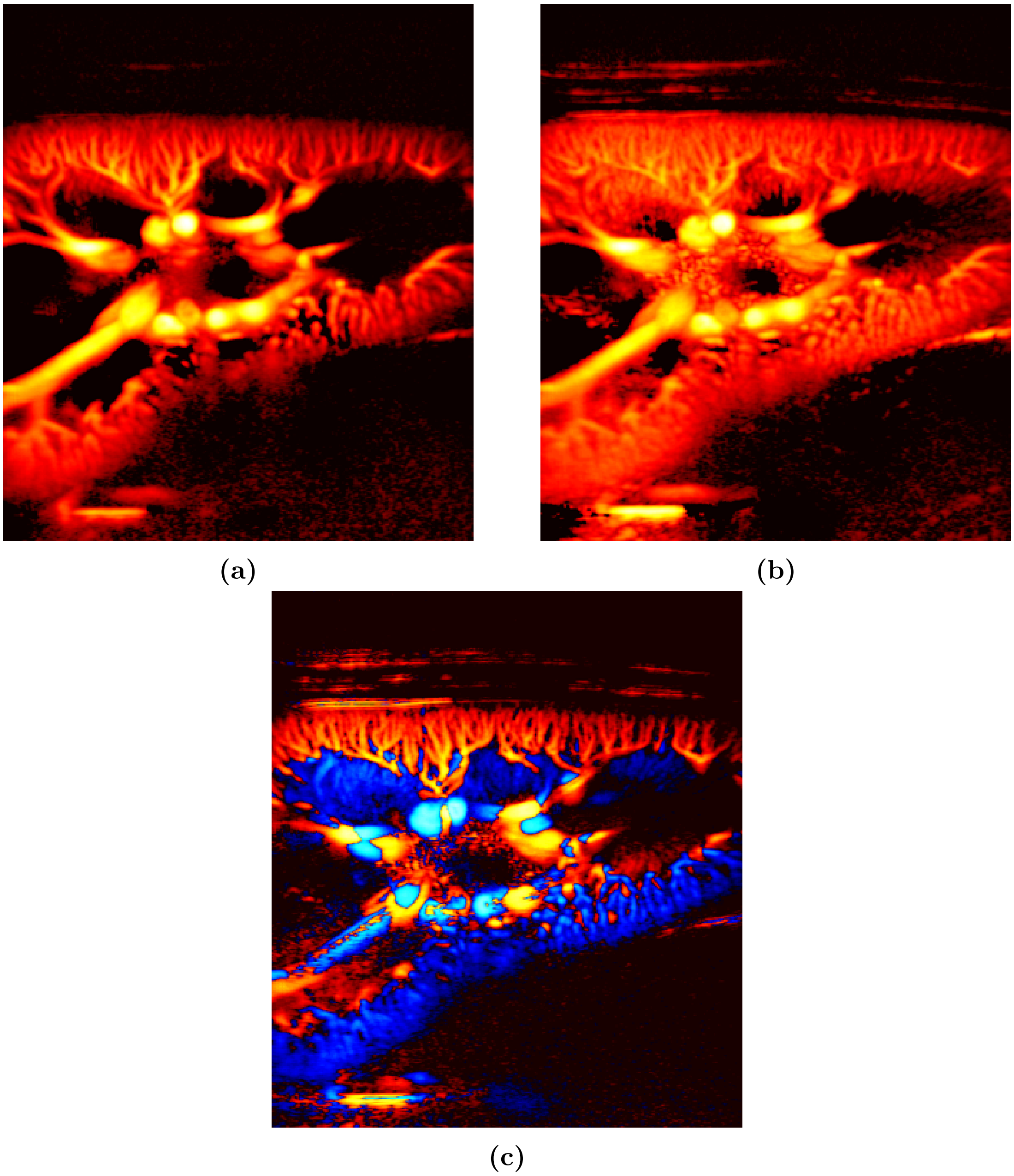

Figure 3.9: Results for different wall filters. Images (a) and (b) show the effects of a different lag between the two subtracted images, analysed using ASAP. The first image has a cut-off frequency of f = 187Hz, corresponding to a vertical blood velocity of v = 36mm/s, the second one of f = 31Hz or v = 6mm/s. The image in (c) shows the ability to discriminate different flow directions. Dynamic range is 50dB, averaging over 1000 frames (about 1.3 sec), corresponding blood vertical velocity is calculated with respect to the transmitted frequency.

but cannot reduce global variations of the noise, while ASAP can reduce the noise mean close to zero globally if sufficient number of frames are used.

By adjusting the signal processing chain, flow of different speeds and direction could also be separated. Having such a rapid reduction of the noise floor increases the ability to detect small vessels while maintaining the image frame rate for real-time applications.

From an implementation point of view, during PD the output of a single pixel is squared by multiplying it by its own conjugate. The only practical difference in our approach is that the multiplication is performed with two different numbers, belonging to two different beamforming outputs. The computational load of this parallel process is therefore the same as for PD, meaning that real-time implementation is achievable, requiring only a minimal upgrade of the machine, and possibly involving only software changes if digital beamforming is used.

The way we choose our apertures, w_1 and w_2, and our vector of samples b, affects the quality of the final image and its noise suppression. So far, we have populated our groups by sampling each channel at the time given by the delay and sum algorithm. For example, our apertures have been chosen by alternately placing four consecutive channels in one of the two groups.

It has been shown that grouping channels in two non-overlapping apertures is likely to create interference signals, in the form of side and grating lobes, which are negatively-correlated between the two groups [52]: such effects and their potential impact on the image have to be taken into account when apertures are chosen. This is because, while the sign of the correlation helps differentiate between main and side-lobe signals, strong interference may mask the signal coming from a weak target next to a strong one.

The results show that, in general, increasing the number of adjacent channels in each group moves the interference pattern closer to the main lobe. On the other hand, to great a reduction in the number of neighbouring channels used in each aperture will increase the grating-lobes while weakening the side-lobes: in the extreme case, where channels are used alternately in each aperture (i.e. odd channels in the first aperture and even channel in the second one), the result is effectively similar to using two transducers with doubled pitch. Approximate estimation of the result of a given choice of aperture can easily be computed using k-space methods [13], especially for linear targets.

To mitigate such effects, other ways of grouping the samples can be used, such as selecting different time instants of the waveform for each group. For example, assuming that the Born approximation holds and no non-linear scatterers are present (i.e. we are not using microbubbles), we could correlate the signal beamformed on each pixel with the one half a wavelength below in the depth direction. As the transmitted wave is known, the expected correlation between such signals is known as well, and ASAP can therefore be used.

In [112], we have also shown that this method works by correlating pixels belonging to the same point spread function after beamforming, in image sequences after envelope detection (B-mode images), and it is therefore a good candidate for a post-processing method to increase the quality of PD acquisitions. A combination of both methods could be used to improve noise suppression and enhance the quality of the final image. The number of apertures can also be increased and their combined cross-correlation calculated in different ways.

ASAP can also be combined with other methods for reducing side and grating lobes, such as DAX beamforming [109, 108], where the transducer aperture is also divided into sub-apertures to increase the quality of B-mode images, and minimum variance beamforming methods [42].

Lastly, we note that a trivial implementation of the technique may give undesirable results when imaging targets at very large depths or in the presence of strong aberration. Such situations may in fact change the steering vector associated with targets (delays) and, therefore, signals of interest may be misinterpreted as interference, as happens in classical minimum variance beamforming; this will result in a weaker signal. While the results presented are promising, as they are generated using a clinical probe, we speculate that in the aforementioned situations a more sophisticated or adaptive way of choosing the apertures may be necessary. This will be the subject of the next chapter. However, as we are using a clinical linear probe, the technique could be readily applied to those applications currently suitable for such linear probe, particularly for imaging small/micro-vasculature in e.g. breast, head and neck, and small body parts.

The ability to image small vessel flow with good contrast, resolution and penetration depth (centimetres) in vivo, using an affordable and portable/accessible technology such as ultrasound, could be of great value. It can be used to detect subtle changes that are relevant to early detection/characterisation in cancer, as well as treatment monitoring and evaluation, in transcranial ultrasound imaging of brain function [113](where signal to noise ratio is very poor due to skull attenuation), and in the evaluation of organ perfusion during transplantation.

Chapter 4

Minimum Variance ASAP

4.1 Black artefacts

While the ASAP approach is effective at reducing the noise floor in reconstruction, empirically we see black artefacts showing around bright objects in the final image: the reason why they appear as black is that we are setting any correlation having a negative real value to zero, since we know that the signal of interest must give positive correlation. This can lead to the undesirable masking of weak signals which are spatially overlapping with the side or grating lobes of bright structures. In this chapter we will evaluate why this happens and how this effect can be mitigated.

There have been many attempts in the literature to reduce the occurrence of interference artifacts for US imaging. Despite spatial windowing on the transducer elements, which merely corresponds to changing the apodization vector, adaptive methods have been largely employed to improve off axis signals rejection. The standard Minimum Variance (MV) beamformer of Capon [42] has been adapted multiple times to work with ultrasound for this purpose. In [30, 31], instead, the authors use the inverse problem nature of Fourier beamforming and DAS to incorporate the reconstruction process in a sparse signal recovery settings, reducing both noise and sidelobes.

Since we are assuming that noise is removed by the orthogonality of the two apertures, we could reformulate the ASAP problem as follows:

How to find two orthonormal apertures $\mathbf{w}_1$ *and* $\mathbf{w}_2$ *such that the signal of interest is preserved and the presence of black areas (i.e. negative correlations) is minimized?*

To do so, we have to understand how such black artefacts arise.

Noise reduction constraints

We start with a simple model for which the cross correlation matrix only contains the signal of interest and noise. To simplify, we further assume that the steering vector $\mathbf{a}_0$ associated with the signal of interest is known and equal to the apodization, $\mathbf{a}_0 \simeq \mathbf{a}$. This gives to $\mathbf{R}$ a structure given by

$$\mathbf{R}_0 = a \cdot \mathbf{a}\mathbf{a}^{\mathsf{H}} + \sigma_n \mathbf{I}, \tag{4.1}$$

where σ_n is the noise power, $\mathbf{I}$ is the identity matrix and a is the power in the direction of the signal of interest. The problem of ASAP is to seek for two vectors $\mathbf{w}_1$ and $\mathbf{w}_2$ that let the signal along the assumed steering vector $\mathbf{a}$ pass without distortion and also minimize the contribution of noise. That is equivalent to ask that

$$\mathbf{w}_1^{\mathsf{H}} \mathbf{R}_0 \mathbf{w}_2 = a. \tag{4.2}$$

Let's now decompose the apertures as the sum of two components

$$\mathbf{w}_i = \mathbf{a} + \mathbf{b}_i, \qquad \mathbf{a}^{\mathsf{H}} \mathbf{b}_i = 0, \tag{4.3}$$

where $\mathbf{b}_i$ is a vector lying in the subspace perpendicular to $\mathbf{a}$. In this case the result of the power estimation is given by

$$\begin{aligned}
\mathbf{w}_1^{\mathsf{H}} \mathbf{R}_0 \mathbf{w}_2 &= (\mathbf{a} + \mathbf{b}_1)^{\mathsf{H}} \mathbf{R}_0 (\mathbf{a} + \mathbf{b}_2) && (4.4)\\
&= (\mathbf{a} + \mathbf{b}_1)^{\mathsf{H}} (a \cdot \mathbf{a}\mathbf{a}^{\mathsf{H}} + \sigma_n \mathbf{I})(\mathbf{a} + \mathbf{b}_2) && (4.5)\\
&= a(\mathbf{a} + \mathbf{b}_1)^{\mathsf{H}} \mathbf{a}\mathbf{a}^{\mathsf{H}} (\mathbf{a} + \mathbf{b}_2) + \sigma_n (\mathbf{a} + \mathbf{b}_1)(\mathbf{a} + \mathbf{b}_2) && (4.6)\\
&= a + (\mathbf{a}^{\mathsf{H}} \mathbf{a} + \mathbf{b}_1^{\mathsf{H}} \mathbf{b}_2) \sigma_n && (4.7)\\
&= a + (1 + \mathbf{b}_1^{\mathsf{H}} \mathbf{b}_2) \sigma_n. && (4.8)
\end{aligned}$$

This shows that, in order to suppress noise, it is necessary that $\mathbf{b}_1^{\mathsf{H}} \mathbf{b}_2 = -1$. One simple way of doing that is given by choosing them in the set of unit norm vectors $\|\mathbf{b}_1\| = \|\mathbf{b}_2\| = 1$, then one gets

$$\mathbf{b}_1 = -\mathbf{b}_2. \tag{4.9}$$

To simplify the notation, we'll use the symbol $\mathbf{a}_\perp$ to denote a generic unitary vector that is perpendicular to $\mathbf{a}$. The two apertures are then finally expressed as

$$\mathbf{w}_1 = \mathbf{a} + \mathbf{a}_\perp, \qquad \mathbf{w}_2 = \mathbf{a} - \mathbf{a}_\perp. \tag{4.10}$$

It is important to note that the original way of performing ASAP by splitting the apertures into two sub-arrays can be described as in (4.10).

Effect of interference

In order to evaluate both the effect on the signal of interest, interferences and uncorrelated noise, the previous model for the cross correlation matrix has to be modified. Under the assumption of uncorrelated sources, the cross correlation matrix is given by

$$\mathbf{R} = a \cdot \mathbf{a}\mathbf{a}^{\mathsf{H}} + \sum_i \sigma_i \cdot \mathbf{e}_i \mathbf{e}_i^{\mathsf{H}} + \sigma \mathbf{I}, \tag{4.11}$$

where $\sigma_i \geq 0$ and $\mathbf{e}_i$ are respectively the power and the steering vector associated to the i-th interference. Note that this model works only when a large number of samples is used, otherwise (especially when less samples than channels are used) noise samples have to be modelled as interference.

The presence of black regions can now be explained. We first note that both the point spread function of ultrasound systems and linear array theory shows that sidelobes are much weaker than half of the mainlobe amplitude (usually referred as Half Maximum, HM): this means that the steering vector $\mathbf{e}_i$ associated with interference is almost perpendicular to the signal of interest steering vector, that is

$$\mathbf{a}^{\mathsf{H}} \mathbf{e}_i = \varepsilon_i, \qquad \|\varepsilon_i\| \ll \frac{1}{2}. \tag{4.12}$$

Focusing on a single interferer and assuming for simplicity that it is indeed perpendicular to the signal of interest ($\mathbf{a}^{\mathsf{H}} \mathbf{e}_i = 0$), the cross correlation matrix is $\mathbf{C} = \sigma_i \mathbf{e}_i \mathbf{e}_i^{\mathsf{H}}$ and the ASAP estimation is

$$ASAP = \mathbf{w}_1^{\mathsf{H}} \mathbf{C} \mathbf{w}_2 = \sigma_i (\mathbf{a}^{\mathsf{H}} + \mathbf{a}_{\perp}^{\mathsf{H}}) \mathbf{e}_i \mathbf{e}_i^{\mathsf{H}} (\mathbf{a} - \mathbf{a}_{\perp}) = -\|\mathbf{a}_{\perp}^{\mathsf{H}} \mathbf{e}_i\|^2. \tag{4.13}$$

This highlights how off-axis signals will always be seen as negative correlations whose magnitude depends on $\|\mathbf{a}_{\perp}^{\mathsf{H}} \mathbf{e}_i\|^2$. An illustration of this calculation can be seen in Fig. 4.1. Therefore, if our goal is to mitigate such problem while rejecting uncorrelated noise , we should try to find a vector $\mathbf{a}_{\perp}$ that is as much orthogonal as possible with respect to the interferences, such that

$$\|\mathbf{a}_{\perp}^{\mathsf{H}} \mathbf{e}_i\|^2 \to 0. \tag{4.14}$$

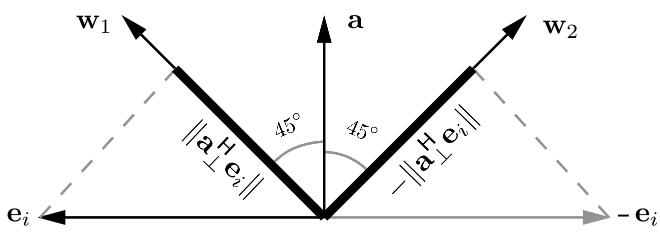

Figure 4.1: Illustration of how negative correlation arise from interference signals.

4.2 Dual apertures minimum variance beamforming

From Sec. 1.2.5, we recall that the aim of MV beamforming is to extract the power of the incoming signal supposedly steered in the direction $\mathbf{a}$, while rejecting as much as possible of the power of other interferences. To do so, one seeks to find the apodization $\mathbf{w}$ which solves the following minimization problem

$$\min_{\mathbf{w}} \mathbf{w}^{\mathsf{H}}\mathbf{R}\mathbf{w}, \qquad \text{with } \mathbf{w}^{\mathsf{H}}\mathbf{a} = 1. \tag{4.15}$$

We could exploit this framework to minimize the power of interferences associated with the two apertures $\mathbf{w}_1$ and $\mathbf{w}_2$, in order to reduce the appearance of black artefacts. It is not possible to directly minimize the estimate $\mathbf{w}_1^{\mathsf{H}}\mathbf{R}\mathbf{w}_2$, as its result is a general complex number, which doesn't have an associated natural notion of number ordering and therefore no concept of minimum. Nor one could seek for the apertures pair that minimizes the real part of the result, as the presence of negative correlations means that the optimal minima is a negative number, which implies that such a procedure would maximize the presence of black artefacts, rather than minimizing it. Lastly, it is not possible to maximise $\mathbf{w}_1^{\mathsf{H}}\mathbf{R}\mathbf{w}_2$, as it would give minimum noise rejection.

Instead, we define the following cost function

$$J(\mathbf{w}_1, \mathbf{w}_2) = \frac{1}{2}\left(\mathbf{w}_1^{\mathsf{H}}\mathbf{R}\mathbf{w}_1 + \mathbf{w}_2^{\mathsf{H}}\mathbf{R}\mathbf{w}_2\right). \tag{4.16}$$

This is a real and positive function for which we could seek a minimum. However, as in MV, we have to add some constraint to the minimization problem to obtain meaningful solution. We choose the following constrains:

$$\mathbf{w}_1^{\mathsf{H}}\mathbf{a} = 1, \qquad \mathbf{w}_2^{\mathsf{H}}\mathbf{a} = 1, \qquad \mathbf{w}_1^{\mathsf{H}}\mathbf{w}_2 = 0, \qquad \mathbf{w}_2^{\mathsf{H}}\mathbf{w}_1 = 0. \tag{4.17}$$

The first two of them ensure a distortionless response in the direction of interest, while the last two ensure that the two apertures are orthogonal and, by consequence, that noise is asymptotically removed. To find a minimum while enforcing such constraint, we use the method of Lagrange multipliers, by defining the Lagrangian function

$$L = \frac{1}{2}\left(\mathbf{w}_1^{\mathsf{H}}\mathbf{R}\mathbf{w}_1 + \mathbf{w}_2^{\mathsf{H}}\mathbf{R}\mathbf{w}_2\right) + \alpha(\mathbf{w}_1^{\mathsf{H}}\mathbf{a} - 1) + \beta(\mathbf{w}_2^{\mathsf{H}}\mathbf{a} - 1) + \gamma(\mathbf{w}_1^{\mathsf{H}}\mathbf{w}_2) + \delta(\mathbf{w}_2^{\mathsf{H}}\mathbf{w}_1), \quad (4.18)$$

where α, β, γ and δ are the unknown Lagrange multipliers. This function is not guaranteed to have a single global minimum anymore, so finding a closed form solution for such minimum is a hard mathematical problem. It is possible, however, to use alternate minimization to iteratively find the solution for $\mathbf{w}_1$ and $\mathbf{w}_2$ while keeping the other one fixed.

Let's start by taking the gradient with respect to $\mathbf{w}_1^{\mathsf{H}}$, while keeping $\mathbf{w}_2$ fixed, and setting it to zero. The resulting expression is

$$\frac{\partial L}{\partial \mathbf{w}_2^{\mathsf{H}}} = \mathbf{R}\mathbf{w}_1 + \alpha\mathbf{a} + \gamma\mathbf{w}_2 = 0, \quad (4.19)$$

whose solution for $\mathbf{w}_1$ is

$$\mathbf{w}_1 = -\mathbf{R}^{-1}(\alpha\mathbf{a} + \gamma\mathbf{w}_2), \quad (4.20)$$

assuming that $\mathbf{R}$ is invertible. By multiplying on the left side by $\mathbf{w}_2$ and $\mathbf{a}$, and using the constraint of eq (4.17), one gets the following system of equations

$$0 = \alpha\mathbf{w}_2^{\mathsf{H}}\mathbf{R}^{-1}\mathbf{a} + \gamma\mathbf{w}_2^{\mathsf{H}}\mathbf{R}^{-1}\mathbf{w}_2 \quad (4.21)$$

$$1 = -\alpha\mathbf{a}^{\mathsf{H}}\mathbf{R}^{-1}\mathbf{a} - \gamma\mathbf{a}^{\mathsf{H}}\mathbf{R}^{-1}\mathbf{w}_2. \quad (4.22)$$

For convenience, let's define the following quantities

$$x = \mathbf{w}_2^{\mathsf{H}}\mathbf{R}^{-1}\mathbf{w}_2, \qquad y = \mathbf{w}_2^{\mathsf{H}}\mathbf{R}^{-1}\mathbf{a}, \qquad z = \mathbf{a}^{\mathsf{H}}\mathbf{R}^{-1}\mathbf{a}, \quad (4.23)$$

which are given, as $\mathbf{w}_2$ is considered fixed. At this point, the system of equations (4.21) and (4.22) becomes

$$0 = \alpha y + \gamma x \quad (4.24)$$

$$-1 = \alpha z + \gamma y^*, \quad (4.25)$$

that can been easily solved to obtain

$$\alpha = \left(\frac{\|y\|^2}{x} - z \right)^{-1} \tag{4.26}$$

$$\gamma = -\frac{y}{x}\alpha. \tag{4.27}$$

With known Lagrange multipliers, they can be substituted in eq. (4.20) to find the first estimate aperture. At this point, the same procedure can be applied to the second aperture. Alternating between optimizing the two apertures gives us the estimate of the optimal pair to use for ASAP, assuming that the constrained problem has no local minima. Performing ASAP in this way is what we call Minimum Variance ASAP.

Note that the cross correlation matrix used while estimating the apertures can be a regularized version of the actual sample cross correlation matrix $\mathbf{R}$. This is often necessary for MV beamforming in US, as the knowledge of the steering vector is most surely inaccurate. Moreover, we use samples in the Doppler / slow-time domain to construct the matrix $\mathbf{R}$, rather than samples taken at different depths. For our approach, it is not possible to use methods such as subarray averaging [45] as it would spread the noise away from the diagonal elements, in which case the orthogonality of the two apertures will remove the noise only partially.

On the other hand, there's no harm in performing diagonal loading [45], so we'll choose this method to improve the performances of our approach. Diagonal loading works by adding a small constant value on the elements of the covariance matrix diagonal, such that

$$\mathbf{R}' = \mathbf{R} + \varepsilon \mathrm{Tr}(\mathbf{R})\mathbf{I}, \tag{4.28}$$

with ε equal to an arbitrary small positive value.

Note on convergence

The convergence of the alternate minimization scheme can be easily proved. First of all, note that since $\mathbf{R}$ is a positive definite matrix, meaning that $\forall \mathbf{v} \neq \mathbf{0}, \mathbf{v}^{\mathsf{H}}\mathbf{R}\mathbf{v} > 0$, then also the function J of eq. (4.16) is positive. In particular, each of the factors of J is positive. At each step, we keep one aperture fixed and optimize for the other one. Assuming that $\mathbf{w}_2$ is kept fixed, the optimization problem form $\mathbf{w}_1$ becomes

$$\min_{\mathbf{w}_1} \frac{1}{2}\mathbf{w}_1^{\mathsf{H}}\mathbf{R}\mathbf{w}_1, \qquad \text{s.t. } \mathbf{w}_1^{\mathsf{H}}\mathbf{w}_2 = 0, \quad \mathbf{w}_1^{\mathsf{H}}\mathbf{a} = 1. \tag{4.29}$$

If we perform a change of basis such that $\mathbf{w}_2 = k(1, 0, 0 \ldots, 0)^{\mathsf{H}}$, then the problem can be restated as

$$\min_{\hat{\mathbf{w}}_1} \begin{pmatrix} 0 & \hat{\mathbf{w}}_1{}^{\mathsf{H}} \end{pmatrix} \begin{pmatrix} a & \mathbf{b}^{\mathsf{H}} \\ \mathbf{c} & \hat{\mathbf{R}} \end{pmatrix} \begin{pmatrix} 0 \\ \hat{\mathbf{w}}_1 \end{pmatrix}, \qquad \text{s.t.} \begin{pmatrix} 0 & \hat{\mathbf{w}}_1^{\mathsf{H}} \end{pmatrix} \begin{pmatrix} a_1 \\ \hat{\mathbf{a}} \end{pmatrix} = 1 \tag{4.30}$$

where

$$\mathbf{w}_1 = \begin{pmatrix} 0 \\ \hat{\mathbf{w}}_1 \end{pmatrix}, \quad \mathbf{a} = \begin{pmatrix} a_1 \\ \hat{\mathbf{a}} \end{pmatrix} \quad \text{and} \quad \mathbf{R} = \begin{pmatrix} a & \mathbf{b}^{\mathsf{H}} \\ \mathbf{c} & \hat{\mathbf{R}} \end{pmatrix}. \tag{4.31}$$

The 0 in the first entry of $\mathbf{w}_1$ is due to the requirement of orthogonality with respect to $\mathbf{w}_2$. Solving this problem is equivalent to solving

$$\min_{\hat{\mathbf{w}}_1} \hat{\mathbf{w}}_1 \hat{\mathbf{R}} \hat{\mathbf{w}}_1 \qquad \text{s.t. } \hat{\mathbf{w}}_1{}^{\mathsf{H}} \hat{\mathbf{a}} = 1. \tag{4.32}$$

The solution of this problem is unique and given by Capon [42]. Let's assume that the value of the cost function at the solution is

$$\lambda_0 = \mathbf{w}_1^{\mathsf{H}} \mathbf{R} \mathbf{w}_1. \tag{4.33}$$

Next, the vector $\mathbf{w}_2$ is updated and, at a second step, the algorithm updates the vector $\mathbf{w}_1$ again. This will give a new value λ_1 for the cost function. Such value has the following property

$$0 < \lambda_1 \leq \lambda_0. \tag{4.34}$$

This shows that, at each step of the algorithm, the value of the cost function for the aperture $\mathbf{w}_1$ can't increase and is bounded from below by 0. Therefore, the algorithm converges. The same argument can be used to prove that also $\mathbf{w}_2$ converges.

4.3 ASAP as noise estimation and subtraction

Another way of looking at ASAP can be given by using the fact that only the real part of the estimated is used. This modifies the estimation as

$$ASAP = \frac{1}{2}(\mathbf{w}_1^{\mathsf{H}} \mathbf{R} \mathbf{w}_2 + \mathbf{w}_2^{\mathsf{H}} \mathbf{R} \mathbf{w}_1). \tag{4.35}$$

By substituting eq. (4.10) in the above, the result is

$$ASAP = \frac{1}{2}\left[(\mathbf{a}+\mathbf{a}_{\perp})\mathbf{R}(\mathbf{a}-\mathbf{a}_{\perp}) + (\mathbf{a}-\mathbf{a}_{\perp})\mathbf{R}(\mathbf{a}+\mathbf{a}_{\perp})\right] \tag{4.36}$$

$$= \mathbf{a}^{\mathsf{H}}\mathbf{R}\mathbf{a} - \mathbf{a}_{\perp}^{\mathsf{H}}\mathbf{R}\mathbf{a}_{\perp}. \tag{4.37}$$

The first term of eq. (4.37) is the standard PD estimate on the direction $\mathbf{a}$, while the second term of the sum is the PD estimate on the direction $\mathbf{a}_{\perp}$. What this is showing is that the way ASAP reduces noise is given by estimating its power as the variance along the direction $\mathbf{a}_{\perp}$ and then subtracting this value from the PD estimate.

Once more, this shows why the choice of $\mathbf{a}_{\perp}$ is crucial, as it must contain noise at its average power while neglecting interferences. If $\mathbf{a}_{\perp}$ contains the power of an interfering signal that is stronger than the main lobe power, negative values arise and by consequence black artefacts.

This results also shows that another way to minimize the risk of black artefacts is given by finding a more robust way of estimating noise power and then simply subtract its value from the PD estimate.

4.3.1 Noise estimate on spatial Fourier spectra

A different way of estimating noise can be derived from the assumption that the received echoes lie in a lower dimensional subspace than the original $\mathbf{x}$. One way to find such subspace by decomposing via SVD the cross correlation matrix, as done in many adaptive beamforming methods [48]

$$\mathbf{R} = \mathbf{U}\mathbf{S}\mathbf{U}^{\mathsf{H}}, \tag{4.38}$$

where $\mathbf{S}$ is a diagonal matrix containing the sorted eigenvalues and $\mathbf{U}$ is the basis matrix made by the associated eigenvectors. Because of the assumed independence of noise, with a large number of samples the eigenvectors corresponding to the highest eigenvalues will span the echoes subspace, while the ones corresponding to the lowest eigenvalues will span the noise subspace: the latter is a convenient vector space in which we can estimate the noise variance.

Given the above considerations, one could try to reduce noise as follows:

1. Calculate the cross correlation matrix $\mathbf{R} = \sum_t \mathbf{x}(t)\mathbf{x}^{\mathsf{H}}(t)$

2. Decompose it via SVD to get $\mathbf{R} = \mathbf{U}\mathbf{S}\mathbf{U}^{\mathsf{H}}$, then keep only the lowest k eigenvectors into the matrix $\mathbf{U}_k$.

3. Generate a random unit norm vector $\mathbf{r} \in \mathbb{R}^k$, project it into the noise subspace to get $\mathbf{b} = \mathbf{U}_k\mathbf{U}_k^{\mathsf{H}}\mathbf{r}$ and use this vector to estimate noise $\sigma_n = \mathbf{b}^{\mathsf{H}}\mathbf{R}\mathbf{b}$.

4. Estimate the signal power as $\mathbf{a}^{\mathsf{H}}\mathbf{R}\mathbf{a} - \sigma_n$.

There are two main problems with such approach:

1. It is not easy to find a k that divides noise and interference subspace, even if the assumptions made are correct. Moreover, is unlikely that the same k works for all the different spatial locations, therefore another adaptive method should be included on top of it to estimate the dimensionality of the noise subspace.

2. While in the limit of an infinite number of measurements the noise cross correlation matrix will theoretically be diagonal and flat, in reality the values along the diagonal will be different and, in general, the SVD decomposition will sort them in descending order, therefore focusing in the lower subspace spanned by the lower eigenvalues will necessarily make ASAP underestimate the noise variance and by consequence degrade its noise reduction performances. In particular, note that setting k to its maximum possible value, that is estimating the noise power as the smallest eigenvalue, corresponds to maximizing the expression in eq. (4.35) under the unit norm constraint for $\mathbf{a}_\perp$, which gives the smallest possible noise rejection.

Those two issues come from the nature of the basis extracted by the SVD method. In order to overcome them, we seek for a basis that eases the task of separating interference and noise subspaces. From antenna theory, the steering vectors associated with echoes in the far field are given by complex exponentials, that is the $\mathbf{e}_i$ in eq. (4.11) have the form

$$\mathbf{e}_i = e^{jk_ic}, \tag{4.39}$$

where k_c is the spatial frequency and c is the channel index. On the other hand, by definition white noise has a flat spectrum in the Fourier domain: once more, as in ASAP, we are assuming that noise has the same power for each channel and is independent between them. If the number of interfering echoes is small compared to the dimensionality of the channel space, it is then reasonable to assume that the Fourier transform of the cross correlation matrix presents few peaks on the diagonal due to the interference echoes and a constant contribution on all diagonal elements due to noise, that is the representation of the interferences in the Fourier domain is sparse. This hypothesis is justified when imaging the vasculature, as it is not homogeneously diffused in US images.

With those consideration, the adaptive way of estimating and compensating for noise is given by the following steps:

1. Express the cross correlation matrix in the Fourier basis by calculating $\hat{\mathbf{R}} = \mathbf{F}^{\mathsf{H}}\mathbf{R}\mathbf{F}$, where $\mathbf{F}$ is the Fourier matrix
2. Extract the spectrum $s(i)$, given by the diagonal of $\hat{\mathbf{R}}$
3. Find the lowest entry $\sigma_i = \min s(i)$ of the spectrum vector and assume its power is equal to noise $\sigma_n = \sigma_i$
4. Estimate the signal power as $\mathbf{a}^{\mathsf{H}}\mathbf{R}\mathbf{a} - \sigma_n$.

Note that the cross correlation matrix used for the power estimation may be different than the one used to find the noise power in practice, the latter has to be made with a large number of samples while the first one can be made by the most recent samples.

4.4 Methods

4.4.1 Processing methods

We compare the results of the proposed noise subtraction method against three more techniques. The first one being standard PD, the second one is ASAP performed using two random orthogonal apertures and the last one is first lag autocorrelation [41]. We have also used MV beamforming with diagonal loading, where the diagonal load is always set the same for both standard MV beamforming and MV ASAP: if not differently specified, the diagonal load value is always $\varepsilon = 0.01$. Due to the fast convergence properties of the alternating minimization, we stop the search for the pair of apertures at 100 iterations for the simulation and to 1000 iterations for the in-vitro data.

4.4.2 Simulations

To get an idea of how negative correlation arises, we performed simulation using Field II [1], by placing a single scatter 2.5cm below a line transducer of 128 elements, with 0.3mm of pitch transmitting a 5MHz 2cycles pulse. In order to simulate the decorrelation of the scatter signal due to motion, we used the model for microbubble Doppler acquisitions described in [37], which states that the correlation function of the Doppler signal is given by the product of a Gaussian function with a modulating complex exponential

$$R(\tau) = \exp\left(-\frac{\tau^2}{2\tau_c^2} + j2\pi\omega_c\tau\right), \tag{4.40}$$

where ω_c is the Doppler frequency and τ_c is the correlation time, that depends on the bandwidth, microbubble motion and physical changes of the microbubbles [37]. In the simulations, unless specified, we use a correlation time of $\tau_c = 4$ pulses and a normalized Doppler frequency of $\omega_c = 0.25$ for evaluating the effect of black artefacts in existing technique, and a normalized Doppler frequency of $\omega_c = 0.1$ when we compare the performance of the different methods. The number of transmit angles is equal to 5, steered between -20 and +20 degrees and not compounded: that is, each transmission is treated as a single image, in order to avoid the intensity reduction effects described in Chapter 2. We used uniform apodization in receive for all experiments, acquiring a total of 250 frames for the simulations used to explain the black artefact issue, and a total of 5000 transmissions for the evaluation of the proposed methods. No noise has been added unless specified.

We remark that those values are purely indicative and used to show the effects of motion in the vicinities of the mainlobe region: to get a comprehensive idea of how different parameters affect the appearance of negative correlation one should try many different combination of the parameters. Here, we concentrate on values that are of interest when fast flow is being imaged.

4.4.3 In-vitro evaluation

The evaluation of the technique has been made in vitro, using the same setup as used for the previous chapter. A tube with microbubbles flowing at 20cm/s in a 200 μm tube has been imaged in cross-section. The microbubble infusion was made using a concentration of 0.1mL of SonoVue contrast agent (SonoVue, Bracco Imaging SpA, Milan, Italy) per liter of water.

The transmission sequence was made of 4MHz pulses of single cycle with a scanning depth of 5cm. The number of compounded plane waves is equal to 11, equispaced between -20 and 20 degrees, and PI is used. A total of 10 acquisitions has been made and averaged to obtain the quantification results.

The acquisitions have been processed both with and without using coherent compounding, which means that we consider each transmission as a single frame. The reason to do so is to evaluate the performances of the methods also for cases when there's a large motion that can attenuate the coherent compounding signal, as shown in Chapter 2.

In the processing the in-vitro data, the apodization used both for the non-adaptive approaches and as reference steering vector for the adaptive methods, is given by the element sensitivity of the array elements, which is assumed as a Gaussian depending on the angle made by the element surface with the beamformed location, having a variance of 15°.

4.4.4 In-vivo

The rabbit kidney acquisition described in Chapter 3 was used to assess the performances of the proposed method in-vivo. The acquisition was made using 15 angles between -18 and 18 degrees but without performing compounding on them. The transmit sequence was made of 4MHz single-cycle pulse with a total frame rate of 750Hz. Pulse inversion was used and the data has been high pass filtered using a 6th lag difference filter having impulse response $h = (1, 0, 0, 0, 0, 0, 1)$, as described in Chapter 3.

4.4.5 Image quality metrics

To evaluate the image quality, we use three metrics. The first one being the SNR, which is defined like for Chapter 3 as

$$SNR = \frac{\mathsf{E}[I_s]}{\mathsf{E}[I_n]}, \tag{4.41}$$

where $\mathsf{E}[I_s]$ is the average signal intensity and $\mathsf{E}[I_n]$ is the average noise intensity. The second metric gives the strength of the sidelobes, and is simply found as the ratio between the maximum sidelobe intensity in the image and the signal intensity. Lastly, the Peak negative sidelobe intensity is the ratio between the largest (in magnitude) negative sidelobe and the mainlobe intensity, which gives a measure of the amount of negative correlation in the image and therefore of artefacts. We also measured the Full-width Half-maximum (FWHM) as the size of the mainlobe when its amplitude is half: since we are dealing with power measure, the FWHM is find at the points where the PSF reaches 1/4 of its maximum value.

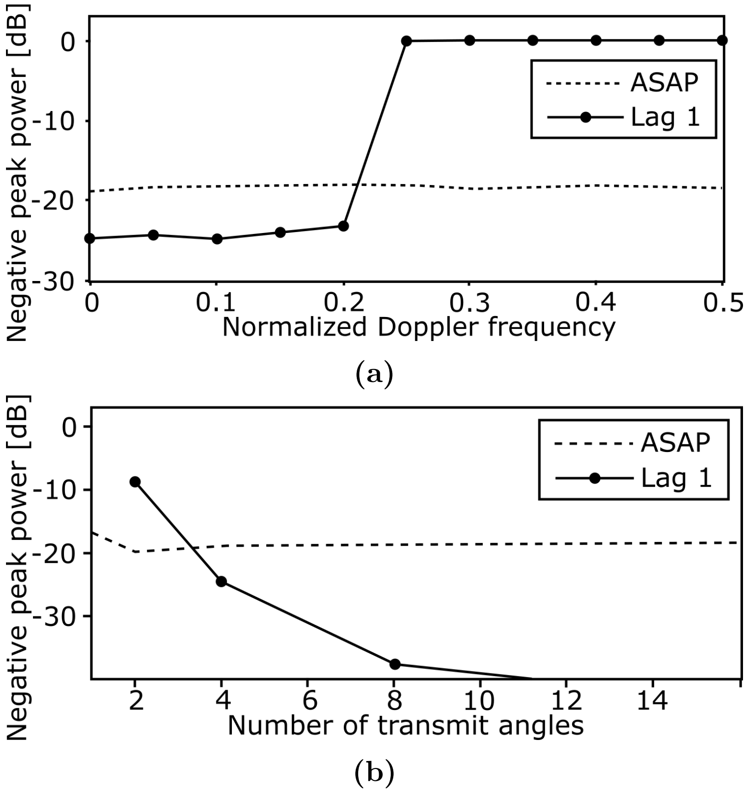

Figure 4.2: Effects of different velocities, given by different Doppler frequencies on the strength of the negative correlations (a) and effect of varying the number of angles on the strength of the power of negative correlations. The frequency axis is normalized by the Nyquist frequency.

4.5 Results

4.5.1 Simulations

We first evaluate how a different Doppler frequency affects the strength of negative correlations on the different processing methods. The results are shown in Fig. 4.2a. We have not shown PD in the figures, as the method is guaranteed to produce positive estimates for Doppler power: for the proposed methods, an analysis of the negative sidelobes follows later in the section. On the other hand, ASAP shows a constant peak negative estimate that is independent of the Doppler frequency: the independence on the scatter velocity is easily explained as ASAP processes the signal in the channel domain without any temporal lag. The first lag autocorrelation method also show a negative peak estimate below the one of ASAP for moderate Doppler frequencies, as the rotation of the point spread function affects the Doppler signal of the pixels associated with part of the sidelobes, giving negative correlations. As expected, the peak negative power goes to 0dB when the Doppler frequency

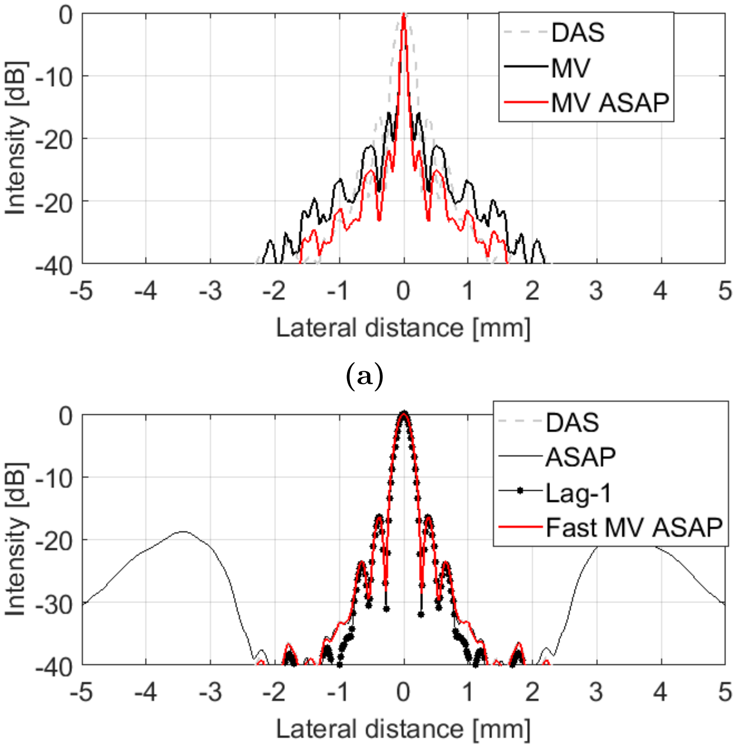

(b)

Figure 4.3: Lateral PSF for different processing methods in the noiseless case, $\varepsilon = 0.01$. The left plot shows the effect on minimum variance methods, the right plot shows the effect on ASAP, Lag-1 and the fast MV ASAP.

reaches 0.25, since in this case the signal associated to the mainlobe will have a negative correlation due to motion itself.

We have then studied how such negative correlations are affected by the number of transmitted angles. Once more, PD doesn't create negative correlations and therefore are not shown in the plot. For ASAP, we see that the strength of negative correlations is constant regardless of changes in the number of compounded angles, while on the other hand the first lag autocorrelation method seems to be very sensitive to the number of angles used, with a peak negative correlation of -9.5dB when 2 angles are used.

The plots in Fig. 4.3 show the lateral beam-plot obtained with different processing methods, when no noise is present in the data. The image in Fig. 4.3a compares the proposed MV ASAP method with DAS and standard MV beamforming, using a diagonal loading of $\varepsilon = 0.01$: we observe that both methods improve the resolution of the mainlobe but achieve different intensities for the sidelobes, for which the proposed method always show reduced sidelobes compared to MV beamforming. Both MV beamforming methods are found to have comparable resolution, which is

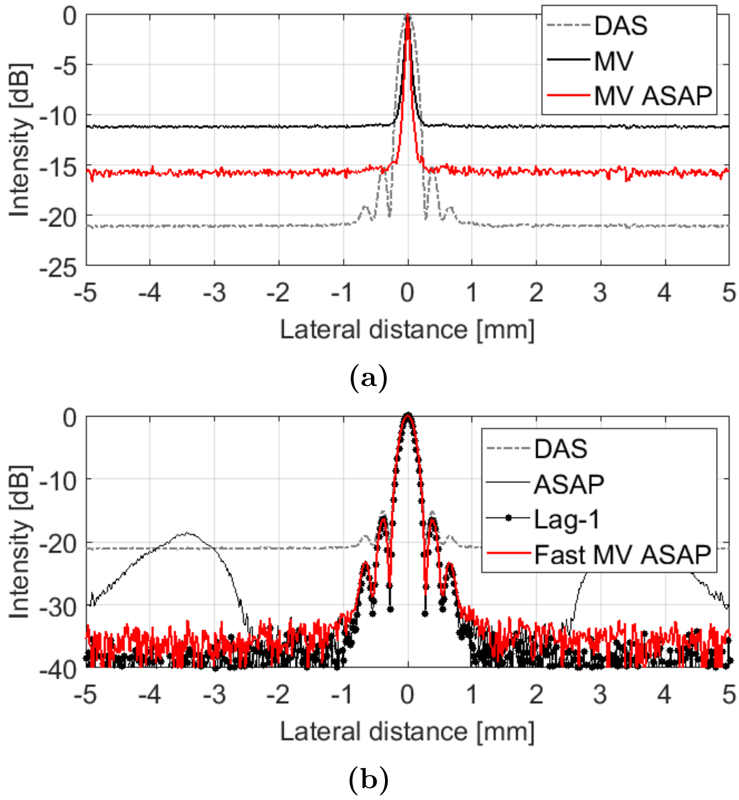

Figure 4.4: Lateral PSF for different processing methods in the noisy case, $\varepsilon = 0$.

clearly improved compared to DAS. The same plots are shown in Fig. 4.3b, where the proposed Fast MV ASAP technique is compared with other correlation methods: the algorithm clearly outperforms a standard implementation of ASAP using fixed apertures, as the high grating-lobes visible in the side of the ASAP beamplot are not found in the Fast MV ASAP technique. However, our method exhibits slightly higher sidelobes compared to Lag-1 autocorrelation.

The same evaluation has been done after adding white noise to the received data, to simulate a noisy scan. The power of the noise has been set equal to the power of the received signal. Diagonal loading has not been used, since the data already contain a large amount of noise. The lateral beam-plots of Fig. 4.4a are equivalent to Fig. 4.3a , but show that the proposed method is capable of reducing the noise floor by a factor of 4.7dB compared to standard MV beamforming while at the same time it produces a sharp mainlobe, improving resolution with respect to DAS, albeit still having a noise floor 5dB higher than the one achieved by DAS.

The image in Fig. 4.4b shows that the proposed Fast MV ASAP can reduce the noise floor to a level that is comparable to ASAP with fixed apertures and Lag-1 autocorrelation, without affecting resolution and once more without exhibiting the large grating lobes shown in the standard ASAP method.

	Noiseless case (μm)	Noisy case (μm)
DAS	326	329
ASAP	326	329
Lag-1	293	293
MV	91	156
Fast MV ASAP	326	326
MV ASAP	93	109

Table 4.1: FWHM in simulations for different processing methods, with diagonal loading $\varepsilon = 0.01$ for the noiseless case and no diagonal loading for the noisy case, using 3000 total transmissions and 5 different angles.

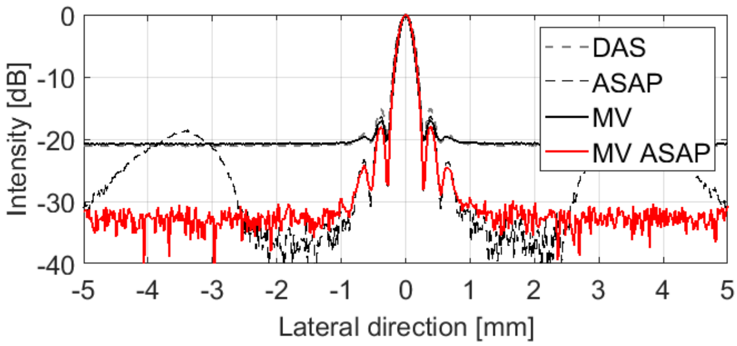

Figure 4.5: Lateral PSF for different processing methods in the noisy case, $\varepsilon = 1$.

The resolution of all the methods has been evaluated for the noisy and noiseless case, and is reported in Tab. 4.1. It is readily seen that the resolution of DAS, standard ASAP and Fast MV ASAP is not affected by the presence of noise, and stays around 326 μm,while on the other hand Lag-1 autocorrelation achieved a moderate improvement in resolution, going down to 293μm, but it is still constant regardless of the presence of noise. The resolution achieved by MV beamforming and MV ASAP is instead largely improved with respect to the other methods, reaching respectively 91 μm and 93 μm, an improvement of about the 350% with respect to DAS. In the presence of noise, the proposed method seems also to outperform the resolution achieved by MV beamforming, as they respectively produce an improvement of 300% and 210% over DAS.

As it is well known that MV approaches DAS when a large diagonal load is used, we hypothesize that a large diagonal loading would make MV ASAP approach standard ASAP. In fact, by looking at Fig. 4.5, we observe that setting a diagonal load of $\varepsilon = 1$ gives, for the MV beamforming, a beamplot which essentially overlaps with the DAS one; on the other hand, the MV ASAP lateral plot shows that it achieves a superior noise reduction, reaching an SNR of 33dB, very close to the 35.4dB of SNR obtained using ASAP with fixed apertures.

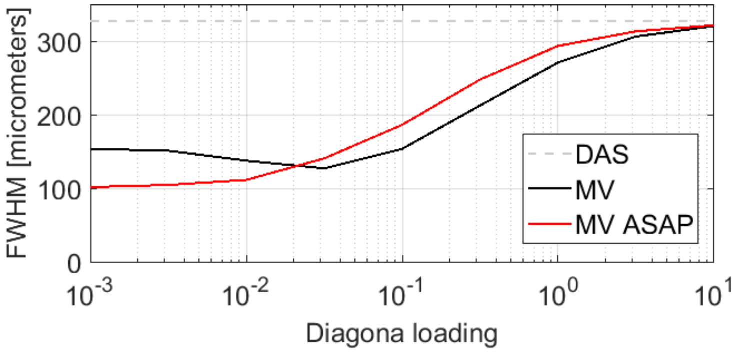

(a) FWHM

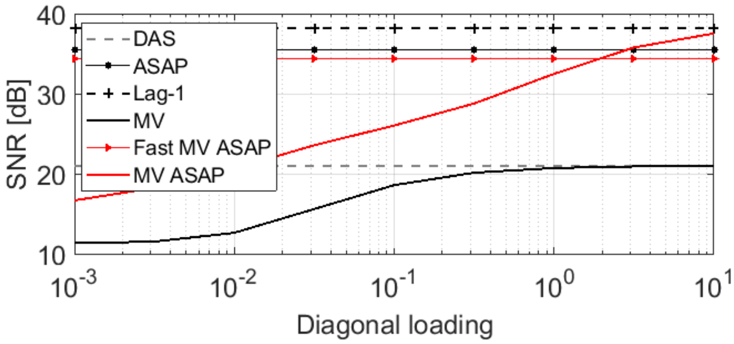

(b) SNR

Figure 4.6: SNR and FWHM for different processing methods in the noisy scenario.

A more systematic study of the FWHM and SNR for different diagonal loading factors, is given in Fig. 4.6. The plot of Fig. 4.6a show that, in presence of noise, low diagonal loading factors give to MV ASAP a lower FWHM compared to standard MV beamforming. This is true until a $\varepsilon = 0.02$ is used: for this value the FWHM of the two methods is the same, and for values above MV beamforming outperforms the proposed method. Lastly, both of them approach the resolution of DAS when a large diagonal loading is used.

The study of the SNR, shown in Fig. 4.6b, demonstrates how the use of orthogonal apertures allows a better noise rejection compared to MV beamforming. From $\varepsilon > 0.01$, the noise floor of MV ASAP constantly improves compared to DAS up to 36.7dB for $\varepsilon = 10$, while for standard beamforming the noise floor at most reaches the DAS value when a very large ε is used. The Fast MV ASAP approach exhibits an SNR of 34.5dB, which is just below the 35.4dB reached by standard ASAP, while Lag-1 autocorrelations shows the best noise rejection with an SNR of 37.5dB.

The last simulations are used to evaluate the side-lobe strength for different processing methods. Fig. 4.7a shows the level of the strongest sidelobe in absolute value: in the lower portion of the graph, MV ASAP show a decreasing apparent side-lobe intensity due to the noise presence, which is stronger than interferences

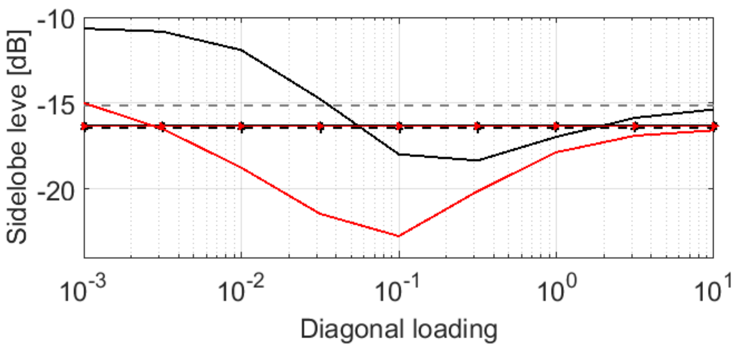

(a) Absolute sidelobe levels

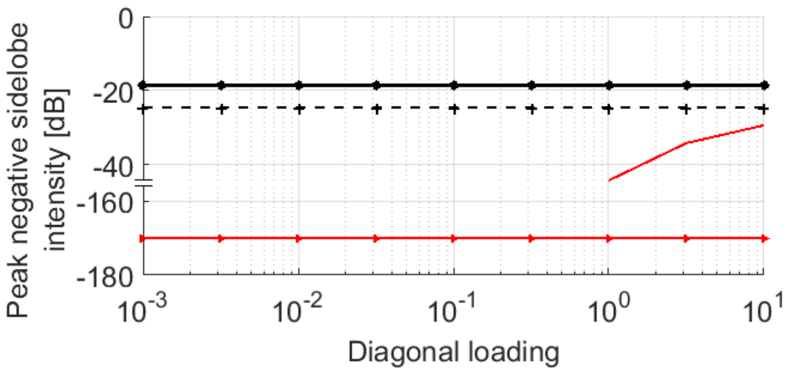

(b) Negative sidelobe peak level

Figure 4.7: Absolute sidelobe level and negative sidelobes level for different processing methods in the noisy scenario, for different values of diagonal loadings. Lines have the same colors and markers as for Fig. 4.6.

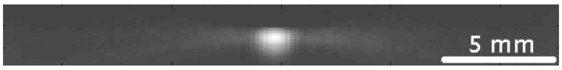

(a) Power Doppler

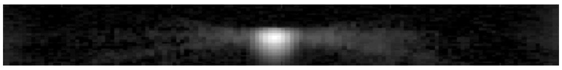

(b) Fast MV ASAP

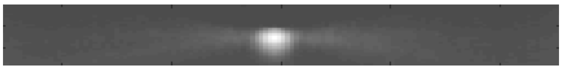

(c) MV $\varepsilon = 1$

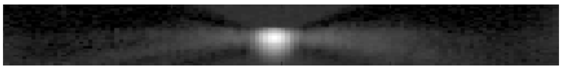

(d) MV ASAP $\varepsilon = 1$

(e) MV $\varepsilon = 0$

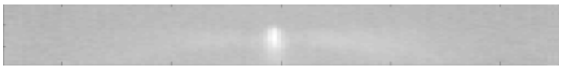

(f) MV ASAP $\varepsilon = 0$

Figure 4.8: Point spread function made by a cross section of a wire with flowing microbubbles with different processing methods. All the images are shown at 50dB of dynamic range.

and therefore dominates the sidelobe region. However, also for diagonal factors of $\varepsilon > 0.1$, our MV ASAP approach always show a reduced sidelobe strength compared with standard MV beamforming. The other correlation methods show a very similar and constant sidelobe level around -16.3dB, which is still below the -15dB shown by DAS.

The Fig. 4.7b shows instead the strength of the maximum negative side-lobe achieved by the different methods. Obviously, PD and MV beamforming don't appear in this graph, as they return postive values by construction (see Sec. 1.2.4 and 1.2.5). The image shows that ASAP and Lag-1 autocorrelation give the strongest negative sidelobes, with intensities of about -20dB and -22dB respectively. MV ASAP instead doesn't show any negative side-lobe until a diagonal loading of about $\varepsilon = 1$ is used, for which the sidelobe levels start rising until a value of about -30dB when $\varepsilon = 10$ is used. Fast MV ASAP, on the other hand, always show a very negligible negative sidelobe power.

4.5.2 In Vitro

We now look at how a tube with flowing microbubbles is imaged using different methods. The images in Fig 4.8 show how the use of Fast MV ASAP largely reduces the noise floor of the images compared to PD, and the same is true for the MV ASAP method with a diagonal loading of $\varepsilon = 1$, while the MV image strongly resembles the PD image in terms of noise intensity, as expected. Removing the diagonal load produces sharper images for the two adaptive beamforming methods, while on the other hand it shows a reduced noise floor for the MV ASAP technique compared to

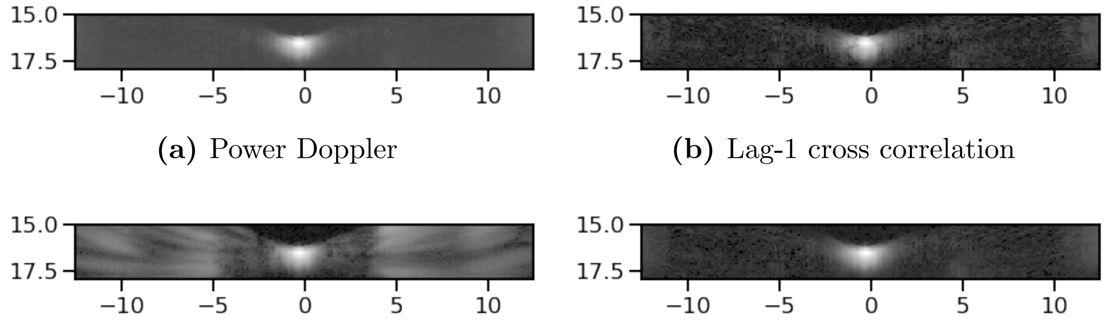

(a) Power Doppler

(b) Lag-1 cross correlation

(c) ASAP

(d) Fast MV ASAP

Figure 4.9: Point spread function made by a cross section of a wire with flowing microbubbles with different processing methods, with coherent compounding. Dynamic range is 60dB, axes are in millimetres.

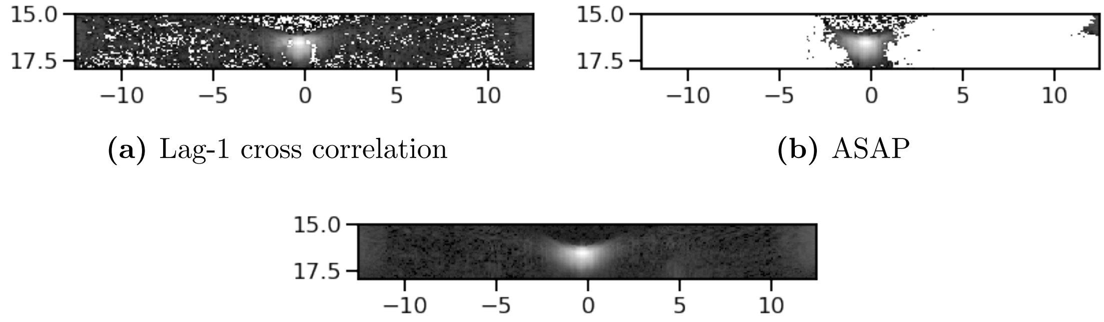

(a) Lag-1 cross correlation

(b) ASAP

(c) Fast MV ASAP

Figure 4.10: Point spread function made by a cross section of a wire with flowing microbubbles with different processing and coherent compounding, where negative correlations are shown in white. It is easily seen that the apperance of black artefacts, which are given by negative correlations, is dramatically reduced using the minimum variance method. Dynamic range is 60dB, axes are in millimetres.

standard MV.

Comparing the images of Fast MV ASAP and MV ASAP using orthogonal aperture, we find that while MV ASAP underperforms the fast method in terms of noise rejection, as it was expected given its noise dependence on the diagonal factor (see Fig. 4.6), it also appears that noise rejection is spatial dependent. It can be in fact observed that the region above the mainlobe exhibits a lower noise rejection than the surroundings. We will explain this in the Discussion section, but this observation led us believe that the MV ASAP method is better suited for noise reduction of MV images when the main concern is to have high resolution, and therefore a low diagonal loading.

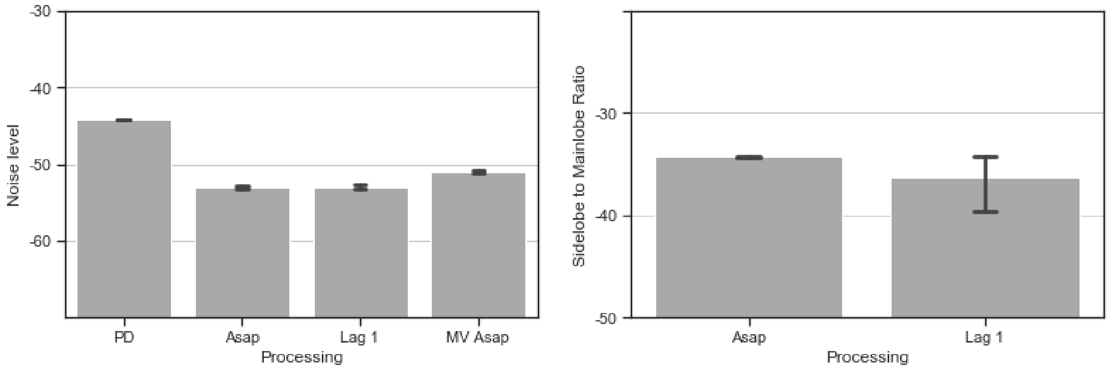

(a) Noise intensity **(b)** Negative sidelobes intensity

Figure 4.11: Normalized noise power and negative sidelobes to mainlobe level for the different second order statistical methods with coherent compounding. PD and Fast MV Asap don't show in the barplot (b) as they don't produce negative correlations.

We further estimate the effectiveness of the Fast MV ASAP approach by comparing its result over the same tube cross section with ASAP, Lag-1 autocorrelation and PD, both with and without coherent compounding.

Fig. 4.9 shows the results when coherent compounding is used. Once more, we see that the proposed method largely mitigates the interference effects that are given by ASAP. The images have been shown once more in Fig. 4.10, where negative correlations in white: we see that, among all, the proposed method has no negative correlations and therefore will prevent the masking of weak signals located in the vicinities of a strong scatterer. The noise reduction and negative average sidelobe levels are shown in Fig. 4.11: as expected from the simulations, the proposed approach slightly underperforms in noise rejection compared to the others method, giving an average noise level of -51dB, compared to the -53dB achieved by ASAP and Lag-1, but still well below the -44.5dB of PD. The negative sidelobes are however completely removed, while both ASAP and Lag-1 show significant negative correlations, of -34.5dB and -36.5dB respectively.

Such analysis has been performed on the same data without prior coherent compounding. The resulting PSFs are displayed in Fig. 4.12 in absolute value and in Fig. 4.13 with masked negative correlations. Again, the proposed approach doesn't show any negative correlations, while both ASAP and Lag-1 display large areas of negative correlations. The quantification of the processing methods performances is shown in Fig. 4.14. The proposed fast approach to MV ASAP shows a noise reduction of a bout 11dB compared to PD, which is once more lower than the 13dB of noise power reduction achieved by ASAP and the 16dB reduction of Lag-1. How-

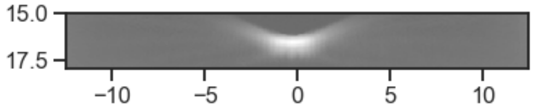

(a) Power Doppler

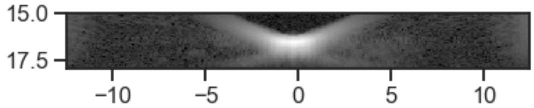

(b) Lag-1 cross correlation

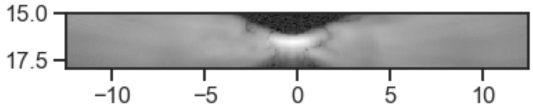

(c) ASAP

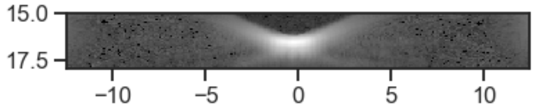

(d) Fast MV ASAP

Figure 4.12: Point spread function made by a cross section of a wire with flowing microbubbles with different processing methods, without coherent compounding. Dynamic range is 60dB, axes are in millimetres.

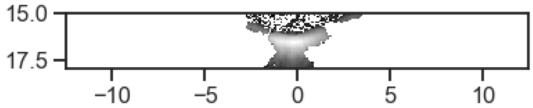

(a) Lag-1 cross correlation

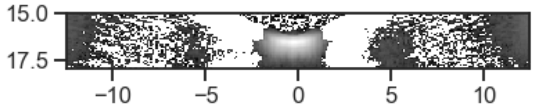

(b) ASAP

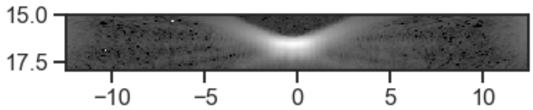

(c) Fast MV ASAP

Figure 4.13: Point spread function made by a cross section of a tube with flowing microbubbles and different processing, without coherent compounding, where negative correlations are shown in white. It is easily seen that the apperance of black artefacts, produced by negative correlations, is dramatically reduced using the minimum variance method. Dynamic range is 60dB, axes are in millimetres.

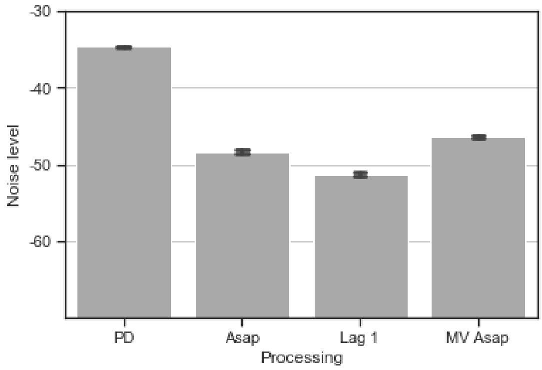

(a) Noise intensity

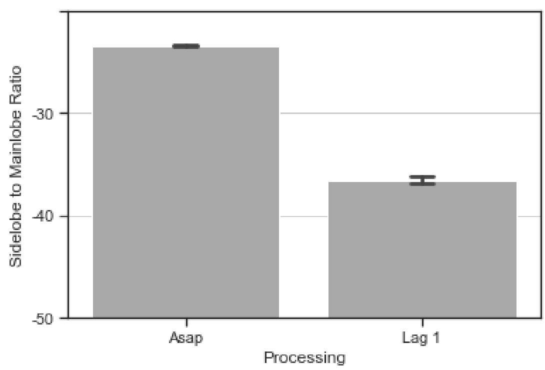

(b) Negative sidelobes intensity

Figure 4.14: Normalized noise power and negative sidelobes to mainlobe level for the different second order statistical methods without coherent compounding. PD and Fast MV Asap don't show in the barplot (b) as they don't produce negative correlations.

ever, we again find no negative correlations, while standard ASAP shows a negative sidelobe level of -24dB on average.

4.6 In vivo

The in-vivo results are shown in Fig. 4.15. From the image on top, we observe that the large noise level doesn't allow a clear distinction of the vasculature using standard PD. On the other hand, using ASAP as described in Chapter 3 gives a large reduction of the noise floor and highlight the vasculature. However, the lack of compounding and the dual aperture correlation gives rise to a large amount of black artefacts, especially in the regions surrounding vessels.

The proposed approach shows as well a large noise reduction compared to PD but with a great reduction of black regions compared to the ASAP image. The fact that such effects are not visible, in a region containing a large amount of vessels, gives strength to our hypothesis that the Fourier basis produces sparse Power spectra even when the vascular network is very dense.

4.7 Discussion

In this chapter, we have discussed the appearance of black artefacts in ASAP images. We have shown that such artefacts, caused by negative correlation, are a common problem in many correlation based methods such as First lag autocorrelation [41]. In

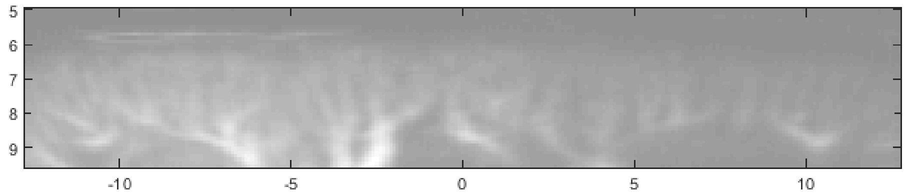

(a) Power Doppler

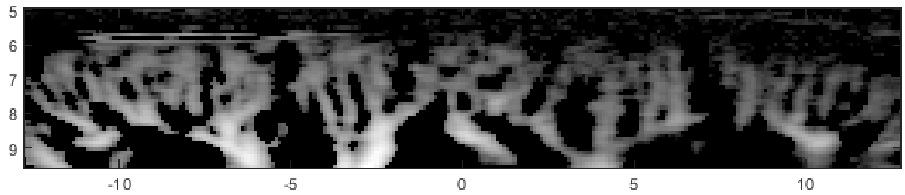

(b) ASAP

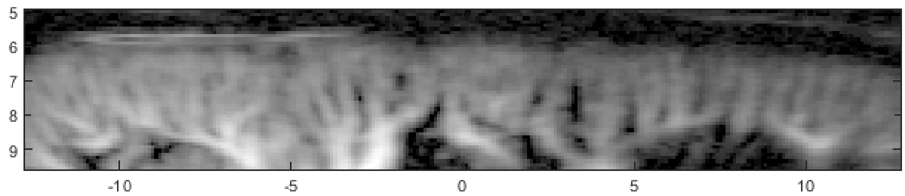

(c) Fast MV ASAP

Figure 4.15: Ultrasound images made on a rabbit kidney using PD (a), standard ASAP using channels paired as in Chapter 3 and the proposed fast method. Dynamic range is 35 dB and axis are in millimetres.

general, those effects result from the presence of strong scatting regions such as big vessels and can potentially mask signals that are located in the same spatial position as the artefacts. We have used simulations based on the autocorrelation function associated to moving microbubbles to evaluate how such negative correlations arise for different scatter velocities and number of compounding angles, and found that the effect on ASAP are constant for different imaging scenarios, while are highly variable for Lag1.

We have studied in detail how this effect arises for ASAP and shown that, in practice, this is given by an overestimation of the noise power in which also the contribution of interferences is included.

For such reasons, we proposed two different ways of removing noise from US images. The first one is derived from the MV beamforming theory. This image reconstruction technique has drawn much interest in the context of HFR US, and in particular during the writing of this thesis a new work has been published, in which the ability of MV beamforming of resolving closely spaced scatterers and microbubbles has been studied in detail [114]. We have modified the standard Capon beamforming in order to work with two different orthogonal apertures, obtaining a minimization problem which can be solved using alternating optimization for each of the apertures of the pair. Simulation results have shown that the proposed approach outperforms both MV beamforming and DAS in terms of noise rejection, and behaves comparably to MV beamforming in terms of mainlobe resolution. Compared with ASAP, the proposed approach is able to largely mitigate the appearance of negative correlations, thanks to the minimum variance criteria.

It has also been found that the diagonal loading defines a trade-off between sharpness of the mainlobe and noise rejection, acting as a user tunable parameter depending on whether more importance is given to image resolution or to noise floor reduction. Another important factor that requires further studies is the effect of the number of transmission in the estimation of the cross correlation matrix, which is important when imaging fast moving organ such as the heart, for which it is not possible to use a large number of frames for building a single image. In this regard, other variants of the MV approach, such as the Frost beamformer [115], the generalized sidelobe canceller [116] or the mid-way approach based on the Pisarenko framework [117], should be evaluated both in presence of contrast agents and without it.

Lastly, even if the alternating minimization is often capable of reaching local minima that are very close to the global one, the initialization of the aperture pair may have an important role in the quality of the converged result: while we have only performed random initialization, other methods of initializing the apertures, such as split apertures, should be evaluated. The optimization method itself may also be confronted with other minimization approaches, such as stochastic gradient descent, which has been shown to be often capable of escaping local minima thanks to its random behaviour [118].

We have also observed that the in-vitro data show a spatially varying noise floor, with increased noise level on the region above the mainlobe, for MV ASAP. This suggest that either the noise reduction ability or the convergence of the minimization criteria are affected by the structure of the covariance matrix, according to whether interferences are present. Further studies must be carried on such issues to evaluate the properties of the minimized function. Another possibility is that, in regions of pure noise, the minimization converges to a region where the negative correlation component is much weaker than the positive one, mitigating noise reduction. For this reason, MV ASAP seems better suited as an alternative to standard MV beamforming for noisy scenarios, as it reduces the FWHM and noise floor compared to standard MV approaches. Another way to mitigate such effect would be given by minimizing some measure of gaussianity of the data rather than variance, assuming that interference signals don't follow a Gaussian distribution while instead noise does.

With that in mind, and to ease the computational burden required by the minimization step, the second noise reduction method that we have proposed uses the sparsity of the spatial Fourier transform of the array to distinguish between echoes and noise power. It has been shown that the fast method is capable of a noise reduction comparable to the other correlation techniques. The assumption that the Fourier spectrum is sparse has been tested using in-vivo data where a dense vascular network is present, using uncompounded scans: even in this scenario, the Fast MV ASAP method showed reduced black artefacts and similar noise reduction compared to ASAP. Further studies must however be made in-vitro, with more complex phantoms, and in-vivo to validate whether the fast method always gives a satisfactory result.

Furthermore, we noted that using the minimum entry on the spatial power spectrum as noise estimate slightly underestimated its power, and therefore results in a reduced noise rejection compared to the other two methods. This proves the importance of correctly estimating the noise floor for enhancing the SNR and, as consequence, calls for improved ways of evaluating such estimate.

Lastly, the proposed method can also be potentially implemented in real time, as the spatial power spectrum of the array can be easily computed in parallel by multiplying the result of DAS delay stage by the Fourier matrix and taking the power estimate for each resulting channel. The noise estimate can also be used to adjust the Doppler spectrum of each pixel and obtain a better estimate of the mean frequency.

Chapter 5

Cross correlation tensor decomposition

In the recent years, the widespread use of ultrafast ultrasound in research made possible to gather CEUS scans with a large density of data per second. The large amount of information calls for statistical methods capable of performing more robust image reconstructions and processing. Emblematic of this is the use of second order spatio-temporal statistics, that is variance, with SVD, to clutter filter beamformed images prior to PD estimation [72, 106], which greatly improved HFR CEUS sensitivity and specificity to small vessels.

Other methods based on second order statistics have been developed, such as our ASAP [119, 112], lagged pixel second [41] or fourth [120] order statistics, cross channels correlation [53, 109, 108] or Short Lag Spatial Coherence Factor [56, 121].

By reviewing such methods, one can easily convince him/herself they are all based on the covariance estimation of some quantities which are assumed to be correlated, combining them using certain criteria and use the result for display or as a weight for other processing methods. It is also easy to see that they operate the correlation over different domains or dimensions, such as channels over slow time for ASAP or over fast time for SLSC, slow time at different lags for lag-τ techniques, different spatial locations for spatial ASAP, etc. It must be further noted how such different techniques aim at removing different kind of artefacts, like uncorrelated noise or interference signals, by assuming different underlying models for the system under examination

To encompass them into a single framework, the presence of different domains of correlation naturally calls for a tensorial, or multi-way, generalization of cross correlation methods for HFR US imaging.

In this chapter, we will start by building up an intuition of why tensors are a good model to describe and understand the different correlation methods, and how weighted tensorial decomposition is useful in this regard. We'll then use the gathered intuition to combine the different methods, and highlight how the extra degrees of freedom allowed by such tensorial model permits to construct more complex and robust processing methods, which can encompass richer and more expressive prior information models for processing. While we believe that this is an interesting way of processing ultrasound that helps exploit the rich structure given in HFR US data, further studies are needed to evaluate the effective performances and limitations of each derived technique.

5.1 Cross correlation tensor

In [37], the authors show that for slow to moderate flow, microbubble signals are coherent for tens of transmissions. This motivates the use of lagged autocorrelations to image small vessels [41]. Instead of the Power Doppler, which is the 0-lag autocovariance, higher lags $\tau > 0$ are evaluated using

$$PD_\tau = \frac{1}{N_f - 1} \sum_f \mathbf{a}^{\mathsf{H}} \mathbf{x}(f) \mathbf{x}^{\mathsf{H}}(f + \tau) \mathbf{a} = \mathbf{a}^{\mathsf{H}} \mathbf{R}_\tau \mathbf{a}, \tag{5.1}$$

where $\mathbf{R}_\tau$ is the τ-lag cross covariance matrix. The idea reduces to the same one as Power Doppler, but using $\mathbf{R}_\tau$ as an estimate of the noiseless $\mathbf{R}$. We therefore use the term *lag-τ PD* for such kind of estimation.

Note, once more, that while $\mathbf{R}_0$ is a positive semidefinite matrix that ensures that the result of PD estimation is a positive real number, $\mathbf{R}_\tau$ is a generic matrix that need not be positive definite nor Hermitian. This means that the lagged PD estimate can in principle be any complex number. In particular, signals that have a negative lag-τ autocorrelation will contribute negatively to the final estimate: those signals could arise, for example, from very fast moving flow or the rotation of side-lobe signals in a unfocused acquisitions with linear angle scanning [94], as shown in Chapter 4.

Leaving aside the effects on the PSF rotation caused by different steering angles, for example assuming that coherent compounding is performed before processing or that a single transmission angle is transmitted. Further assuming that the signals from each one of the sources are statistically independent, then eq. (4.11) is fulfilled at each lag, giving

$$\mathbf{R}_\tau = a(\tau) \cdot \mathbf{a}\mathbf{a}^{\mathsf{H}} + \sum_i \sigma_i(\tau) \cdot \mathbf{e}_i \mathbf{e}_i^{\mathsf{H}} + \delta(\tau)\sigma_n \mathbf{I}, \tag{5.2}$$

where the $\delta(\tau)$ term is used to restrict the noise contribution only to $\mathbf{R}_0$.

This model naturally leads to a tensor or multi-way description. By stacking together different $\mathbf{R}_\tau$ matrices over a third dimension, the 3-way tensor $\mathbf{R}_{i,j,\tau}$ is obtained, where the dimensions are (channels, channels, lags).

In tensor notation, the above model is

$$\mathbf{R}_{i,j,\tau} = a_\tau \mathbf{a}_i \mathbf{a}_j^{\mathsf{H}} + \sum_\lambda \sigma_{\lambda,\tau} \mathbf{e}_{\lambda,i} \mathbf{e}_{\lambda,j}^{\mathsf{H}} + \delta(\tau)\sigma \mathbf{I}. \tag{5.3}$$

To unify the notation, we stop distinguishing between signal of interest and interferences, by posing $\sigma_{0\tau} = a_\tau$:

$$\mathbf{R}_{ij\tau} = \sum_\lambda \sigma_{\lambda\tau} \mathbf{e}_{\lambda i} \mathbf{e}_{\lambda j}^{\mathsf{H}} + \delta(\tau)\sigma \mathbf{I}. \tag{5.4}$$

Excluding the noise term, this is exactly the canonical polyadic decomposition (CPD) of a 3-mode tensor [122], which is given by

$$\mathbf{R}_{ijk} = \sum_\lambda \mathbf{A}_{\lambda i} \mathbf{B}_{\lambda j} \mathbf{C}_{\lambda k}. \tag{5.5}$$

This model can be further expanded by considering each compounding angle separately, constructing a 5-way tensor where the two additional indexes α and β refer to two different transmissions. The tensor will therefore look like

$$\mathbf{R}_{ij\alpha\beta\tau} = \frac{1}{F} \sum_f x_{i\alpha}(f) x_{j\beta}(f+\tau)^*, \tag{5.6}$$

where $x_{i\alpha}(f)$ refers to the signal recorded by the i-th element at the compounding angle α of the frame f.

Following the same logic, one could increase the order of the tensor to include correlations between different pixels [112] or different time lags [56]. We now show a few application of the tensorial framework to highlight the increased degree of freedom and understanding of the processing methods that it provides.

5.2 Applications of the tensorial framework

5.2.1 Tensor decomposition and coherence approaches

From the previous section, it is not obvious how different correlation methods can be described using the given formalism, as no reconstruction of the cross correlation matrix is involved. However, this is an effect arising from the simplicity of the correlation methods, which on the other hand has the advantage of speeding up the computation. We now review how those techniques can all be described by the following steps:

1. Decompose the cross correlation tensor using a model that contains a mixture of fixed and free variables.
2. Perform an estimate on the decomposed model.

While doing so, we also propose some generalized methods inspired from them.

Lagged cross correlation and ASAP

Calling $\mathbf{a}$ the steering vector, we assume that $\mathbf{R}_{ij\tau}$ has the following structure

$$\hat{\mathbf{R}}_{ijk} = \delta_\tau \sigma_\tau \mathbf{a}\mathbf{a}^{\mathsf{H}} + \mathbf{N}_{i,j,k}, \tag{5.7}$$

where $\mathbf{N}_{i,j,\tau}$ is Gaussian zero-mean noise. In such scenario, the optimal way (in the leasts-squares sense) of estimating the noiseless tensor is given by minimizing the function

$$J = \frac{1}{2} \left\| \mathbf{R}_{ijk} - \delta_\tau \sigma_\tau \mathbf{a}\mathbf{a}^{\mathsf{H}} \right\|_{\mathrm{F}}^2 . \tag{5.8}$$

Because the assumed structure gives a null matrix for every $k \neq \tau$, minimizing the above function is equivalent to minimizing

$$J = \frac{1}{2} \left\| \mathbf{R}_{ijk}|_{k=\tau} - \sigma_\tau \mathbf{a}\mathbf{a}^{\mathsf{H}} \right\|_{\mathrm{F}}^2 = \frac{1}{2} \left\| \mathbf{R}_\tau - \sigma_\tau \mathbf{a}\mathbf{a}^{\mathsf{H}} \right\|_{\mathrm{F}}^2 . \tag{5.9}$$

Taking the gradient with respect to σ_τ and setting it to zero gives the solution

$$\sigma_\tau = \mathbf{a}^{\mathsf{H}} \mathbf{R}_\tau \mathbf{a}. \tag{5.10}$$

The value of σ_τ coincides with the lag-τ estimate p as, in fact, estimating the value in the direction $\mathbf{a}$ from the reconstructed cross correlation matrix is trivially

$$p = \mathbf{a}^{\mathsf{H}}\hat{\mathbf{R}}_{\tau}\mathbf{a} = \sigma_{\tau}\mathbf{a}^{\mathsf{H}}\mathbf{a}\mathbf{a}^{\mathsf{H}}\mathbf{a} = \sigma_{\tau}. \tag{5.11}$$

Therefore lagged cross correlation estimation is assuming a model as in eq. (5.7). Setting $\tau = 0$ we get the classic PD estimate.

For the case of ASAP, the model is changed as

$$\hat{\mathbf{R}}_{i,j,\tau} = \delta_{\tau}\sigma_{\tau}\mathbf{a}\mathbf{a}^{\mathsf{H}} + \sigma_n\delta_{\tau}\mathbf{I}_{i,j} + \mathbf{N}_{i,j,\tau}, \tag{5.12}$$

whose optimal estimate is given, for example, by decomposing the tensor as

$$\hat{\mathbf{R}}_{ijk} = \delta_{\tau=0}\sigma_0\mathbf{w}_1\mathbf{w}_2^{\mathsf{H}}, \tag{5.13}$$

where $\mathbf{w}_1$ and $\mathbf{w}_2$ are the two orthogonal apertures. Using the same arguments as above, we get back the same result, that is the ASAP estimate is equal to σ_0, but it removes asymptotically the noise contribution.

Mixed lag model

If we want to extend the previous model to include multiple lags, we can generalize it by removing the delta function

$$\hat{\mathbf{R}}_{\tau} = \sigma_{\tau}\mathbf{a}\mathbf{a}^{\mathsf{H}}. \tag{5.14}$$

Now according to the way we allow the σ_{τ} to change and depending on how we process it to get the estimate p, the results we obtain are different.

For example, if we let σ_{τ} vary with τ and then we average its value, we are simply taking as power estimate the average value of different lag-τ estimate: we are implicitly assuming that $\sigma_{\tau} = const$ and any deviations from such constant value are given by noise, which we filter out when we average.

This boils down to solving the following minimization problem

$$J = \frac{1}{2}\left\|\mathbf{R}_{\tau} - \sigma_{\tau}\mathbf{a}\mathbf{a}^{\mathsf{H}}\ \right\|_{\mathrm{F}}^{2} = \frac{1}{2}\sum_{i,j,\tau}\|R_{ij\tau} - \sigma_{\tau}\mathbf{a}_i\mathbf{a}_j^{\mathsf{H}}\|^2 \tag{5.15}$$

To remove the noise contribution, we could instead not include the diagonal entries of the first lag cross correlation matrix from the minimization function. This can be easily done by modifying the cost function J such that the entries of R_{ijk} for which $i = j$ and $\tau = 0$ are not included in its computation, for example by changing J to

$$J' = \frac{1}{2} \sum_{i,j,\tau} M_{i,j,\tau} \| R_{i,j,\tau} - \sigma_\tau \mathbf{a}_i \mathbf{a}_j^{\mathsf{H}} \|^2, \tag{5.16}$$

where $M_{i,j,k}$ is a mask function such that

$$M_{i,j,k} = \begin{cases} 0 & i = j, \ \tau = 0 \\ 1 & \text{otherwise.} \end{cases} \tag{5.17}$$

Excluding the zero-lag cross correlation matrix diagonal from the computation of the cost function, is equivalent to use a generalized ASAP matrix $\mathbf{A}$ for the zero lag estimate

$$\mathbf{A} = \mathbf{a}\mathbf{a}^{\mathsf{H}} - \mathrm{diag}(\mathbf{a}\mathbf{a}^{\mathsf{H}}), \tag{5.18}$$

where $\mathrm{diag}(\mathbf{M})$ is a diagonal matrix whose diagonal entries are given by M_{ii} and the off-diagonal entries are null

$$\mathrm{diag}(M)_{ij} = \begin{cases} M_{ij} & i = j \\ 0 & i \neq j. \end{cases} \tag{5.19}$$

Removing the signal independence constraint

In the considerations made so far, we are assuming that the steering vectors for each scatterer are constant for all the samples and that the signals are independent.

However, this is a very strong assumption that doesn't hold for at least two reasons. First of all, when different steering vectors are used only the Direction of arrival (DOA) coming from the beamformed position is approximately constant across different samples, while the rotation of the PSF changes the steering vector associated with even the same interference scatter at different frames, creating mixed correlations at all lags. Secondly, the received echoes are all the result of scattering the same waveform, so the response of scatterers from different spatial locations may exhibit correlations.

To build up a model that can take into account such differences we start by considering a single scatterer. If it is placed in the spatial location where we are beamforming, we can assume that the steering vector associated is constant for all different lags, as previously done. However, if it is an off axis target, the use of different transmission angles changes its direction of arrival, which is the reason why coherent compounding improves contrast when imaging stationary scatterers.

Therefore, we define $\mathbf{e}_{i,\alpha}$ the steering vector associated with the scatter when we are transmitting at angle α. The single scatter cross correlation model is given by

$$\mathbf{R}_{ij\tau} = \sum_{\alpha} \sigma_{\alpha,\alpha+\tau,\alpha} \mathbf{e}_{\alpha} \mathbf{e}_{\alpha+\tau}^{\mathsf{H}}. \tag{5.20}$$

Assuming that N_α angles are transmitted, an easier way to visualize this is to focus on a single time lag τ and write it as a matrix product

$$\mathbf{R}_{\tau} = \mathbf{E}\mathbf{S}_{\tau}\mathbf{E}^{\mathsf{H}}, \tag{5.21}$$

where

$$\mathbf{E} = \begin{pmatrix} e_{1,1} & e_{1,2} & \dots & e_{1,N_\alpha} \\ e_{2,1} & e_{2,2} & \dots & e_{2,N_\alpha} \\ & \vdots & & \end{pmatrix}, \qquad S_\tau = \begin{pmatrix} \sigma_{1,1,\tau} & \sigma_{1,2,\tau} & \dots & \sigma_{1,N_\alpha,\tau} \\ \sigma_{2,1,\tau} & \sigma_{2,2,\tau} & \dots & \sigma_{2,N_\alpha,\tau} \\ & & \vdots & \\ \sigma_{N_\alpha,1,\tau} & \sigma_{N_\alpha,2,\tau} & \dots & \sigma_{N_\alpha,N_\alpha,\tau} \end{pmatrix},. \tag{5.22}$$

The matrix $\mathbf{E}$, constant for all the different lags, is the matrix containing the steering vectors associated to different transmit angles, while $\mathbf{S}_\tau$ is the square matrix containing the cross correlation phase and amplitude for each possible pair of steering vectors, and varies with the lag. Thanks to this last matrix, we can model cross correlation for different steering vectors, as happens for the case of transmitting multiple unfocused waves. We stress that the matrix containing the steering vectors is the same for the different lags. In fact such a model is analogous to a Tucker decomposition, with Hermitian transpose symmetry on the first two modes matrices [122].

When multiple scatters are present, their scattered signals will also be partially correlated, since they generate in response to waves having the same frequency content. To include multiple scatters, we just have to extend the matrix $\mathbf{E}$ by adding more columns. The matrix $\mathbf{S}$ will then model the cross correlation of both steering vectors associated with different scatters for different transmissions, or of different scatters.

Such a model comes with a large number of parameters, which can easily be more than the original Cross correlation (CC) tensor, especially if the core tensor $\mathbf{S}$ is large. While regularization is a powerful approach to solve this issue [123], with the potentiality to introduce other information on the model such as sparsity, but we will instead just reduce the size of the core tensor. We however impose that the columns of this matrix are orthonormal between themself, as it appears to speed up the estimation of the core tensor.

It would be possible to just use this decomposition to estimate a noiseless version of the CC tensor, but instead we can use the ideas developed in the previous sections to highlight the variety of filtering methods allowed by the tensor formulation.

The idea is to include our known *a-priori* information regarding the DOA steering vector $\mathbf{a}$ and impose that one of the factors of the matrix $\mathbf{E}$ coincides with a. This can be easily done by appending in front of such matrix a column equal to $\mathbf{a}$, that is

$$\hat{\mathbf{E}} = (\mathbf{E}\mathbf{a}) = \begin{pmatrix} a_1 & e_{1,1} & e_{1,2} & \dots & e_{1,N_\alpha} \\ a_2 & e_{2,1} & e_{2,2} & \dots & e_{2,N_\alpha} \\ & \vdots & & & \end{pmatrix}. \tag{5.23}$$

While we train our model, we will take care not to update such column in order to keep equal to $\mathbf{a}$.

After convergence, the PD value associated to the spatial location of interest is estimated by the factor S_{110} corresponding to the first element of the matrix $\mathbf{S}$. In Matlab notation, that is $S(1,1,1)$, since the vector $\mathbf{a}$ has got unit norm, therefore

$$p = S_{110}. \tag{5.24}$$

We name this method Multilinear Power Doppler Estimation (MPDE).

5.2.2 In-vivo acquisitions

The aim of the proposed methods, such as MPDE, is to improve the image quality in challenging situations. For such reason, it has been tested on HFR CEUS scans of the left ventricular cardiac chamber, performed on a healthy volunteer by Dr. Matthieu Toulemonde [76].

This dataset has been chosen as it offers a challenging opportunity for beamforming, because of quite a few reasons: it is imaged using a relatively small phased array using diverging waves, which are characterized by a low MI compared to plane waves, the field of view is large and deep, thus reducing the frame rate and increasing the amount of information packed in the RF data, there are large motions that prevent the use of many samples to evaluate cross correlations and make coherent compounding ineffective, the large amount of contrast agent and small aperture size create very large and widely spreads side and grating lobes, that can easily mask weak signals of interest such as the perfusion information of the myocardium.

The acquisition is performed using a 3 cycle Gaussian pulse shaped wave, with a central frequency of 1.5MHz, transmitted as a diverging wave using the virtual source synthetic aperture method [124]. Pulse inversion imaging is used with 11 compounded angles, for a total of 22 transmissions per frame. The number of frames used to estimate the cross correlation matrix is 7, giving a total of 77 time samples for each matrix estimation. The cross correlation tensor is constructed up to lag 5.

The methods evaluated are lag-0 (Power Doppler), noiseless lag-0 using the matrix $\mathbf{A}$, lag-1, tensorial generalization for the cross correlation methods using tensor (ASAP + Lag-τ + SLSC) and MPDE.

Results

The results of the processing is shown in Fig. 5.1. In the PD image, we see the presence of large sidelobe and background noise that make difficult the quantification of small signal in the myocardial area. Using Lag-1 cross correlation, we see that the noise floor is largely reduced, but the negative correlations due to the fast flow in the chamber create black artefacts. Furthermore, the interference reduction in the area of the cardiac muscle seems unsatisfactory.

Using ASAP with the generalized matrix of eq. (5.18) produces a cleaner image with reduced artefacts, but still shows very dark regions in the myocardium due to negative correlations. The approach generalizing cross correlation methods gives some improvements with respect to ASAP, while suffering from artefacts in the chamber arising from averaging positive and negative correlations due to fast flow.

The result of the MPDE tensorial decomposition, shows instead a very low amount of artefacts, in terms of side and grating lobes strength, negative correlations and masking of the myocardial segments. It also shows a very smooth flow pattern in the chamber while providing great definition of the cardiac walls.

5.2.3 Asap over compounding angles

As a second example of use of the tensorial framework, we extend the cross correlation tensor to include different angles. In this case, the data received by the array is

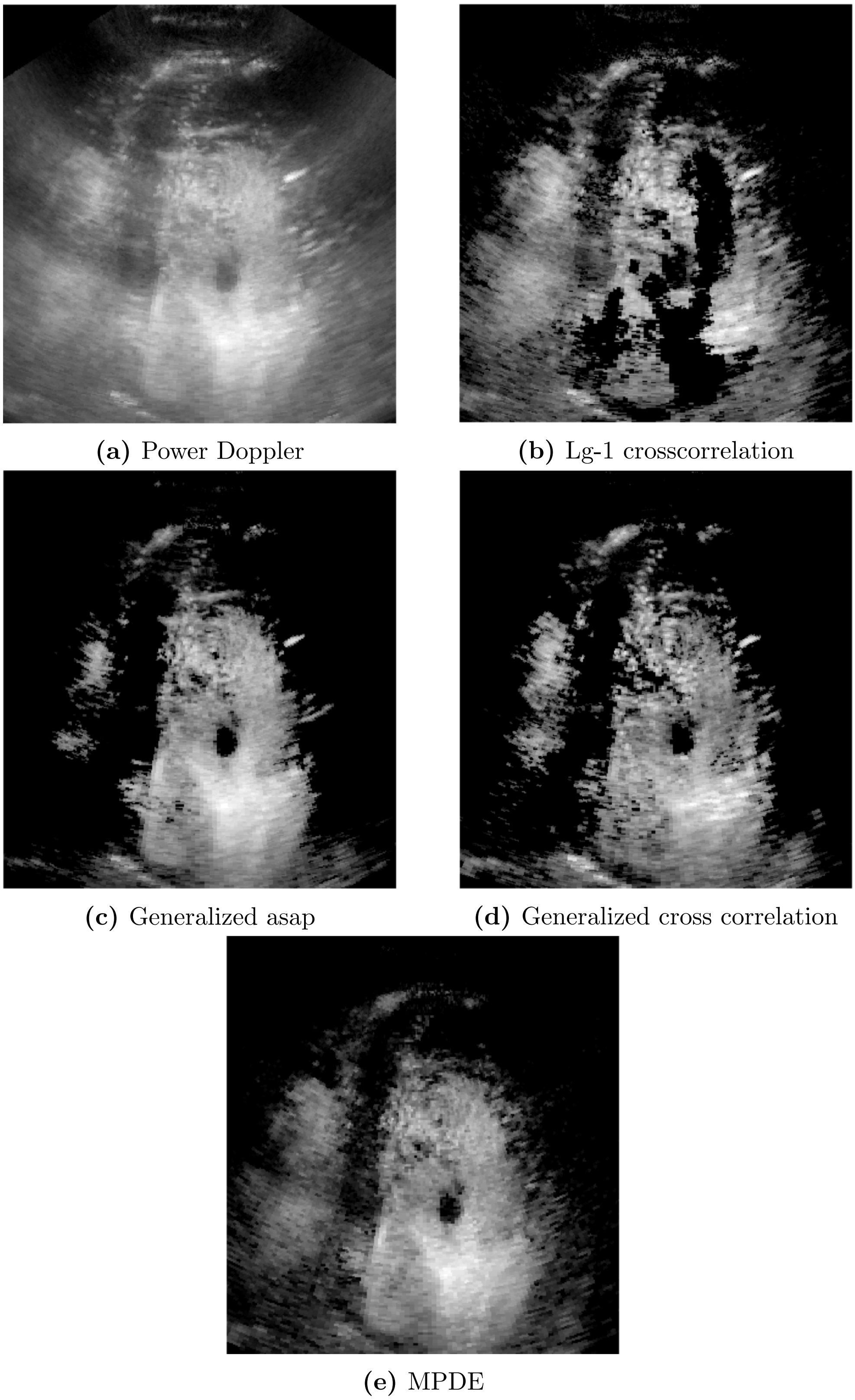

Figure 5.1: Cardiac imaging using different second order statistical methods. Negative correlations are set to zero, dynamic range is 35dB.

indexed with three numbers: channel, time and compounding angle, and can be seen as a sequence of matrices $\mathbf{x}_{i,\alpha}(t)$, where Latin letters indicate channels and Greek letters indicate compounding angles. When we perform ASAP after compounding, we are implicitly adding all the columns of the input matrix to get the channel vectorial inputs

$$\mathbf{x}_c = \sum_{\alpha} b_\alpha \mathbf{x}_{c,\alpha} = \mathbf{x}_{c,\alpha}\mathbf{b}, \tag{5.25}$$

where $\mathbf{b} = (b_1, b_2, b_3, \dots)^{\mathsf{H}}$ is the vector given by the weights associated to each compounding angle during the sum. This vector can be also regarded as a kind of *apodization* applied in the angles domain, to be compared with the usual apodization applied on the channel domain.

This symmetry suggests that ASAP can also by applied to the compounding angles after summing all the elements, rather than to the channels after summing the angles. The assumption now is not that noise must be uncorrelated across channels, but rather that noise in different frames is uncorrelated while the contrast agent signal is: the weight vector $\mathbf{b}$ represents our assumption about the interframe correlation.We call this method *anglewise ASAP* and works identically to the ASAP technique as described in the previous chapter, except for the dimensions in which it is applied.

The cross correlation tensor has now reduced dimensions, that is $N_\alpha \times N_\alpha$ where N_α is the number of compounding angles used. We can find pair of orthogonal apertures using any of the methods described in the previous chapters: in this case, we will use Fast MV ASAP, as described in Chapter 4.

Results

The point spread function resulting from the proposed method is shown in Fig. 5.2. We see that, compared to the classical way of performing ASAP, the proposed method slightly underperforms noise rejection by a factor of 2dB, but still reaches a 6dB reduction of noise level compared to PD. The effect of noise reduction and sidelobe intensity has been quantified in Fig. 5.3, where we see that the proposed technique largely reduces the intensity in the interference regions compared to ASAP.

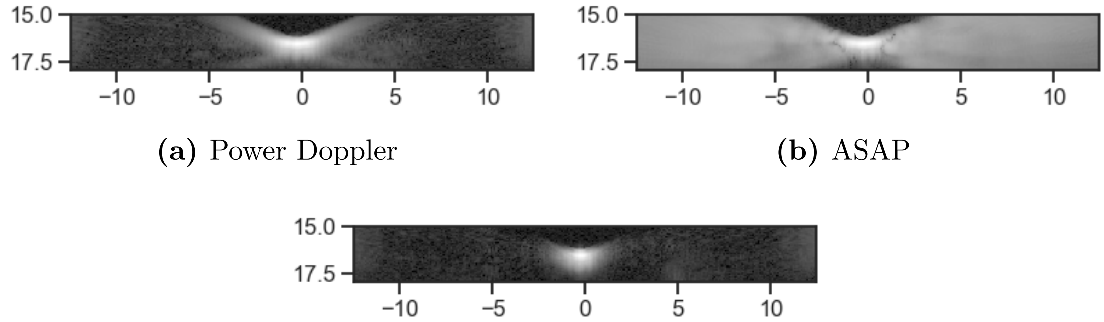

(a) Power Doppler **(b)** ASAP

(c) Minimum variance ASAP over angles

Figure 5.2: Point spread function made by a cross section of a wire with flowing microbubbles with different processing methods. Dynamic range is 60dB

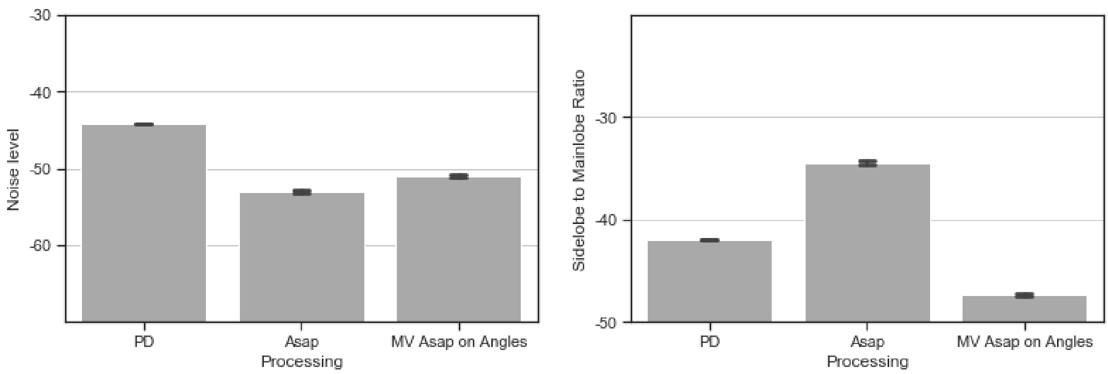

(a) Noise intensity **(b)** Sidelobe intensity

Figure 5.3: Normalized noise power and sidelobe to mainlobe level for the different second order statistical methods.

5.2.4 Tensor generalization of minimum variance beamforming

We now use again the 5-way tensor that includes both the different compounding angles and the different channels correlations

$$\mathbf{R}_{i,j,\alpha,\beta,\tau} = \sum_{f} \mathbf{x}_{i,\alpha}(f)\mathbf{x}_{j,\beta}(f+\tau). \tag{5.26}$$

Many methods devised for a single domain can now be generalized to multiple domains using the tensorial method. For example, in [50] the authors used minimum variance beamforming sequentially on channel and then on transmission domain, in a method they call Transmit-Receive (Tx-Rx) MV beamforming. To do so, we need to define two constraint on the apodization vector $\mathbf{w}$ and on the transmission

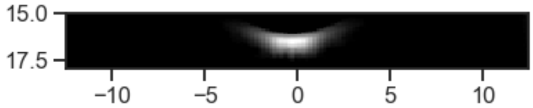

(a) Power Doppler

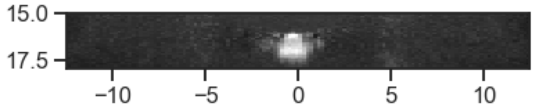

(b) Tx-Rx Minimum variance

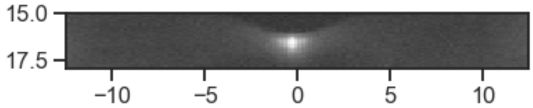

(c) Tensorial minimum variance

Figure 5.4: Point spread function made by a cross section of a wire with flowing microbubbles with different processing methods. Dynamic range is 30dB.

weights vector $\mathbf{w}_\alpha$: the first one is the usual unit gain response to the direction of interest $\mathbf{a}$, given by setting $\mathbf{w}^{\mathsf{H}}\mathbf{a} = 1$, an the the other one is the unit response of the transmission weight vector to the standard weight vector $\mathbf{q}$ (see Sec. 1.2.4), that is $\mathbf{w}_\alpha \mathbf{q} = 1$. Using tensors, instead, we can perform such processing contemporary on both the channel and transmit domain by substituting the cross correlation matrix with the cross correlation tensor and the two linear constraints with a single one, namely

$$\sum_{i,j} W_{ij} A^*_{ij} = 1, \tag{5.27}$$

where A_{ij} is the steering matrix, given by

$$\mathbf{A} = \mathbf{a}\mathbf{q}^{\mathsf{H}} \qquad \rightarrow \qquad A_{i,j} = a_i q_j, \tag{5.28}$$

and W_{ij} is the matrix that generalizes the minimum variance apodization in the channel-transmit domain. The minimization problem then becomes

$$\mathbf{W} = \min_{\mathbf{W}} \sum_{i,j,\alpha,\beta} W^*_{i,\alpha} \mathbf{R}_{i,j,\alpha,\beta} . W_{j,\beta} \tag{5.29}$$

Results

The results of applying both the Tx-Rx minimum variance approach and the tensorial generalization of the minimum variance method are given in Fig. 5.4, where for both methods a diagonal loading factor of 0.001 has been used (see eq. (4.28) for our definition of diagonal loading factor). Comparing the two methods, we see that the tensorial generalization achieves a sharper estimate of the PSF while at the same time maintains the axial resolution of the PD image. Also, the proposed approach seems to give a more reasonable shape of the PSF mainlobe compared to the Tx-Rx method. However, the SNR of the minimum variance methods increases from 31.4dB of the PD image, to 24.4dB of the Tx-Rx approach and 21.5dB of the proposed method: this shows that our approach may be more sensitive to mismatches of the steering vector, therefore more studies must be done to on how to regularize the CC matrix before estimating the MV aperture.

5.3 Discussion

In this chapter, we have described how the intuitive idea that different correlation methods are performing very similar operations in slightly different domain, can be expressed mathematically using the language of tensors and associated operations. By extending the cross correlation matrix to a cross correlation tensor, then most of the approach currently available in the literature can be unified in a single framework; furthermore, they can be easily combined into mixed methods.

We have shown how many processing methods can be seen as the result of a tensor decomposition and an estimation on the reconstructed tensor, which allowed us to merge different correlation-based methods into a single generalized correlation approach, for which preliminary result suggest improved performances. Further than that, using more complex decomposition techniques it is possible to drop the crude assumption of uncorrelated sources often made when designing statistical estimators for ultrasound imaging, increasing the image quality even in difficult settings such as contrast enhanced cardiac imaging.

The multi-way approach also make easy to understand how to extend many techniques based on linear algebra into their multi-linear counterparts: we gave two examples by extending our ASAP method to work in transmission domain, rather than in channels, and by constructing a multilinear version of the Capon beamformer, which we compared with a state of the art technique.

Another interesting line of research that the tensorial formulations highlights is given by Independent Component Analysis techniques for blind source separation. For example, assuming that the recorded echoes present different power spectra, one could exploit simultaneous diagonalization of the covariance matrices at different time lags as done in AMUSE [125] to separate signals generated in different spatial locations. Another possibility is also given by considering that contrast enhanced ultrasound signals are produced by non stationary processes and, therefore, have time varying high order statistics that can be used for source separation [126].

The results shown in this chapter are promising, but are however only preliminary due to the time constraint of the PhD study period. To fully exploit the power of multilinear signal processing, it is necessary to gain a better understanding of the statistical properties of US data when viewed as a multidimensional array. Based on this, robust methods have to be designed and tested in various kind of controlled settings, in order to quantitatively and qualitatively evaluate the strength and weaknesses of each approach.

Chapter 6

Summary and conclusions

In this thesis, we have studied how the introduction of contrast agents and HFR US has changed the possibilities of imaging vascular and cardiac flow dynamics and anatomy.

In Chapter 2, after reviewing the main principle ultrasound imaging and contrast acquisitions, we give the first cotribution by studying the *effect of motion* on contrast enhanced images in the case where large motions are present. This work started by the observation of intensity reductions in contrast enhanced images of the heart. As such artefacts were associated with large flows velocity of some phases of the cardiac cycle, we formulated the hypothesis that they are due to motion during the compounding stage. To verify such idea, we began by performing *simulations* using a realistic model of micrububble under different scanning conditions.

The results have shown that the shape of the PSF associated with microbubbles is largely modified by the presence of motion, especially in the axial direction, which generates large variations of the point spread functiom. Furthermore, both the peak intensity and the average intensity of the microbubble signal is *largely reduced* as the velocity increases, up to 26dB and 16dB of reduction respectively, in accordance to our hypothesis and previous literature on contrast and non contrast imaging.

We also observe that such reduction, which is due to the coherent compounding operation, is very *dependent on both the position and the velocity* direction of the microbubbles, with up to 25dB reduction for the largest axial velocity, and worsen as more angles are employed to reconstruct a single image.

We have then shown how motion compensation is a valuable option for mitigating such effects and demonstrated improvements of both CNR and CANR in the LV chamber and miocardium, respectively by 1.2dB and 0.5dB, when a simple motion correction scheme is applied.

Motivated by those results, in Chapter 3 we have investigated the use of correlation to enhance vascular images without increases of computational complexity that could prevent their application in the clinical settings. To this end, we devised ASAP as a quick and powerful method to improve the SNR of standard and contrast-enhanced vascular images by exploiting the diagonal structure of the noise cross correlation matrix. By using two orthogonal apertures, we effectively *reject noise while preserving the mainlobe signal*, by exploiting the lack of correlation between noise of different channels. The results show up to 19dB of SNR improvement compared to PD for both in-vivo and in-vitro experiments.

The effect of interferences has also been evaluated and, noting the negative correlation of side and grating lobe signals, we proposed to filter out non positive value to perform *interference reduction*. To this end, we have also empirically studied several ways of defining the fixed orthogonal apertures to minimize the appearance of negative correlations in the images and, also, we have highlighted how filtering the slow-time signals of each aperture can give further insight on the vascular properties of the images, such as the flow direction.

The appearance of negative correlation in correlation methods and in particular the ASAP images, on the other hand, can negatively affect the ability to image small vessels located in the proximity of a large one.

In Chapter 4 we have studied this issue in detail from the image formation point of view and derived two main ways of interpreting the presence of negative correlations . From this, we have shown that ASAP is basically a noise estimation and subtraction method and that negative correlations are generated by an *overestimation of the noise floor*, in which also the power of interference scatterers contributes.

This lead to two different solutions. The first one is to use *adaptive methods* to estimate the pair of apertures. While simulation data show promising result, the in-vitro data indicate that this method may be better suited as a noise reduction method for MV beamforming.

The second way of estimating the noise power is derived from linear array theory. It uses the fact that, when a moderate number of scatterers is present, the delayed signal is *sparse in the spatial Fourier domain.* Such domain gives a convenient space in which noise can be estimate by extracting the lowest spectral power. While this slightly underestimates the noise level compared to ASAP or interframe correlation methods, it almost completely reduces the presence of negative correlation both in simulation, in vitro and in vivo studies. The proposed method is fast as it requires just the multiplication of two matrices whose size is equal to the number of channels, and can be parallelized.

Lastly, in Chapter 5, we proposed a *tensorial framework* that generalizes the most of the correlation methods that appear in ultrasound literature and provide a convenient mathematical structure for designing processing methods based on coherence. We have shown with example how some techniques based on second order statistics can be extended in different domains and, in general, explained how different correlation methods can be seen as simple decomposition techniques of a multy-way covariance tensor.

As an example, we have extended the ASAP method from the channel domain to the transmit domain, showing how noise reduction is substantially preserved while side lobes are largely reduced, even compared to standard PD. Similarly, we generalized MV beamforming to work both in the channel and in the transmission domain, showing improved robustness compared to modern transmit-receive MV approaches, albeit with a slight reduction of SNR. While the tensorial approach is a promising direction, for which we have shown preliminary results both in-vitro and in-vivo, further studies are however needed to evaluate the performances of the methods designed in such manner.

6.1 Future work

In the immediate future, more detailed in-vivo evaluation and quantification of the proposed methods must be performed. The convergence properties of the developed MV ASAP must be addressed, together the use of different cost function for estimating the optimal pair of apertures, and the method must be tested in-vivo. The Fast MV ASAP technique must as well be evaluated in a wider range of scenarios and the proposed noise estimation method should be also used to perform different kind of image reconstruction, for example by using it to reduce the velocity bias of velocity estimators that use the mean Doppler frequency, by removing noise from the Doppler power spectra.

In the longer term, the advantage of having large amount of data per single scan allows to use statistical priors during the reconstruction process and therefore design reconstruction methods that are optimal in some sense. Building on the findings of this thesis, future work should focus into understanding in greater details what are the statistical properties of contrast enhanced ultrasound vascular images.

Once the structure of ultrasound data is understood, one of the first task that could be addressed is to solve the problem of clutter rejection. Very recently, the sparsity of microbubble signals has been used to surpass the assumption of orthogonal components used for SVD clutter filtering, by constructing a low-rank + sparse core decomposition that is able to distinguish between large tissue signals and contrast agents [127]. The inherent sparsity of microbubbles could also be used in the reconstruction process itself, by modeling the scattering function as a collection of impulsive elements and casting the beamforming process as a global inverse problem, albeit one main difficult in such approach is given by the non linear response of microbubbles which make difficult a linear formulation. Such approach could be valuable for high frequency imaging, where the non linear response of microbubbles is negligible.

The use of decomposition methods has also been found valuable for image reconstruction. One important future step would be a more rigorous evaluation the derived methods we proposed. It would also be interesting to extend the tensorial framework to include different spatial location, so to incorporate the inherent spatio-temporal properties of microbubble flow in the image reconstruction process. An example of such approach would be given by modeling interframe displacement as a Markov process, since under the assumption of constant flow microbubble motion is just dependent on their spatial location.

Bibliography

[1] J. A. Jensen, "FIELD: A Program for Simulating Ultrasound Systems," *Medical and Biological Engineering and Computing*, vol. 34, no. SUPPL. 1, pp. 351–352, 1996.

[2] A. Stanziola, M. Toulemonde, Y. Yildiz, R. Eckersley, and M.-X. Tang, "Ultrasound imaging with microbubbles," *IEEE Signal Processing Magazine*, vol. 33, no. 2, 2016.

[3] J. Engelbrecht, "Wave equations in mechanics," *Estonian Journal of Engineering*, vol. 19, no. 4, p. 273, 2013. [Online]. Available: http://www.kirj.ee/?id=23355&tpl=1061&c_tpl=1064

[4] T. L. Szabo, *Diagnostic Ultrasound Imaging: Inside Out.* Academic Press, 2013. [Online]. Available: https://books.google.co.kr/books?id=wTYTAAAAQBAJ

[5] J. Bercoff, M. Tanter, and M. Fink, "Supersonic Shear Imaging : A New Technique," *IEEE Transactions on Ultrasonics, Ferroelectrics and Frequency Control*, vol. 51, no. 4, pp. 396–409, 2004.

[6] L. Demanet, "Waves and Imaging Class notes - 18.325," 2016. [Online]. Available: http://math.mit.edu/icg/resources/notes325.pdf

[7] J. Y. Lu, "2d and 3d High Frame Rate Imaging with Limited Diffraction Beams," *IEEE Transactions on Ultrasonics, Ferroelectrics, and Frequency Control*, vol. 44, no. 4, pp. 839–856, 1997.

[8] J. Cheng and J. Y. Lu, "Extended high-frame rate imaging method with limited-diffraction beams," *IEEE Transactions on Ultrasonics, Ferroelectrics, and Frequency Control*, vol. 53, no. 5, pp. 880–899, 2006.

[9] K. Watanabe, *Integral Transform Techniques for Green's Function.* Springer, 2014, vol. 71. [Online]. Available: http://link.springer.com/10.1007/978-3-319-00879-0

[10] G. S. Alberti, H. Ammari, F. Romero, and T. Wintz, "Mathematical analysis of ultrafast ultrasound imaging," *SIAM Journal on Applied Mathematics*, vol. 77, no. 1, pp. 1–25, 2017.

[11] J. A. Jensen, S. I. Nikolov, K. L. Gammelmark, and M. H. Pedersen, "Synthetic aperture ultrasound imaging," *Ultrasonics*, vol. 44, no. SUPPL., 2006.

[12] F. P. C. PINTO, "Signal Processing in Space and Time - A Multidimensional Fourier Approach [PhD Thesis]," *École Polytechnique Fédérale De Lausanne*, vol. 4871, 2010.

[13] M. E. Anderson and G. E. Trahey, "A seminar on k-space applied to medical ultrasound," *Department of Biomedical Engineering, Duke University*, 2000.

[14] B. D. Van Veen and K. M. Buckley, "Beamforming: A versatile approach to spatial filtering," *IEEE assp magazine*, vol. 5, no. 2, pp. 4–24, 1988.

[15] P. N. T. Wells, "Ultrasonic imaging of the human body," *Reports on Progress in Physics*, vol. 62, no. 5, pp. 671–722, 1999. [Online]. Available: http://stacks.iop.org/0034-4885/62/i=5/a=201?key=crossref.5491ff1d7ef665f8c859e1c1d18b3e11

[16] G. Montaldo, M. Tanter, J. Bercoff, N. Benech, and M. Fink, "Coherent plane-wave compounding for very high frame rate ultrasonography and transient elastography," *Ultrasonics, Ferroelectrics, and Frequency Control, IEEE Transactions on*, vol. 56, no. 3, pp. 489–506, 2009. [Online]. Available: http://ieeexplore.ieee.org/xpl/articleDetails.jsp?arnumber=4816058

[17] B. Denarie, T. A. Tangen, I. K. Ekroll, N. Rolim, H. Torp, T. Bjastad, and L. Lovstakken, "Coherent plane wave compounding for very high frame rate ultrasonography of rapidly moving targets," *IEEE Transactions on Medical Imaging*, vol. 32, no. 7, pp. 1265–1276, 2013.

[18] M. Cikes, L. Tong, G. R. Sutherland, and J. D'Hooge, "Ultrafast cardiac ultrasound imaging: Technical principles, applications, and clinical benefits," *JACC: Cardiovascular Imaging*, vol. 7, no. 8, pp. 812–823, 2014.

[19] L. E. Kinsler, A. R. Frey, A. B. Coppens, and J. V. Sanders, "Fundamentals of acoustics," *Fundamentals of Acoustics, 4th Edition, by Lawrence E. Kinsler, Austin R. Frey, Alan B. Coppens, James V. Sanders, pp. 560. ISBN 0-471-84789-5. Wiley-VCH, December 1999.*, p. 560, 1999.

[20] M. F. Schiffner, "Random Incident Sound Waves for Fast Compressed Pulse-Echo Ultrasound Imaging," *arXiv:1801.00205 [physics]*, Dec. 2017, arXiv: 1801.00205. [Online]. Available: http://arxiv.org/abs/1801.00205

[21] P. Kruizinga, F. Mastik, N. de Jong, A. F. W. van der Steen, and G. van Soest, "Plane-wave ultrasound beamforming using a nonuniform fast fourier transform," *IEEE Transactions on Ultrasonics, Ferroelectrics*

and Frequency Control, vol. 59, no. 12, Dec. 2012. [Online]. Available: http://ieeexplore.ieee.org/document/6373791/

[22] D. Garcia, L. L. Tarnec, S. Muth, E. Montagnon, J. Poree, and G. Cloutier, "Stolt's f-k migration for plane wave ultrasound imaging," *IEEE Transactions on Ultrasonics, Ferroelectrics, and Frequency Control*, vol. 60, no. 9, pp. 1853–1867, Sep. 2013. [Online]. Available: http://ieeexplore.ieee.org/document/6587395/

[23] R. H. Stolt, "Migration by Fourier Transform," *GEOPHYSICS*, vol. 43, no. 1, pp. 23–48, Feb. 1978. [Online]. Available: http://library.seg.org/doi/10.1190/1.1440826

[24] O. Bernard, M. Zhang, F. Varray, P. Gueth, J.-P. Thiran, H. Liebgott, and D. Friboulet, "Ultrasound Fourier slice imaging: a novel approach for ultrafast imaging technique," in *2014 IEEE International Ultrasonics Symposium*. Chicago, IL, USA: IEEE, Sep. 2014, pp. 129–132. [Online]. Available: http://ieeexplore.ieee.org/document/6932218/

[25] M. Zhang, F. Varray, A. Besson, R. E. Carrillo, M. Viallon, D. Garcia, J.-P. Thiran, D. Friboulet, H. Liebgott, and O. Bernard, "Extension of fourier-based techniques for ultrafast imaging in ultrasound with diverging waves," *IEEE transactions on ultrasonics, ferroelectrics, and frequency control*, vol. 63, no. 12, pp. 2125–2137, 2016.

[26] T. Chernyakova and Y. Eldar, "Fourier-domain beamforming: the path to compressed ultrasound imaging," *IEEE transactions on ultrasonics, ferroelectrics, and frequency control*, vol. 61, no. 8, pp. 1252–1267, 2014.

[27] T. Szasz, A. Basarab, M.-F. Vaida, and D. Kouamé, "Beamforming with sparse prior in ultrasound medical imaging," *IEEE International Ultrasonics Symposium - IUS*, 2014.

[28] R. E. Carrillo, A. Besson, M. Zhang, D. Friboulet, Y. Wiaux, J.-P. Thiran, and O. Bernard, "A sparse regularization approach for ultrafast ultrasound imaging," in *Ultrasonics Symposium (IUS), 2015 IEEE International*. IEEE, 2015, pp. 1–4.

[29] J. Liu, Q. He, and J. Luo, "Compressed sensing for synthetic transmit aperture," in *Ultrasonics Symposium (IUS), 2015 IEEE International*. IEEE, 2015, pp. 1–4.

[30] A. Besson, R. E. Carrillo, O. Bernard, Y. Wiaux, and J.-P. Thiran, "Compressed delay-and-sum beamforming for ultrafast ultrasound imaging," *2016 IEEE International Conference on Image Processing (ICIP)*, pp. 2509–2513, 2016. [Online]. Available: http://ieeexplore.ieee.org/lpdocs/epic03/wrapper.htm?arnumber=7532811

[31] A. Besson, M. Zhang, F. Varray, H. Liebgott, D. Friboulet, Y. Wiaux, J.-P. Thiran, R. E. Carrillo, and O. Bernard, "A sparse reconstruction framework for Fourier-based plane wave imaging," *IEEE Transactions on Ultrasonics, Ferroelectrics, and Frequency Control*, vol. 3010, no. c, pp. 1–14, 2016.

[32] J. A. Jensen, *Estimation of blood velocities using ultrasound: a signal processing approach.* Cambridge University Press, 1996.

[33] J. Bercoff, G. Montaldo, T. Loupas, D. Savery, F. Mézière, M. Fink, and M. Tanter, "Ultrafast compound Doppler imaging: providing full blood flow characterization." *IEEE transactions on ultrasonics, ferroelectrics, and frequency control*, vol. 58, no. 1, pp. 134–47, 2011. [Online]. Available: http://www.ncbi.nlm.nih.gov/pubmed/21244981

[34] C. Kasai, K. Namekawa, a. Koyano, and R. Omoto, "Real-Time Two-Dimensional Blood Flow Imaging Using an Autocorrelation Technique," *IEEE Transactions on Sonics and Ultrasonics*, vol. 32, no. 3, pp. 458–464, 1985.

[35] T. Loupas, J. T. Powers, and R. W. Gill, "Axial velocity estimator for ultrasound blood flow imaging, based on a full evaluation of the Doppler equation by means of a two-dimensional autocorrelation approach," *IEEE Transactions on Ultrasonics, Ferroelectrics, and Frequency Control*, vol. 42, no. 4, pp. 672–688, 1995.

[36] H. Torp and K. Kristoffersen, "Velocity matched spectrum analysis: A new method for suppressing velocity ambiguity in pulsed-wave Doppler," *Ultrasound in Medicine & Biology*, vol. 21, no. 7, pp. 937–944, Jan. 1995. [Online]. Available: http://linkinghub.elsevier.com/retrieve/pii/030156299500039T

[37] C. Tremblay-Darveau, R. Williams, P. S. Sheeran, L. Milot, M. Bruce, and P. N. Burns, "Concepts and Tradeoffs in Velocity Estimation with Plane-Wave Contrast-Enhanced Doppler," *IEEE Transactions on Ultrasonics, Ferroelectrics, and Frequency Control*, vol. 63, no. 11, pp. 1890–1905, 2016.

[38] A. Jensen and S. Nikolov, "Directional synthetic aperture flow imaging," *IEEE Transactions on Ultrasonics, Ferroelectrics and Frequency Control*, vol. 51, no. 9, pp. 1107–1118, Sep. 2004. [Online]. Available: http://ieeexplore.ieee.org/document/1334843/

[39] R. Cohen, Y. Sde-Chen, T. Chernyakova, C. Fraschini, J. Bercoff, and Y. C. Eldar, "Fourier domain beamforming for coherent plane-wave compounding," *2015 IEEE International Ultrasonics Symposium (IUS)*, pp. 1–4, 2015. [Online]. Available: http://ieeexplore.ieee.org/lpdocs/epic03/wrapper.htm?arnumber=7329373

[40] I. K. Ekroll, M. M. Voormolen, O. K.-V. Standal, J. M. Rau, and L. Lovstakken, "Coherent compounding in doppler imaging," *IEEE Transactions on Ultrasonics,*

Ferroelectrics, and Frequency Control, vol. 62, no. 9, pp. 1634–1643, Sep. 2015. [Online]. Available: http://ieeexplore.ieee.org/lpdocs/epic03/wrapper.htm?arnumber=7272462

[41] C. Tremblay-Darveau, A. Bar-Zion, R. Williams, P. S. Sheeran, L. Milot, T. Loupas, D. Adam, M. Bruce, and P. N. Burns, "Improved contrast-enhanced power doppler using a coherence-based estimator," *IEEE Transactions on Medical Imaging*, vol. 36, no. 9, pp. 1901–1911, 2017.

[42] J. Capon, "High-resolution frequency-wavenumber spectrum analysis," *Proceedings of the IEEE*, vol. 57, no. 8, pp. 1408–1418, 1969.

[43] J. Synnevag, A. Austeng, and S. Holm, "Minimum variance adaptive beamforming applied to medical ultrasound imaging," *IEEE Ultrasonics Symposium 2005*, vol. 00, no. 4, pp. 1199–1202, 2005. [Online]. Available: http://ieeexplore.ieee.org/lpdocs/epic03/wrapper.htm?arnumber=1603066

[44] J. F. Synnevag, A. Austeng, and S. Holm, "Adaptive beamforming applied to medical ultrasound imaging," *Ultrasonics, Ferroelectrics and Frequency Control, IEEE Transactions on*, vol. 54, no. 8, pp. 1606–1613, 2007. [Online]. Available: http://www.ncbi.nlm.nih.gov/pubmed/17703664

[45] I. K. Holfort, F. Gran, and J. A. Jensen, "Minimum variance beamforming for high frame-rate ultrasound imaging," *Proceedings - IEEE Ultrasonics Symposium*, no. 3, pp. 1541–1544, 2007.

[46] ——, "Broadband Minimum Variance Beamforming for Medical Ultrasound Imaging," *IEEE Trans. Ultrason., Ferroelec., Freq. Contr.*, vol. 56, no. 2, pp. 314–325, 2009.

[47] K. Harmanci, J. Tabrikian, and J. L. Krolik, "Relationships between adaptive minimum variance beamforming and optimal source localization," *IEEE Transactions on Signal Processing*, vol. 48, no. 1, pp. 1–12, 2000.

[48] B. M. Asl and A. Mahloojifar, "Eigenspace-based minimum variance beamforming applied to medical ultrasound imaging," *IEEE transactions on ultrasonics, ferroelectrics, and frequency control*, vol. 57, no. 11, 2010.

[49] ——, "Contrast enhancement and robustness improvement of adaptive ultrasound imaging using forward-backward minimum variance beamforming," *IEEE Transactions on Ultrasonics, Ferroelectrics and Frequency Control*, vol. 58, no. 4, pp. 858–867, Apr. 2011. [Online]. Available: http://ieeexplore.ieee.org/document/5750109/

[50] I. K. Holfort, A. Austeng, J.-F. Synnevag, S. Holm, F. Gran, and J. A. Jensen, "Adaptive receive and transmit apodization for synthetic aperture ultrasound

imaging," in *2009 IEEE International Ultrasonics Symposium.* Rome: IEEE, Sep. 2009, pp. 1–4. [Online]. Available: http://ieeexplore.ieee.org/document/5442035/

[51] P. C. Li and M. L. Li, "Adaptive imaging using the generalized coherence factor," *IEEE Transactions on Ultrasonics, Ferroelectrics, and Frequency Control*, vol. 50, no. 2, pp. 128–141, 2003.

[52] C. H. Seo and J. T. Yen, "Sidelobe suppression in ultrasound imaging using dual apodization with cross-correlation," *IEEE Transactions on Ultrasonics, Ferroelectrics, and Frequency Control*, vol. 55, no. 10, pp. 2198–2210, 2008.

[53] J. Shin, Y. Chen, H. Malhi, and J. T. Yen, "Ultrasonic Reverberation Clutter Suppression Using Multiphase Apodization With Cross Correlation," *IEEE Transactions on Ultrasonics, Ferroelectrics, and Frequency Control*, vol. 63, no. 11, pp. 1947–1956, 2016.

[54] J. Camacho, M. Parrilla, and C. Fritsch, "Phase coherence imaging," *IEEE Transactions on Ultrasonics, Ferroelectrics, and Frequency Control*, vol. 56, no. 5, pp. 958–974, 2009.

[55] H. Hasegawa and H. Kanai, "Phase coherence factor with sub-aperture beamforming," *IEEE International Ultrasonics Symposium, IUS*, pp. 539–542, 2014.

[56] M. A. Lediju, G. E. Trahey, M. Jakovlijevic, B. C. Byram, and J. J. Dahl, "Short-lag spatial coherence imaging," *Proceedings - IEEE Ultrasonics Symposium*, pp. 987–990, 2010.

[57] K. K. Shung, R. A. Sigelmann, and J. M. Reid, "Scattering of ultrasound by blood," *IEEE Transactions on Biomedical Engineering*, vol. BME-23, no. 6, pp. 460–467, Nov 1976.

[58] D. H. Evans, J. A. Jensen, and M. B. Nielsen, "Ultrasonic colour Doppler imaging," *Interface Focus*, 2011.

[59] E. Stride and N. Saffari, "Microbubble ultrasound contrast agents: a review," *Proceedings of the Institution of Mechanical Engineers, Part H: Journal of Engineering in Medicine*, vol. 217, no. 6, pp. 429–447, 2003.

[60] C. Tremblay-darveau, R. Williams, L. Milot, M. Bruce, and P. N. Burns, "Combined Perfusion and Doppler Imaging Using Plane-Wave Nonlinear Detection and Microbubble Contrast Agents," *IEEE transactions on ultrasonics, ferroelectrics, and frequency control*, vol. 61, no. 12, pp. 1988–2000, 2014.

[61] D. Cosgrove, "Ultrasound contrast agents: An overview," *European Journal of Radiology*, vol. 60, no. 3, pp. 324–330, 2006.

[62] D. Cosgrove and C. Harvey, "Clinical uses of microbubbles in diagnosis and treatment," *Medical and Biological Engineering and Computing*, vol. 47, no. 8, pp. 813–826, 2009.

[63] K. Christensen-Jeffries, R. J. Browning, M. X. Tang, C. Dunsby, and R. J. Eckersley, "In vivo acoustic super-resolution and super-resolved velocity mapping using microbubbles," *IEEE Transactions on Medical Imaging*, vol. 34, no. 2, pp. 433–440, 2015.

[64] M. S. Plesset, "The dynamics of cavitation bubbles," *Journal of applied mechanics*, vol. 16, pp. 277–282, 1949.

[65] T. Faez, M. Emmer, K. Kooiman, M. Versluis, A. F. W. van der Steen, and N. de Jong, "20 years of ultrasound contrast agent modeling," *IEEE Transactions on Ultrasonics, Ferroelectrics and Frequency Control*, vol. 60, no. 1, Jan. 2013. [Online]. Available: http://ieeexplore.ieee.org/document/6396482/

[66] D. H. Simpson and P. N. Burns, "Pulse inversion Doppler: a new method for detecting nonlinear echoes from microbubble contrast agents," in *Ultrasonics Symposium, 1997. Proceedings., 1997 IEEE*, vol. 2. IEEE, 1997, pp. 1597–1600.

[67] N. de Jong, A. Bouakaz, and F. J. Ten Cate, "Contrast harmonic imaging," *Ultrasonics*, vol. 40, no. 1-8, pp. 567–573, May 2002. [Online]. Available: http://linkinghub.elsevier.com/retrieve/pii/S0041624X02001713

[68] F. Lin, C. Cachard, F. Varray, and O. Basset, "Generalization of Multipulse Transmission Techniques for Ultrasound Imaging," *Ultrasonic Imaging*, vol. 37, no. 4, pp. 294–311, Oct. 2015. [Online]. Available: http://journals.sagepub.com/doi/10.1177/0161734614566696

[69] P. Tortoli, D. Bagnai, and D. Righi, "Quantitative analysis of Doppler spectrum modifications yielded by contrast agents insonified at high pressure." *IEEE transactions on ultrasonics, ferroelectrics, and frequency control*, vol. 46, no. 1, pp. 247–51, 1999. [Online]. Available: http://www.ncbi.nlm.nih.gov/pubmed/18238421

[70] M.-X. Tang, H. Mulvana, T. Gauthier, A. K. P. Lim, D. O. Cosgrove, R. J. Eckersley, and E. Stride, "Quantitative contrast-enhanced ultrasound imaging: a review of sources of variability," *Interface Focus*, vol. 1, no. 4, pp. 520–539, Aug. 2011. [Online]. Available: http://rsfs.royalsocietypublishing.org/cgi/doi/10.1098/rsfs.2011.0026

[71] S. Qin, C. F. Caskey, and K. W. Ferrara, "Ultrasound contrast microbubbles in imaging and therapy: physical principles and engineering," *Physics in Medicine and Biology*, vol. 54, no. 6, pp. R27–R57, Mar. 2009. [Online]. Available: http://stacks.iop.org/0031-9155/54/i=6/a=R01?key=crossref.747f537e4cc42fed007c7f0875ec5880

[72] C. Demene, T. Deffieux, M. Pernot, B.-F. Osmanski, V. Biran, S. Franqui, J.-M. Correas, I. Cohen, O. Baud, and M. Tanter, "Spatiotemporal clutter filtering of ultrafast ultrasound data highly increases Doppler and fUltrasound sensitivity." *IEEE transactions on medical imaging*, vol. PP, no. 99, p. 1, 2015. [Online]. Available: http://www.ncbi.nlm.nih.gov/pubmed/25955583

[73] T. R. Porter and F. Xie, "Myocardial Perfusion Imaging With Contrast Ultrasound," *JACC: Cardiovascular Imaging*, vol. 3, no. 2, pp. 176–187, Feb. 2010. [Online]. Available: http://linkinghub.elsevier.com/retrieve/pii/S1936878X09007943

[74] W. F. Armstrong and T. Ryan, "Stress Echocardiography from 1979 to Present," *Journal of the American Society of Echocardiography*, vol. 21, no. 1, pp. 22–28, Jan. 2008. [Online]. Available: http://linkinghub.elsevier.com/retrieve/pii/S0894731707008103

[75] Y. Li, C. P. Ho, M. Toulemonde, N. Chahal, R. Senior, and M. X. Tang, "Fully Automatic Myocardial Segmentation of Contrast Echocardiography Sequence Using Random Forests Guided by Shape Model," *IEEE Transactions on Medical Imaging*, vol. XX, no. X, pp. 1–11, 2017.

[76] M. Toulemonde, R. Corbett, V. Papadopoulou, N. Chahal, Y. Li, C. Leow, D. Cosgrove, R. Eckersley, N. Duncan, R. Senior, and M.-X. Tang, "High Frame-Rate Contrast Echocardiography: In-Human Demonstration," *JACC: Cardiovascular Imaging*, pp. 1–2, 2017. [Online]. Available: https://doi.org/10.1016/j.jcmg.2017.09.011

[77] M. D'Onofrio, S. Crosara, R. De Robertis, S. Canestrini, and R. P. Mucelli, "Contrast-Enhanced Ultrasound of Focal Liver Lesions," *American Journal of Roentgenology*, vol. 205, no. 1, pp. W56–W66, Jul. 2015. [Online]. Available: http://www.ajronline.org/doi/10.2214/AJR.14.14203

[78] T. van Rooij, V. Daeichin, I. Skachkov, N. de Jong, and K. Kooiman, "Targeted ultrasound contrast agents for ultrasound molecular imaging and therapy," *International journal of hyperthermia*, vol. 31, no. 2, pp. 90–106, 2015.

[79] A. L. Klibanov, "Ligand-carrying gas-filled microbubbles: Ultrasound contrast agents for targeted molecular imaging," *Bioconjugate Chemistry*, vol. 16, no. 1, pp. 9–17, 2005.

[80] M. E. Maragoudakis, "Angiogenesis in health and disease," *General Pharmacology: Vascular System*, vol. 35, no. 5, pp. 225–226, 2000.

[81] D. B. Ellegala, H. Leong-Poi, J. E. Carpenter, A. L. Klibanov, S. Kaul, M. E. Shaffrey, J. Sklenar, and J. R. Lindner, "Imaging tumor angiogenesis with contrast

ultrasound and microbubbles targeted to avb3," *Circulation*, vol. 108, no. 3, pp. 336–341, 2003.

[82] J. R. Lindner, "Microbubbles in medical imaging: current applications and future directions." *Nature reviews. Drug discovery*, vol. 3, no. 6, pp. 527–32, 2004. [Online]. Available: http://dx.doi.org/10.1038/nrd1417

[83] V. R. Stewart and P. S. Sidhu, "New directions in ultrasound: Microbubble contrast," *British Journal of Radiology*, vol. 79, no. 939, pp. 188–194, 2006.

[84] B. B. Goldberg, J. B. Liu, and F. Forsberg, "Ultrasound contrast agents: a review." *Ultrasound in medicine & biology*, vol. 20, no. 4, pp. 319–333, 1994.

[85] J. Provost, C. Papadacci, J. E. Arango, M. Imbault, M. Fink, J.-L. Gennisson, M. Tanter, and M. Pernot, "3d ultrafast ultrasound imaging in vivo," *Physics in Medicine & Biology*, vol. 59, no. 19, p. L1, 2014.

[86] B. Y. S. Yiu, S. S. M. Lai, and A. C. H. Yu, "Vector Projectile Imaging: Time-Resolved Dynamic Visualization of Complex Flow Patterns," *Ultrasound in Medicine and Biology*, vol. 40, no. 9, pp. 2295–2309, 2014.

[87] C. H. Leow, E. Bazigou, R. J. Eckersley, A. C. H. Yu, P. D. Weinberg, and M.-X. Tang, "Flow Velocity Mapping Using Contrast Enhanced High-Frame-Rate Plane Wave Ultrasound and Image Tracking: Methods and Initial in Vitro and in Vivo Evaluation." *Ultrasound in medicine & biology*, vol. 41, no. 11, pp. 2913–2925, 2015.

[88] K. Wei, a. R. Jayaweera, S. Firoozan, a. Linka, D. M. Skyba, and S. Kaul, "Quantification of myocardial blood flow with ultrasound-induced destruction of microbubbles administered as a constant venous infusion." *Circulation*, vol. 97, no. 5, pp. 473–483, 1998.

[89] F. Lin, C. Cachard, R. Mori, F. Varray, F. Guidi, and O. Basset, "Ultrasound contrast imaging: Influence of scatterer motion in multi-pulse techniques," *IEEE Transactions on Ultrasonics, Ferroelectrics, and Frequency Control*, vol. 60, no. 10, pp. 2065–2078, 2013.

[90] C. C. Shen and P. C. Li, "Motion artifacts of pulse inversion-based tissue harmonic imaging," *IEEE Transactions on Ultrasonics, Ferroelectrics, and Frequency Control*, vol. 49, no. 9, pp. 1203–1211, 2002.

[91] J. Viti, H. J. Vos, N. d. Jong, F. Guidi, and P. Tortoli, "Detection of Contrast Agents: Plane Wave Versus Focused Transmission," *IEEE Transactions on Ultrasonics, Ferroelectrics, and Frequency Control*, vol. 63, no. 2, pp. 203–211, Feb. 2016. [Online]. Available: http://ieeexplore.ieee.org/document/7342972/

[92] C. Tremblay-Darveau, R. Williams, L. Milot, M. Bruce, and P. N. Burns, “Visualizing the tumor microvasculature with a nonlinear plane-wave doppler imaging scheme based on amplitude modulation,” *IEEE transactions on medical imaging*, vol. 35, no. 2, pp. 699–709, 2016.

[93] K. L. Gammelmark and J. A. Jensen, “2-D tissue motion compensation of synthetic transmit aperture images,” *IEEE Transactions on Ultrasonics, Ferroelectrics, and Frequency Control*, vol. 61, no. 4, pp. 594–610, Apr. 2014. [Online]. Available: http://ieeexplore.ieee.org/lpdocs/epic03/wrapper.htm?arnumber=6822987

[94] J. Poree, D. Posada, A. Hodzic, F. Tournoux, G. Cloutier, and D. Garcia, “High-Frame-Rate Echocardiography Using Coherent Compounding with Doppler-Based Motion-Compensation,” *IEEE Transactions on Medical Imaging*, vol. 35, no. 7, pp. 1647–1657, 2016.

[95] J. Flynn, R. Daigle, L. Pflugrath, K. Linkhart, and P. Kaczkowski, “Estimation and display for Vector Doppler Imaging using planewave transmissions,” in *2011 IEEE International Ultrasonics Symposium.* Orlando, FL, USA: IEEE, Oct. 2011, pp. 413–418. [Online]. Available: http://ieeexplore.ieee.org/document/6293682/

[96] M. Toulemonde, Y. Li, S. Lin, M. X. Tang, M. Butler, V. Sboros, R. J. Eckersley, and W. Duncan, “Cardiac imaging with high frame rate contrast enhanced ultrasound : in-vivo demonstration,” *IEEE International Ultrasonics Symposium (IUS)E*, pp. 1–4, 2016.

[97] J. A. Jensen and N. B. Svendsen, “Calculation of pressure fields from arbitrarily shaped, apodized, and excited ultrasound transducers,” *IEEE transactions on ultrasonics, ferroelectrics, and frequency control*, vol. 39, no. 2, pp. 262–267, 1992.

[98] J.-M. GORCE, M. ARDITI, and M. SCHNEIDER, “Influence of Bubble Size Distribution on the Echogenicity of Ultrasound Contrast Agents,” *Investigative Radiology*, vol. 35, no. 11, pp. 661–671, 2000. [Online]. Available: http://content.wkhealth.com/linkback/openurl?sid=WKPTLP:landingpage&an=00004424-200011000-00003

[99] P. Marmottant, S. van der Meer, M. Emmer, M. Versluis, N. de Jong, S. Hilgenfeldt, and D. Lohse, “A model for large amplitude oscillations of coated bubbles accounting for buckling and rupture,” *The Journal of the Acoustical Society of America*, vol. 118, no. 6, pp. 3499–3505, 2005.

[100] J. Tu, J. Guan, Y. Qiu, and T. J. Matula, “Estimating the shell parameters of SonoVue ® microbubbles using light scattering,” *The Journal of the Acoustical Society of America*, vol. 126, no. 6, pp. 2954–2962, 2009.

[101] D. Rueckert, L. I. Sonoda, C. Hayes, D. L. Hill, M. O. Leach, and D. J. Hawkes, "Nonrigid registration using free-form deformations: application to breast MR images," *IEEE transactions on medical imaging*, vol. 18, no. 8, pp. 712–721, 1999.

[102] S. Harput, K. Christensen-Jeffries, J. Brown, Y. Li, K. J. Williams, A. H. Davies, R. J. Eckersley, C. Dunsby, and M.-X. Tang, "Two-Stage Motion Correction for Super-Resolution Ultrasound Imaging in Human Lower Limb," *IEEE Transactions on Ultrasonics, Ferroelectrics, and Frequency Control*, vol. 65, no. 5, pp. 803–814, May 2018. [Online]. Available: https://ieeexplore.ieee.org/document/8334280/

[103] M. Toulemonde, W. C. Duncan, A. Stanziola, and R. J. Eckersley, "Effects of motion on high frame rate contrast enhanced echocardiography and its correction," *IEEE International Ultrasonics Symposium (IUS)*, pp. 31–34, 2017.

[104] M. X. Tang and R. J. Eckersley, "Frequency and pressure dependent attenuation and scattering by microbubbles," *Ultrasound in Medicine and Biology*, vol. 33, no. 1, pp. 164–168, 2007.

[105] J. Tierney, C. Coolbaugh, T. Towse, and B. Byram, "Adaptive clutter demodulation for non-contrast ultrasound perfusion imaging," *IEEE Transactions on Medical Imaging*, vol. 36, no. 9, pp. 1979–1991, 2017.

[106] P. Song, A. Manduca, J. Trzasko, and S. Chen, "Ultrasound Small Vessel Imaging with Block-Wise Adaptive Local Clutter Filtering," *IEEE Transactions on Medical Imaging*, vol. 0062, no. c, pp. 1–1, 2016. [Online]. Available: http://ieeexplore.ieee.org/document/7559732/

[107] Y. L. Li and J. J. Dahl, "Coherent flow power doppler (CFPD): flow detection using spatial coherence beamforming." *IEEE transactions on ultrasonics, ferroelectrics, and frequency control*, vol. 62, no. 6, pp. 1022–35, 2015. [Online]. Available: http://www.pubmedcentral.nih.gov/articlerender.fcgi?artid=4467462&tool=pmcentrez&rendertype=abstract

[108] J. Shin and J. T. Yen, "Clutter suppression using Phase Apodization with Cross-correlation in ultrasound imaging," *IEEE International Ultrasonics Symposium, IUS*, pp. 793–796, 2013.

[109] J. Shin, Y. Chen, M. Nguyen, and J. T. Yen, "Robust ultrasonic reverberation clutter suppression using Multi-Apodization with Cross-correlation," *IEEE International Ultrasonics Symposium, IUS*, pp. 543–546, 2014.

[110] M.-X. Tang, N. Kamiyama, and R. J. Eckersley, "Effects of nonlinear propagation in ultrasound contrast agent imaging." *Ultrasound in medicine & biology*, vol. 36, no. 3, pp. 459–66, 2010. [Online]. Available: http://www.ncbi.nlm.nih.gov/pubmed/20133035

[111] J. Udesen and J. A. Jensen, "Investigation of transverse oscillation method," *IEEE Transactions on Ultrasonics, Ferroelectrics, and Frequency Control*, vol. 53, no. 5, pp. 959–971, 2006.

[112] A. Stanziola and M.-x. Tang, "Temporal and spatial processing of high frame-rate contrast enhanced ultrasound data," *The 21 st European Symposium on Ultrasound Contrast Imaging*, no. January, 2016.

[113] E. Mace, G. Montaldo, B. F. Osmanski, I. Cohen, M. Fink, and M. Tanter, "Functional ultrasound imaging of the brain: Theory and basic principles," *IEEE Transactions on Ultrasonics, Ferroelectrics, and Frequency Control*, vol. 60, no. 3, pp. 492–506, 2013.

[114] K. Diamantis, T. Anderson, M. B. Butler, C. A. Villagomez-Hoyos, J. A. Jensen, and V. Sboros, "Resolving Ultrasound Contrast Microbubbles using Minimum Variance Beamforming," *IEEE Transactions on Medical Imaging*, pp. 1–1, 2018. [Online]. Available: https://ieeexplore.ieee.org/document/8421245/

[115] O. L. Frost, "An algorithm for linearly constrained adaptive array processing," *Proceedings of the IEEE*, vol. 60, no. 8, pp. 926–935, 1972.

[116] L. Du, T. Yardibi, J. Li, and P. Stoica, "Review of user parameter-free robust adaptive beamforming algorithms," in *Signals, Systems and Computers, 2008 42nd Asilomar Conference on.* IEEE, 2008, pp. 363–367.

[117] P. Stoica, J. Li, and X. Tan, "On spatial power spectrum and signal estimation using the Pisarenko framework," *IEEE Transactions on Signal Processing*, vol. 56, no. 10, pp. 5109–5119, 2008.

[118] L. Bottou, "Stochastic gradient learning in neural networks," *Proceedings of Neuro-Nımes*, vol. 91, no. 8, p. 12, 1991.

[119] A. Stanziola, C. H. Leow, E. Bazigou, P. D. Weinberg, and M. Tang, "ASAP: Super-Contrast Vasculature Imaging Using Coherence Analysis and High Frame-Rate Contrast Enhanced Ultrasound," *IEEE Transactions on Medical Imaging*, vol. 37, no. 8, pp. 1847–1856, Aug. 2018.

[120] A. Bar-Zion, C. Tremblay-Darveau, O. Solomon, D. Adam, and Y. C. Eldar, "Fast Vascular Ultrasound Imaging With Enhanced Spatial Resolution and Background Rejection," *IEEE Transactions on Medical Imaging*, vol. 36, no. 1, pp. 169–180, Jan. 2017.

[121] M. A. Lediju, G. E. Trahey, B. C. Byram, and J. J. Dahl, "Short-lag spatial coherence of backscattered echoes: Imaging characteristics," *IEEE Transactions on*

Ultrasonics, Ferroelectrics, and Frequency Control, vol. 58, no. 7, pp. 1377–1388, 2011.

[122] A. Cichocki, D. Mandic, L. De Lathauwer, G. Zhou, Q. Zhao, C. Caiafa, and H. A. Phan, "Tensor Decompositions for Signal Processing Applications: From two-way to multiway component analysis," *IEEE Signal Processing Magazine*, vol. 32, no. 2, pp. 145–163, Mar. 2015. [Online]. Available: http://ieeexplore.ieee.org/document/7038247/

[123] C. Caiafa and a. Cichocki, "Multidimensional compressed sensing and their applications," *Wiley Interdisciplinary Reviews: Data \ldots*, pp. 1–41, 2013. [Online]. Available: http://onlinelibrary.wiley.com/doi/10.1002/widm.1108/full

[124] C. Papadacci, M. Pernot, M. Couade, M. Fink, and M. Tanter, "High-contrast ultrafast imaging of the heart," *IEEE Transactions on Ultrasonics, Ferroelectrics, and Frequency Control*, vol. 61, no. 2, pp. 288–301, 2014.

[125] L. Tong, V. Soon, Y. Huang, and R. Liu, "AMUSE: a new blind identification algorithm," in *Circuits and Systems, 1990., IEEE International Symposium on.* IEEE, 1990, pp. 1784–1787.

[126] K. Matsuoka, M. Ohoya, and M. Kawamoto, "A neural net for blind separation of nonstationary signals," *Neural networks*, vol. 8, no. 3, pp. 411–419, 1995.

[127] M. Bayat and M. Fatemi, "Concurrent Clutter and Noise Suppression via Low Rank Plus Sparse Optimization for Non-Contrast Ultrasound Flow Doppler Processing in Microvasculature," in *2018 IEEE International Conference on Acoustics, Speech and Signal Processing (ICASSP).* IEEE, 2018, pp. 1080–1084.